Chaos and Structures in Geophysics and Astrophysics

Antonello Provenzale and Neil J. Balmforth

Lecture 1

Fundamentals

1.1 Introduction

Even though our limited perceptions provide us with only a brief glimpse of the Universe, the main lesson that we learn from our observation is that the world is complicated. Very complicated. Every part of the universe interacts with the other parts; the responses of each component are never proportional to the applied forces, and the feedbacks of one subsystem on another cannot be discarded. As a result, processes are unpredictable, and chaotic behavior is a common occurrence. Disorder and turbulence become rife. Yet from the chaotic background, coherent structures sometimes emerge, patterns form, and local order is generated.

In the face of the wealth of phenomena, the myriad of details and the richness of quality and quantity, the quest for scientific understanding might seem to be a hopeless endeavour. Perhaps it is a fundamental human flaw that leads us to challenge this point of view. But challenge it we do. And at end of our struggles, perhaps we will find some comfort in judging how far we have come, and how infinitely further we could continue. At the very least, it may cure the crisis of mid-life. Thus, even if it may be pointless to try to describe what can happen in the universe, in these lecture notes, for reasons obscured to all but the fellows, we begin to do so.

There are indeed several ways of approaching the overwelming complexity of nature. One is simply to observe the natural world, and make quantitative measurements. This is what is often done in astrophysics and geophysics, where little or no control can be obtained on the system under study. But this approach is always limited if we have no scientific framework with which we can rationalize the observations.

The other approaches seek to establish some foundation on which to build our understanding. But to build such a foundation, we must meet head-on the complexity of the problems we seek to explain, and this constitutes an impossible undertaking: we cannot study the full complexity of things by a unique approach, and sometimes we do not even know whether there is a meaningful "universal law" behind the observations (as in biological evolution or human psychology).

Instead, we progress like ancient Romans; we divide, then conquer. Put more scientifically,

we begin by isolating some natural phenomenon, separating parts of a whole that should probably stay together. Moreover, we simply ignore most of the physical ingredients and deal only with those parts that can be couched as mathematical problems. Then we formulate idealized problems that model what we deem to be the most essential pieces of the selected phenomena. Finally, we attempt to solve those simple models. In other words, we conjure incomplete images of the real world, then disect them.

More troubles, however, arise. For many systems, we do not have a clean mathematical formulation of the problem (such as in problems of landscape evolution, or earthquake dynamics, or sociology). In other instances, even though we deal with problems that can be couched in terms of mathematical equations, we are not always able to solve them in their full generality. This is especially true in geophysics (and sometimes in astrophysics), where we believe that fluid mechanics offers a formalism to understand the atmosphere and oceans: the Navier-Stokes equations have been known for two centuries, but we have yet to solve them. Thus, even our attempts to divide and conquer run into trouble.

These fundamental difficulties lead to a division in scientific ideology regarding how one should approach the idealized problems. As Ed Spiegel pleasantly puts it, one ideology suggests a method that is championed by the "slobs", the other to methods advocated by the "bores".

The first methodology involves efforts to incorporate *as much as possible*. The tools are numerical simulation and big computers; the results are GCMs, numerical climate models, galaxies of point particles, and stars made of treacle. In these hi-tech approaches, researchers invent a new, virtual world, wherein they perform sophisticated numerical simulations that incorporate as many aspect of reality as possible - and parametrize those which are left out. But with the mass of the included details comes an unweildiness, an inability to truly assess the robustness of solutions, and even at times to correctly solve the equations.

The second ideology could be described as escapism. We abstract even more from the physics, idealize yet further, until we arrive at a problem that, though totally divorced from reality, can be solved precisely and elegantly. The solutions may not be relevant to the problem that motivated the mathematical analysis, but it is pretty, inexpensive and very alluring.

Of course, this description makes mockery of the two approaches. But there are dangers in the two ideologies, and perhaps this mockery will make the reader aware of their respective pitfalls. From a different perspective, both methodologies amount to true attempts to learn about the real world. And any serious explanation should no doubt consist of both. There are settings in which one may be more useful than the other, and instances in which real progress can only be made when the two methods are used in concert.

As in true Walsh Cottage Tradition, the lecture notes that follow are devoted to an approach that more closely follows the second ideology. In particular, we shall explore a few simplified - in fact, always oversimplified - models of various geophysical and astrophysical processes, mainly using concepts from dynamical system theory. In such an effort, we do not expect to find quantitative correspondence between the models and reality, but we aim at understanding some aspects of some of the main processes at work, possibly estimating their respective roles and importance. And, perhaps surprisingly, from time to time we hope that we succeed in understanding something of the complicated Universe that surrounds us.

1.2 Some elementary dynamical systems theory

There are many books devoted to the properties of dynamical systems (*e.g.* Drazin 1992; Ott 1993; Ott *et al.* 1994). Here, we simply mention some of the relevant concepts which will be used in the rest of the lectures.

A dynamical system is a mathematical model or law,

$$\mathbf{X}_t \mapsto \mathbf{X}_{t+\delta t} = \Phi_{\delta t}(\mathbf{X}_t), \tag{1.1}$$

where $\mathbf{X}_t$ is a vector of variables that completely describes the state of the system at time t,

$$\mathbf{X}_t \equiv (X_t^{(1)}, X_t^{(2)}, X_t^{(3)}, \cdots, X_t^{(N)}), \quad X_t \in \mathbb{R}^N, \tag{1.2}$$

and $\mathbf{X}_{t+\delta t}$ is the state of the system at time $t + \delta t$. The particular choice of state variables is dictated by the nature of the system. For example, in thermodynamics of ideal gases we might choose temperature, pressure and volume as dynamical variables.

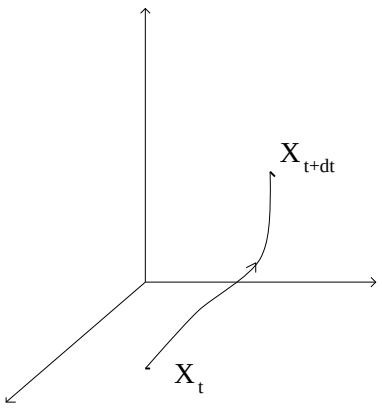

Figure 1.1: A trajectory in phase space

The state of the system at any time may be represented by a point in *phase space*; that is, an $N-$dimensional space spanned by the N dynamical variables. The number of degrees of freedom (DOF) of a system is defined by the dimensionality of its phase space (N).

Example: The logistic map One of the most commonly used examples of a chaotic dynamical system is the logistic map (see Fig. 1.2):

$$\begin{aligned} X_{n+1} &= 4aX_n(1 - X_n), \\ & \quad 0 \leq X_n \leq 1 \quad , \quad 0 \leq a \leq 1. \end{aligned} \tag{1.3}$$

This system has been used in applications as diverse as describing insect population outbreaks and the generation of pseudo-random numbers. The behavior of the system depends on the value of the parameter a, which determines the height of the parabola (*c.f.* a_1, a_2, a_3 in Fig.

1.2). An important characteristic of this system is that, for sufficiently large a, the time series of X_n is chaotic and two points with similar initial conditions may not remain close under iteration of the map. That is, there is sensitive dependence on initial condition.

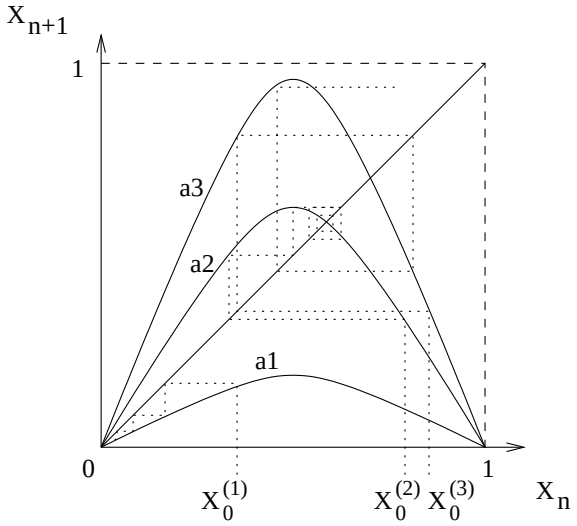

Figure 1.2: *La mappa logistica*. The logistic map. The dotted lines show sample evolution sequences. For smaller values of a, such as a_1, the system iterates to $X = 0$. For larger a (like a_2) the system converges to the nontrivial fixed point. At the largest values of a (a_3), the system is chaotic, with initial close trajectories from nearby initial conditions diverging exponentially quickly.

1.2.1 Linear versus nonlinear dynamics

A crucially important feature of the logistic map that is essential in creating complicated dynamics is nonlinearity. This highights the fact that nonlinear systems are fundamentally different from linear ones.

A linear system may be considered to have outputs which are proportional to its inputs. This leads to a relatively simple range of dynamical behaviour. By contrast, a nonlinear system does not in general obey this law of proportionality. In other words, the evolution law of a nonlinear system cannot be expressed in terms of a linear transformation of a previous state: $\mathbf{X}_{t+\delta t} = \mathbf{f}(\mathbf{X}_t) \neq \mathbf{M} \cdot \mathbf{X}_t$, for some matrix or linear operator (M).

For nonlinear systems, the principle of superposition does not, in general, hold. That is, if we are given two solutions X_t and Y_t of a nonlinear system, $\alpha X_t + \beta Y_t$ is not necessarily a solution.

Nonlinear systems may exhibit many types of temporal evolution, depending on the structure of the system. The behaviour can be a simple as the relaxation to an equilibrium or a *fixed point*, for which $\mathbf{X}(t + \delta t) = \mathbf{X}(t)$. Linear systems can also display this behaviour, but

a key difference in a nonlinear system is that there can be *multiple equilibria*.

Another simple solution to a nonlinear system is a periodic orbit. These reflect oscillations of the system and are again familiar from linear dynamics. But the evolution of a nonlinear system can be substantially more complicated. Notably, it can be *chaotic*.

1.2.2 Determinism and randomness

An important distinction between dynamical systems surrounds whether the dynamics is completely deterministic, or whether the evolution proceeds at least partly as a result of stochastic effects.

For deterministic dynamical systems, if we are given an initial state X_t, then the state at some later time, $X_{t+\delta t}$, is uniquely determined via the evolution law. This property of uniqueness implies that for deterministic systems, trajectories in phase space may never cross at finite time.

For stochastic dynamical systems, only the probability $P(X_{t+\delta t})$ may be determined from the knowledge of X_t, and trajectories in phase space may cross. It is sometimes useful to consider deterministic dynamical systems as stochastic ones simply because we do not possess a full description of all the variables, or if the system has many degrees of freedom and it proves more expedient to eliminate some variables and treat the system as if it were stochastic.

1.2.3 Types of Dynamical Systems

Dynamical systems come in many different shapes and forms, and it is often convenient to introduce some sort of classification scheme. So we do here.

The simplest types of dynamical systems are those for which the evolution law takes the form of a simple algebraic operation. Such an operation arises when we consider systems in which time is *discrete*. Then,

$$\mathbf{X}_{t+1} = f(\mathbf{X}_t) \tag{1.4}$$

where $\mathbf{X} \in \mathbb{R}^N$, and $f(\mathbf{X}_t)$ is a known algebraic function. Such dynamical systems are often called "maps of the interval" if there is a single dependent variable, or "maps of the plane" (for two such variables), or simply "maps". The logistic map that we have already encountered is one of the canonical examples of a one-dimensioanl map. Discrete-time systems are not always maps of $\mathbb{R}^N$ into itself. Cellular automata and games of life are also discrete-time dynamical systems.

When the time variable is continuous, the evolution law of the dynamical system takes the form of a set of differential equations. Then we deal with continuous-time dynamical systems, the simplest examples of which are governed by ordinary differential equations:

$$\frac{d\mathbf{X}}{dt} = \dot{\mathbf{X}} = \mathbf{F}(\mathbf{X}), \tag{1.5}$$

with $\mathbf{X} \in \mathbb{R}^N$ and $\mathbf{F}(\mathbf{X})$ again a prescribed function. Typically we solve the system as an initial-value problem with the image in mind of the system evolving from some known initial state. Much of lecture 2 will be concerned with these kinds of systems.

ODEs of the form (1.5) are finite dimensional; the solutions can be envisioned as orbits within a space of $N-$dimensions. More complicated continuous-time dynamical systems have infinite dimension. Two commonly encountered examples of such systems are delay-differential equations and partial-differential systems.

The evolution law for delay-differential equations contains the entire history of the trajectory:

$$\frac{d\mathbf{X}}{dt} = \int_0^t \mathbf{K}[\mathbf{X}(t'), t']dt', \tag{1.6}$$

where $\mathbf{K}[\mathbf{X}(t), t]$ is a known kernel. Such models usually arise in systems with long-term memory.

Partial differential equations (PDEs) may be expressed as

$$\frac{\partial \omega}{\partial t} = K[\omega, \nabla\omega, \cdots], \tag{1.7}$$

where ∇ is the gradient operator in the spatial variables. Along with the spatial dimensions come a variety of boundary conditions. An example relevant to these lectures is two-dimensional Navier-Stokes flow:

$$\frac{\partial \omega}{\partial t} + [\psi, \omega] = \nu\nabla^2\omega, \tag{1.8}$$

where $\omega = \nabla^2\psi$ is vorticity and ψ is the stream function.

Solutions to continuous-time dynamical systems can be described as trajectories in the phase space that begin from a single point characterizing the initial condition. The set of all possible trajectories can be thought of as defining a velocity field, $\mathbf{u} = d\mathbf{X}/dt$ in the phase space. For this reason, continuous-time dynamical systems are sometimes referred to as "flows".

Finally, stochastic systems are described by equations where a random term enters the dynamics. A classic example is the linear Langevin equation (or Ornstein-Uhlenbeck process)

$$du = -\frac{u}{T}dt + \frac{\sigma}{T^{1/2}}dW, \tag{1.9}$$

where T is a decorrelation time for the random variable u, σ^2 is the variance of u and dW is a random white noise term characterized by $\langle dW\rangle = 0$ and $\langle dW(t)dW(t')\rangle = 2dt\delta(t - t')$. Here, $\langle ...\rangle$ indicates ensemble average. System (1.9) generates a time series $u(t)$ with a gaussian amplitude distribution $p(u)$ and exponentially decaying autocorrelation, $\langle u(t)u(t + \tau)\rangle \propto \exp(-\tau/T)$. Given the present state of such a stochastic system, say $u(0)$, we cannot determine its future state precisely. We can just determine the probability of a future state given the present one, i.e., $P[u|u(0)]$. Nonlinear stochastic processes are also possible. First-order (in time) nonlinear processes take the general form

$$dv = f(v)dt + g(v)dW, \tag{1.10}$$

where dW is still a white-noise process (Wiener process). For such a model, the probability distribution $p(v)$ is not necessarily gaussian. We shall encounter one of these nonlinear stochastic systems in Lecture 3.

1.2.4 Conservative dynamical systems

A dynamical system is called conservative if there is a quantity $E(\mathbf{X}_t)$ which is constant during the evolution:

$$\dot{E} = 0. \tag{1.11}$$

This implies that the system dynamics takes place on a manifold with dimension $N-1$, defined by $E =$ constant.

Conservative systems are referred to as Hamiltonian systems if they can be written in the form,

$$\left.\begin{array}{rcl} H & = & E \\ \dot{q}_j & = & \frac{\partial H}{\partial p_j} \\ \dot{p}_j & = & -\frac{\partial H}{\partial q_j} \end{array}\right\}, j = 1, ..., \frac{N}{2}, \tag{1.12}$$

where q and p are canonically conjugate variables. For such a system, the number of degrees of freedom is traditionally defined as $N/2$, *i.e.*, as the number of pairs of canonically conjugate variables.

Dynamical systems of the form $\dot{\mathbf{X}} = \mathbf{F}(\mathbf{X})$ preserve phase-space volume if

$$\nabla \cdot \mathbf{F} = 0. \tag{1.13}$$

To see this, let us take the Taylor expansion of a solution $\mathbf{X}(t+h)$ for small h:

$$\mathbf{X}(t+h) = \mathbf{X}(t) + h\dot{\mathbf{X}}(t) + o(h). \tag{1.14}$$

Note that $o(h)$ refers to terms with powers of h greater than one, including fractional powers. The time evolution of a volume element is described by the determinant of the Jacobian matrix $\frac{\partial X_i(t+h)}{\partial X_j(t)}$. This is given by

$$\begin{aligned} \det J &= \det\left\{\frac{\partial X_i(t+h)}{\partial X_j(t)}\right\} \\ &= \det\left\{\delta_{ij} + h\left(\frac{\partial F_i}{\partial X_j}\right)_t + o(h)\right\} \\ &= 1 + h\ \nabla \cdot \mathbf{F} + o(h). \end{aligned} \tag{1.15}$$

For example, in two-dimensional flow, after discarding terms $o(h)$,

$$\det J = \begin{vmatrix} 1 + \frac{\partial F_1}{\partial X_1}h & \frac{\partial F_1}{\partial X_2}h \\ \frac{\partial F_2}{\partial X_1}h & 1 + \frac{\partial F_2}{\partial X_2}h \end{vmatrix} \tag{1.16}$$

$$= \left(1 + h\frac{\partial F_1}{\partial X_1}\right)\left(1 + h\frac{\partial F_2}{\partial X_2}\right) - h^2\frac{\partial F_1}{\partial X_2}\frac{\partial F_2}{\partial X_1}$$

$$\approx 1 + h\left(\frac{\partial F_1}{\partial X_1} + \frac{\partial F_2}{\partial X_2}\right). \tag{1.17}$$

Thus if $\nabla \cdot F = 0$ then $\det J = 1$ and the phase space volume does not change.

The existence of a conserved quantity, E, and volume preservation in phase space are independent properties of dynamical systems. However, many conservative systems of physical interest are also characterized by preservation of volumes in phase space. If the system does preserve volume, then the associated velocity field of the flow, $\mathbf{u} = d\mathbf{x}/dt$, is *incompressible*.

1.2.5 Dissipative dynamical systems

Dissipative systems are those for which the volume of phase space occupied by a set of initial conditions is not conserved, and, in fact, decreases over the course of time: $\nabla \cdot \mathbf{F} < 0$. In other words, the flow of the dynamical system is *contracting*. Provided the system is bound, then this contraction implies that, as $t \to \infty$, the motion becomes confined to a set A with zero volume in phase space and dimension $D < N$. This set is an "attractor" of the system.

Two useful concepts are the following:

Invariant Set: An invariant set A is one which maps to itself under the flow: $A \stackrel{t}{\to} A$.

Attracting Set: An invariant set A is an attracting set (an attractor) if there exists a set B with non-zero measure, $A \subset B$, such that $B \stackrel{t}{\to} A$. B is called the *basin of attraction* of A.

In dissipative systems there can be many qualitatively different types of attractors. The most commonly encountered attractors are:

- Fixed points
- Limit cycles
- Quasi-periodic motion
- Chaotic (strange) attractors

1.3 Dust Grains in a Stratified Atmosphere

We now use the simple example of a dust grain in a stratified atmosphere to illustrate some of the concepts introduced above. Imagine an infinitesimally small particle in a stably stratified atmosphere (Fig. 1.3). The density of the ambient fluid is $\rho(z)$, and the particle is at equilibrium at $z = C$, where $\rho(C) = \rho_p$. The motion of the particle satisfies

$$\ddot{z} = g\frac{\rho(z) - \rho_p}{\rho_p}, \tag{1.18}$$

which can be written in the form,

$$\begin{aligned} \dot{z} &= v \\ \dot{v} &= \frac{g}{\rho_p}(\rho(z) - \rho_p). \end{aligned} \tag{1.19}$$

This is a continuous-time dynamical system with a two-dimensional phase space.

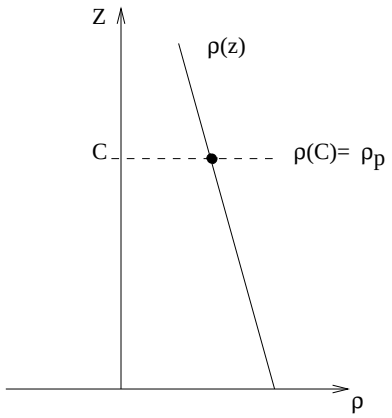

Figure 1.3: An illustration of a dust grain moving in a stratified atmosphere.

1.3.1 Linear stratification

Suppose that $\rho(z) = \alpha(z - C) + \rho(C)$, where α is a constant, and that $\rho(C) = \rho_p$. Then we may choose $C = 0$ with no loss of generality. Then Eq. (1.19) becomes

$$\begin{aligned} \dot{z} &= v \\ \dot{v} &= \frac{g\alpha}{\rho_p} z. \end{aligned} \tag{1.20}$$

This is a linear system and is equivalent to the simple harmonic oscillator.

If the atmosphere is stably stratified, α is negative and we have stable oscillations. The flow in phase space is shown in figure 1.4; this type of picture, which shows the character of typical orbits, is called a phase portrait. The stable oscillations appear as closed circles in the phase portrait. There is a single equilibrium point at $z = v = 0$. Because of the shape of the orbits surrounding this equilibrium, it is called an elliptic fixed point.

When α is positive, the atmosphere is unstably stratified and the particle trajectory exhibits exponential divergence from the fixed point; the phase portrait is shown in Fig. 1.5. The point $z = 0, v = 0$ is now a saddle point; because of the hyperbolic shape of nearby orbits, it is referred to as a hyperbolic fixed point.

The fixed points of the system are the positions of static equilibrium for the dust particle. These points are the solutions $\mathbf{X}_f$ to $\mathbf{F}(\mathbf{X}_f) = 0$. For our illustrative example, $\mathbf{X} = (z, v)$, and the fixed point is given by $(\dot{z}, \dot{v}) = (0, 0)$:

$$\begin{aligned} v &= 0 \\ \rho(z) - \rho_p &= 0. \end{aligned} \tag{1.21}$$

Hence, for a linear stratification, $\rho(z) = \rho_p + \alpha z$, and the fixed point is $z_f = 0$ (linear systems can only ever have a single fixed point).

The linear stability of a fixed point can be examined via linear perturbation analysis, in which one studies the evolution from an infinitesimal displacement from the fixed point. In

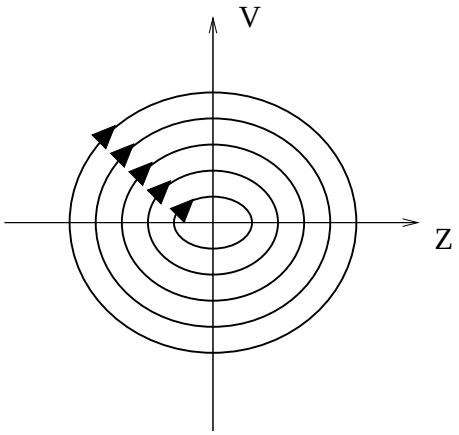

Figure 1.4: Elliptic fixed point

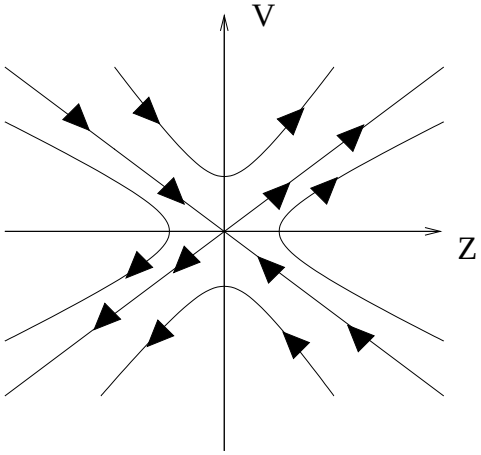

Figure 1.5: Hyperbolic fixed point

general, suppose that $\dot{\mathbf{X}} = \mathbf{F}(\mathbf{X})$ has a fixed point at $\mathbf{X}_f$. Consider a point close to $\mathbf{X}_f$ given by $\mathbf{X} = \mathbf{X}_f + \xi$. Then, $\dot{\xi} = \mathbf{F}(\mathbf{X}_f + \xi)$ which may be expanded in a Taylor series as

$$\begin{aligned} \dot{\xi} &= \mathbf{F}(\mathbf{X}_f) + \left(\frac{\partial \mathbf{F}}{\partial \mathbf{X}}\right)_{\mathbf{X}_f} \xi + \cdots \\ &\approx \left(\frac{\partial \mathbf{F}}{\partial \mathbf{X}}\right)_{\mathbf{X}_f} \xi, \end{aligned} \tag{1.22}$$

where $(\partial \mathbf{F}/\partial \mathbf{X})$ is the Jacobian of $\mathbf{F}$. This is a linear system; the eigenvalues of the Jacobian matrix determine whether the infinitesimal perturbation grows or decays. In other words, stability is only ensured if all the eigenvalues of the Jacobian have negative real part.

For the example above,

$$\begin{aligned} z &= z_f + \zeta \\ v &= v_f + \theta, \end{aligned} \tag{1.23}$$

and

$$\begin{aligned} \dot{\zeta} &= \theta \\ \dot{\theta} &= \frac{g\alpha}{\rho_p}\zeta. \end{aligned} \tag{1.24}$$

Thus the fixed point is stable if $\alpha < 0$, or unstable if $\alpha > 0$, exactly as indicated above. Indeed, since the system is linear in this case, linear stability theory provides information also about the global stability of the fixed point. This example is also rather trivial for precisely this reason. Nonlinear stratifications, however, lead to less trivial dynamics.

1.3.2 Nonlinear stratification

Let us now parameterize the density as $\rho(z) = \rho_0 + \alpha z + \gamma z^3$. Then

$$\begin{aligned} \dot{z} &= v \\ \dot{v} &= \frac{\alpha g}{\rho_p} z + \frac{\gamma g}{\rho_p} z^3, \end{aligned} \tag{1.25}$$

which is a nonlinear system. The fixed points satisfy

$$\begin{aligned} v &= 0 \\ z(\alpha + \gamma z^2) &= 0, \end{aligned} \tag{1.26}$$

the solutions of which are $v = 0$, and $z = z_0 = 0$ or $z = z_{1,2} = \pm\sqrt{-\alpha/\gamma}$. It is clear that $z_{1,2}$ exist only if α and γ have opposite signs.

Phase portraits of the system are shown in Figs. 1.6 and 1.7. In the first case, $\alpha > 0$ and $\gamma < 0$, and there are two elliptic fixed points and one saddle. Orbits either circulate around one of the two elliptic fixed points, or with larger amplitude around all three. There are two

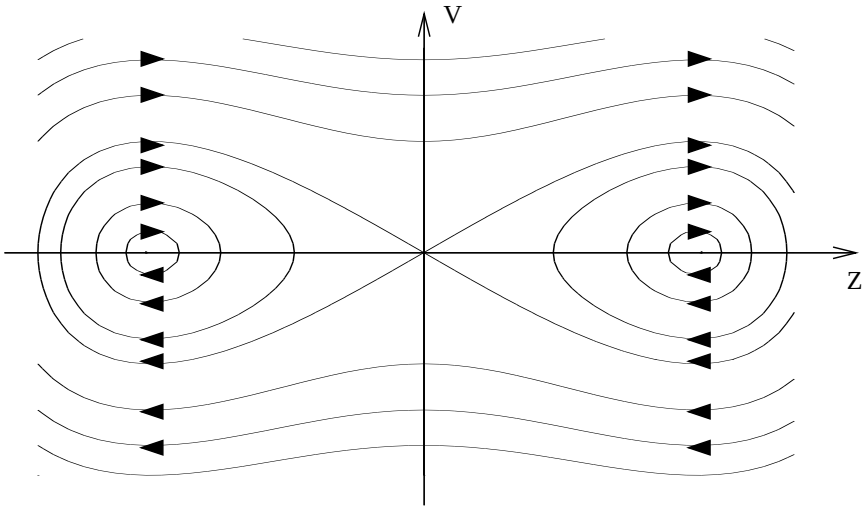

Figure 1.6: Phase space portrait for the nonlinear atmospheric stratification with $\alpha > 0$ and $\gamma < 0$.

special orbits that connect the origin to itself; these are called "separatrices" or "homoclinic orbits", and correspond to trajectories that begin at the origin for $t \to -\infty$, then circulate around one of the elliptic fixed points before returning to the origin for $t \to \infty$.

In the second example, $\alpha < 0$ and $\gamma > 0$, and there are two hyperbolic fixed points beside the elliptic fixed point at the origin. The special orbits that connect the two saddle points are again separatrices; they are also referred to as "heteroclinic orbits". There are only unbounded orbits in this case when the initial condition lies inside the separatrices.

In contrast to the single fixed point of the linear case, the nonlinear system therefore has multiple equilibria. The stability of the fixed points can again be examined using linear stability theory. For the fixed point z_0,

$$\ddot{\xi} = \frac{g}{\rho_p}\alpha\xi, \tag{1.27}$$

the same result as was obtained for the case of linear stratification. For the fixed points $z_{1,2}$, we expand $\ddot{\xi}$ as:

$$\begin{aligned}
\ddot{\xi} &= \frac{g}{\rho_p}\left[\alpha\left(\pm\sqrt{-\frac{\alpha}{\gamma}}+\xi\right)+\gamma\left(\pm\sqrt{-\frac{\alpha}{\gamma}}+\xi\right)^3\right] \\
&= \frac{g}{\rho_p}\left(\pm\alpha\sqrt{-\frac{\alpha}{\gamma}}+\alpha\xi\mp\alpha\sqrt{-\frac{\alpha}{\gamma}}-3\alpha\xi+\cdots\right) \\
&\approx -\frac{2g}{\rho_p}\alpha\xi.
\end{aligned} \tag{1.28}$$

The linear stability of the fixed points $z_{1,2}$ is thus determined by the value of α. If $\alpha < 0$, z_0 is stable and $z_{1,2}$ are unstable. If $\alpha > 0$, z_0 is unstable and $z_{1,2}$ are stable. This parallels

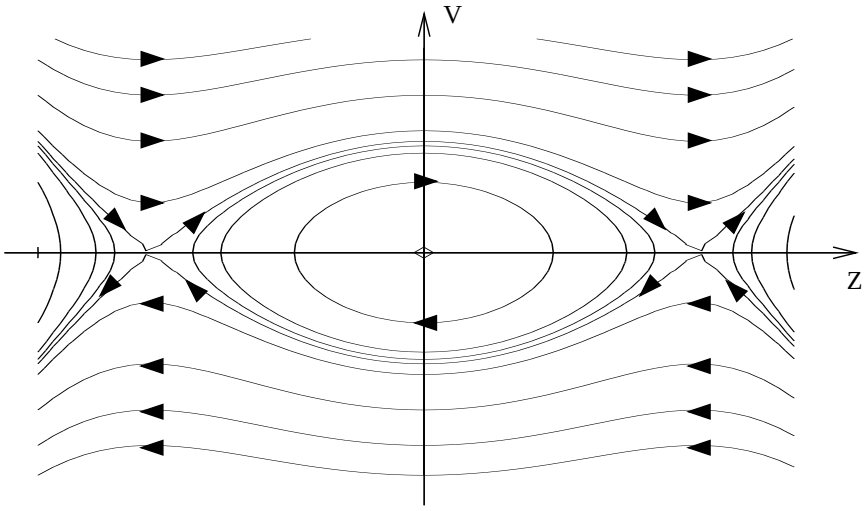

Figure 1.7: As in Figure 1.6, except for $\alpha < 0$ and $\gamma > 0$.

the conclusions one draws from the phase portraits in Figs. 1.6 and 1.7. Note that at leading order, γ does not play a role in the stability result.

1.3.3 Parameter variation

Suppose that in the above example we fix $\gamma < 0$ and vary the parameter α. For $\alpha < 0$, there is only a single fixed point, namely that at the origin. According to equation (1.27), this fixed point is stable. But when $\alpha > 0$, we have three equilibria and a situation like that shown in the phase portrait 1.6. Here the origin is unstable, and the two nontrivial fixed points are stable. In other words, when α passes zero, there is a change in the equilibrium points of the system. This is an example of a bifurcation; that is, a change in the system properties. The particular bifurcation displayed in this example is called a "pitchfork" bifurcation (Fig. 1.8), in which a fixed point loses stability and sheds two new, stable fixed points.

1.3.4 Conservative and Dissipative Systems

The equations (1.19) also form a conservative system. In particular, the energy,

$$H = E = \frac{1}{2}v^2 - \frac{g}{\rho_p}\int [\rho(z) - \rho_p]\, dz, \tag{1.29}$$

is conserved: $\dot{H} = 0$. This system is also Hamiltonian, since the equations may be obtained from

$$\begin{aligned} \dot{z} &= \frac{\partial H}{\partial v} \\ \dot{v} &= -\frac{\partial H}{\partial z}, \end{aligned} \tag{1.30}$$

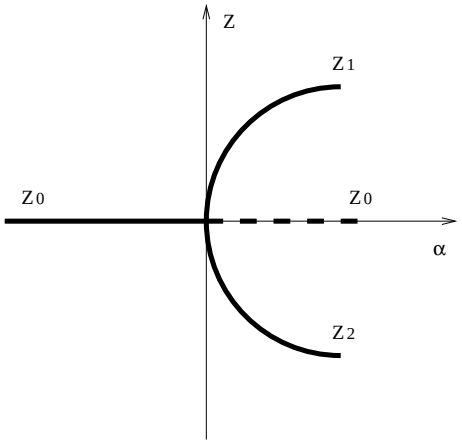

Figure 1.8: "Pitchfork" or "trident" bifurcation of the dust grain example with $\gamma < 0$. For $\alpha < 0$ there exists only one stable fixed point. As α increases beyond 0, three solutions exist: two stable fixed points, z_1 and z_2, and one unstable solution, z_0.

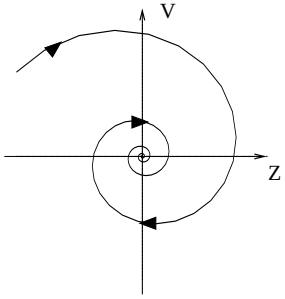

Figure 1.9: Attracting spiral point (focus) for a dissipative nonlinear system

where the Hamiltonian H is just the energy. Note that z and v are canonically conjugate variables.

In the presence of friction, the system becomes dissipative:

$$\ddot{z} = \frac{g}{\rho_p}(\rho(z) - \rho_p) - \mu\dot{z}, \tag{1.31}$$

where $\mu\dot{z}$ is a Stokes drag. In this case, $\dot{E} < 0$, energy is not conserved, and the phase space volume shrinks. An example of such a case is shown in Fig. 1.9. This displays a phase portrait in which there is an attracting spiral point at the origin. In other words, all of the oscillations of the conservative system disappear under the dissipative perturbation leaving only a stable spiral point where the elliptic fixed was once located. If such a damped system is forced, however, the asymptotic state may be a state of motion, such as a limit cycle.

1.4 Bifurcations

One of the key concepts of dynamical systems theory is a *bifurcation*. Basically. this term means simply that as we vary one of the intrinsic properties of the system, a transition takes place in the dynamical behaviour. The threshold at which the transition occurs is *the point of bifurcation*. Before the bifurcation there is one type of dynamical behaviour, and beyond it there is another.

In the flow of fluids down a pipe, for example, we might vary the viscosity or the forcing pressure gradient. Either way, we have a control parameter, the Reynolds number, that we vary in order to observe changes in the fluid dynamics. For low Reynolds number, the flow is laminar. But beyond a certain threshold, the fluid motion becomes turbulent, and this is one example of a bifurcation.

Another example is in fluid convection. Here we confine a fluid between two plates and impose a vertical temperature gradient (see lecture 2). As we ramp up this gradient by heating the two plates to a stronger and stronger temperature difference, we observe a bifurcation - the onset of fluid convection.

In dynamical systems theory, bifurcations are classified. One of the most important features of nonlinear systems is that many bifurcations are universal. That is, many transitions have a common form, independently of the physical system in which they take place. Thus, from an understanding of the most common types of bifurcations, we can understand many behavioural transitions.

It is presumably from such simple dynamics that we ultimately build up to the extensive, violently unstable systems in which we observe turbulent cascades over many scales of motion, and the emergence of coherent structures. More specifically, turbulence is usually thought to originate as a result of a bifurcation sequence that leads from a simple, regular or laminar flow to the turbulent state. Part of this sequence is the famed "transition to chaos". But the sequence itself, is merely a succession of known types of bifurcations.

The main types of bifurcations encountered in low-order dynamical systems that we shall mention in these lectures are the following:

Pitchfork bifurcation: We have already encountered this type of bifurcation. It corresponds to a situation in which an equilibrium point changes its stability by shedding two new ones. In the example considered earlier, the original equilibrium lost stability, and the two new fixed points were stable. This situation is called a *supercritical* pitchfork bifurcation. When the new equilibria are unstable, they co-exist with the stable equilibrium, and the pitchfork is *subcritical*.

Hopf bifurcation: In the simplest form of a Hopf bifurcation, a fixed point loses stability by shedding a limit cycle. That is, the equilibrium loses stability to perturbations that take the form of growing oscillations. In a *supercritical Hopf bifurcation*, the growing oscillations saturate on a nearby limit cycle. But for *subcritical Hopf bifurcations*, an unstable limit cycle collides with the stable fixed point, leaving it unstable beyond the bifurcation.

Period doubling bifurcation: A limit cycle may undergo a bifurcation where its basic period doubles, and the system "makes two turns" on nearby loops before returning to the initial position. A period-doubling bifurcation is revealed by the appearance of sub-harmonics

in the power spectrum of the system. A celebrated scenario of transition to chaos is based on a sequence of period doubling bifurcations, during which the basic period T is modified as $T \to 2T \to 4T \to ... \to 2^n T$ until chaotic behavior (associated with $n \to \infty$) is met.

1.5 Poincaré and stroboscopic maps

When the dimension of the dynamical system becomes larger than two, it is no longer possible to visualize the behaviour of typical orbits in terms of simple phase portraits like those shown in figures 1.6 and 1.7; projections of the solution onto a plane often obscures the structure of the attractor. Instead, we must develop other tools; one such tool is the Poincaré section.

Consider a simple flow of the form:

$$\frac{d\mathbf{X}}{dt} = \mathbf{F}(\mathbf{X}), \quad \mathbf{X} = (x, y, z). \tag{1.32}$$

The Poincaré section (Fig.1.10) of such a flow is formed by finding the intersections of a trajectory with a given surface or "manifold" in the phase space. This manifold is the "surface of section". It is sometimes useful to further take only those intersections with the same directionality with respect to the manifold. (Clearly, one requires the selected manifold to be nowhere tangent to the trajectory.) The set of intersection points is the Poincaré section. Given these points, we may then associate a dynamical law that maps one intersection point into the following one. This is the "Poincaré map" on the particular surface of section.

The Poincaré map (1.33) reduces a system from continuous to discrete time, and from dimension N to dimension $N-1$. Thus, one goes from $\dot{\mathbf{X}} = \mathbf{F}(\mathbf{X})$, $\mathbf{X} \in \mathbb{R}^N$, to $\xi_{n+1} = f(\xi_n)$, $\xi_n \in \mathbb{R}^{N-1}$, where ξ_n is the n-th intersection of $\mathbf{X}(t)$ with the selected manifold:

$$X(t) \to \xi_n, \ n = 1, 2, \cdots, \ X \in \mathbb{R}^N, \ \xi_n \in \mathbb{R}^{N-1} \tag{1.33}$$

Another type of map is the stroboscopic map, obtained by reducing the trajectory to a series of snapshots taken at equal intervals of time. In this case, one goes from $\dot{\mathbf{X}} = \mathbf{F}(\mathbf{X})$ to $\eta_{n+1} = g(\eta_n)$ where $\eta_n = \mathbf{X}(t_0 + n\Delta t)$. For stroboscopic maps, the dimensionality of the system is not reduced.

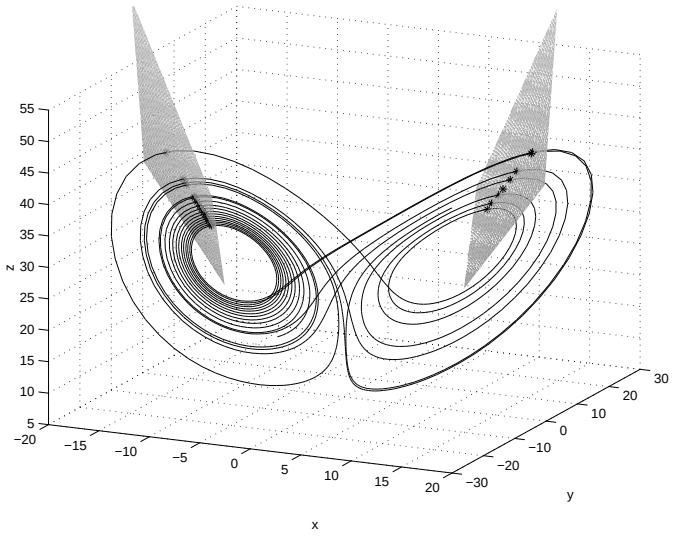

(a)

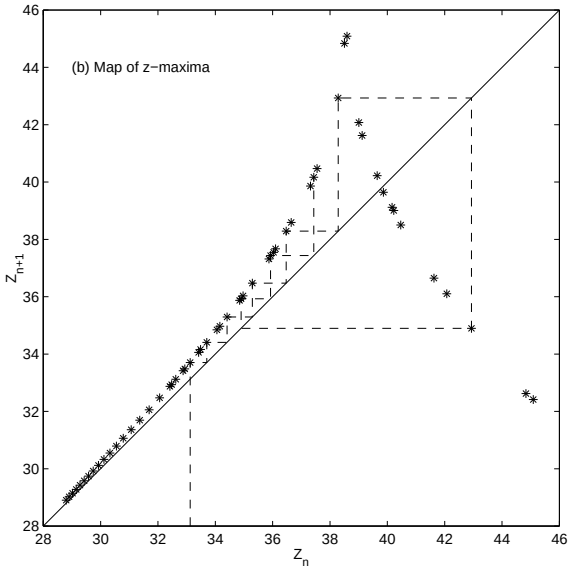

(b)

Figure 1.10: Poincaré section and map. Panel (a) shows the trajectory of a solution to the Lorenz equations (see lecture 2), with a Poincaré section determined by the maxima of z: $xy - 8z/3 = 0$. The values of z determined from each intersection with this manifold, Z_n, are plotted as a map, $Z_{n+1} = Z_{n+1}(Z_n)$ in panel (b). The stars in panel (a) show the intersection points.

Lecture 2

Multiple equilibria, limit cycles and strange attractors

In this lecture we introduce some of the classic low-order geophysical models exhibiting multiple equilibria, limit cycles and chaos.

2.1 Energy-balance models of the global climate

The global climate shows variability on many different time scales. Indirect observations (using the ratio of oxygen isotopes ^{16}O and ^{18}O in deep-sea sediment cores) provide an indication of past temperatures. In the quaternary period the average temperature has fluctated by several degrees on timescales of hundreds of thousands of years, coinciding with periods of widespread glaciation and deglaciation. These and other evidences indicate that the global climate is capable of producing internal fluctuations and amplifying external forcings.

Simple models have been proposed in order to develop some understanding of the global climate (see, for example, Ghil & Childress 1987 for a review). We now derive the simplest of these models, which includes only the energy balance between incoming solar radiation and its re-radiation back into space from the Earth's surface.

From the first law of thermodynamics we have

$$\Delta E = Q_{in} - Q_{out} = c\Delta T, \tag{2.1}$$

where ΔE is the change in the internal energy of the system, induced by difference between the incoming energy Q_{in} and the outgoing energy Q_{out}. The change in internal energy has been parameterized as $\Delta E = c\Delta T$ where ΔT is the change in the temperature of the system and c is the specific heat. In the time Δt we have

$$c\frac{\Delta T}{\Delta t} = \mathcal{F}_{in} - \mathcal{F}_{out}, \tag{2.2}$$

where $\mathcal{F}_{in,out} = \frac{Q_{in,out}}{\Delta t}$ are the incoming and outgoing heat fluxes. By taking the limit $\Delta t \to 0$ we obtain

$$c\frac{dT}{dt} = \mathcal{F}_{in} - \mathcal{F}_{out}. \tag{2.3}$$

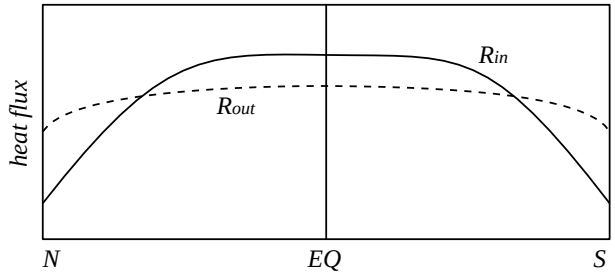

Figure 2.1: Sketch of observed dependence of radiation balance on latitude (redrawn from Ghil & Childress 1987)

The incoming flux $\mathcal{F}_{in}$ is at short wavelengths, whilst the outgoing flux is at longer wavelengths, primarily in the infrared.

The total incident power per unit area of solar radiation is referred to as the "solar constant", S. At the top of the atmosphere, $S = 1.368kW/m^2$ (with a variation of 3.5% due to the ellipticity of the Earth's orbit). This incoming radiation is partly absorbed, and partly reflected back into space. The proportion reflected is given by the albedo parameter α. This parameter varies with both position and time because land, sea, ice and clouds all reflect light differently. However, for simplicity, we take a global, average value: $\alpha = 0.3$.

The total solar energy reaching the Earth per unit time is $\pi R^2 S$ (where R is the radius of the Earth), giving on average a flux of $\pi R^2 S / 4\pi R^2 = \frac{1}{4}S$ at the top of the Earth's atmosphere. The total absorbed flux is therefore $\mathcal{F}_{in} = \frac{1}{4}S(1-\alpha)f(\phi) \approx 240 f(\phi) W/m^2$, where $f(\phi)$ is a latitude correction accounting for geometrical projection.

The outgoing flux can be found by using a modification of Stefan-Boltzmann law, giving $\mathcal{F}_{out} = g(T)\sigma T^4$, where $g(T)$ is a 'greyness' correction to account for the fact that the Earth is not a perfect black body.

If we assume a local equilibrium ($\mathcal{F}_{in} = \mathcal{F}_{out}$) we obtain

$$\frac{1}{4}S(1-\alpha)f(\phi) = g(T)\sigma T^4. \tag{2.4}$$

This expression predicts equilibrium temperatures of $270K$ at the equator, $170K$ at the north pole and $150K$ at the south pole. The average temperature predicted by (2.4) is significantly underestimated due to the omission of the atmospheric greenhouse effect, which raises global temperatures by inhibiting the transmission of thermal radiation from the surface into space. This simple calculation also predicts a much larger difference between polar and equatorial temperatures than that seen on the Earth - this is due to neglecting the mean transport of heat from the tropics to the polar regions by atmospheric and oceanic circulation. The difference between the observed values of $\mathcal{F}_{in}$ and $\mathcal{F}_{out}$ as a function of latitude (see Figure 2.1) provides means of estimating the meridional heat transport of the ocean and atmosphere, as shown in Figure 2.2. More sophisticated analyses have estimated the proportions of this transport due to the oceanic circulation and the mean and fluctuating atmospheric circulation.

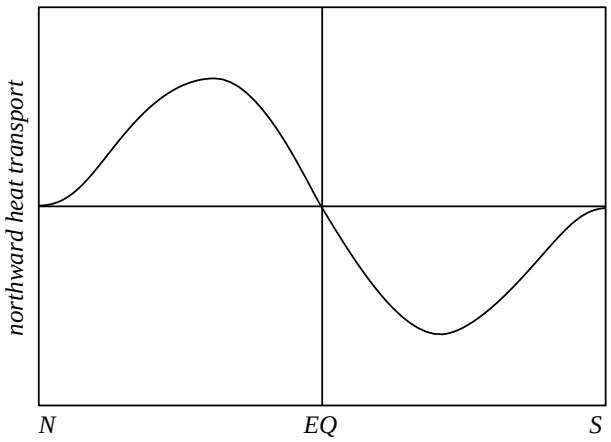

Figure 2.2: Sketch of atmospheric and oceanic heat transport versus latitude, deduced from local radiation imbalances (redrawn from Ghil & Childress 1987)

2.1.1 The effect of temperature-dependent albedo

We now consider the globally averaged energy balance, at first ignoring, for simplicity, the greyness factor. The energy balance in stationary conditions then becomes

$$\frac{1}{4}S(1-\alpha) = \sigma T^4,$$

which has the unique, physically meaningful solution,

$$T_0 = \left[\frac{S(1-\alpha)}{4\sigma}\right]^{\frac{1}{4}}.$$

The average albedo α depends, however, on temperature. When the temperature is low and ice covers a large fraction of the Earth, the albedo is larger than for an ice-free Earth. Denoting by α_f and α_i the albedos corresponding to a minimal and maximal ice cover respectively, we can approximate the ice-albedo feedback as

$$\alpha(T) = \alpha_i, \quad T \leq T_i,$$

$$\alpha(T) = \alpha_f, \quad T \geq T_f$$

and

$$\alpha(T) = \alpha_i + (\alpha_f - \alpha_i)\frac{T - T_i}{T_f - T_i}, \quad T_i < T < T_f,$$

where T_i is the temperature below which ice has its maximum extend, and T_f is the temperature above which ice has its minimal extent.

The dependence of albedo on temperature can result in multiple equilibria, in contrast to the case of a constant albedo in which only one equilibrium is possible. The energy balance can

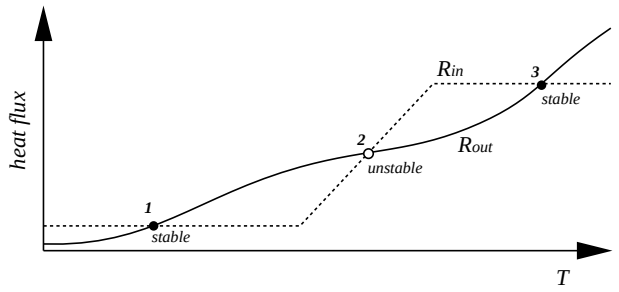

Figure 2.3: Fixed points of a simple energy-balance climate model (redrawn from Ghil & Childress 1987)

be solved graphically by plotting $\mathcal{F}_{out}$ and $\mathcal{F}_{in}$ as functions of T and looking for intersections of the two curves (see figure 2.3, where a greyness correction to $\mathcal{F}_{out}$ has also been included). The number of fixed points depends on the values of the parameters chosen. When we have three fixed points as in figure 2.3, a linear stability analysis shows that point 2 is unstable and points 1 and 3 are stable. The instability of point 2 is due to the positive feedback between ice and albedo: a small temperature increase will reduce the extent of ice cover, reducing the albedo and increasing the temperature still further.

This example demonstrates the existence of multiple equilibria even for very simple nonlinear models. Note that the phase space of the above model is one-dimensional, as the dynamics is fully described by the global temperature T. For one-dimensional dissipative systems with continuous time and without an explicit time-dependent external forcing (i.e., an autonomous ordinary differential equation), stationary equibria (fixed points) are the only possible attractors.

2.1.2 Ice-sheet dynamics

The simple model described above displays multiple equilibria but it does not have any time-dependent behavior in its asymptotic states. In order to obtain self-sustained oscillations (i.e., limit cycles) in an autonomous system, at least a phase space of at least two dimensions is required.

In order to produce self-sustained climatic oscillations, we thus need a second dynamical variable to be coupled with global temperature. One way to achieve this is to include the dynamics of the ice sheets. Consider an idealized ice sheet as shown in figure 2.4.

The air temperature is assumed to decrease with altitude and with latitude, leading to accumulation of ice above the $0°C$ isotherm and ablation below it. The ice sheet is bounded on the northern side by the ocean, which is assumed to prevent the growth of the ice sheet on that side. Thus we shall consider only the variation in the extent L of the ice sheet to the right of the midpoint. If the height h of the ice sheet above ground varies with north-south position y according to

$$h(y) = \lambda^{\frac{1}{2}}(L - |y|)^{\frac{1}{2}},$$

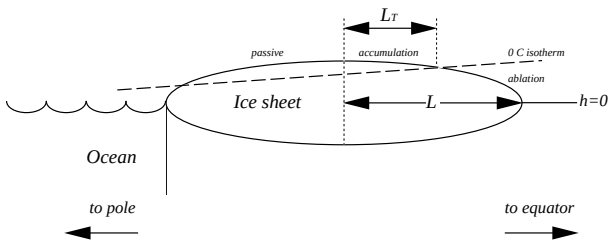

Figure 2.4: Idealized model of an ice sheet (redrawn from Ghil & Childress 1987).

then the volume of ice is

$$V = 2c_L\lambda^{\frac{1}{2}}L^{\frac{1}{2}}\int_0^L \left(1 - \frac{|y|}{L}\right)^{\frac{1}{2}} dy = \frac{4}{3}\lambda^{\frac{1}{2}}L^{\frac{3}{2}}c_L,$$

where c_L measures the longitudinal extent of the ice sheet.

The rate of change of ice volume can be written as $\dot{V} = aA - a'A'$, where $A = c_L L_T$ is the area with accumulation at the rate a, and $A' = c_L(L - L_T)$ is the area with ablation at the rate a'. This gives

$$\dot{V} = c_L a'[\epsilon L_T - (L - L_T)],$$

where $\epsilon = \frac{a}{a'}$. This expression can be used to find the rate of change of the extent of the ice sheet:

$$\dot{L} = \frac{a'}{2\lambda^{\frac{1}{2}}L^{\frac{1}{2}}}[(1+\epsilon)L_T - L]$$

where L_T is a given function of L and of the (fixed) slope of the $0°C$ isotherm.

The variation in ice cover influences the energy balance through changes in albedo. The global average albedo can be written as

$$\alpha = \gamma(\alpha_0 + \alpha_1\mu) + (1-\gamma)\alpha_{oc}(T),$$

where γ is the fraction of the earth's surface covered by land, and α_0 and α_{oc} are the albedo of the land and ocean, respectively. The quantity μ represents the fraction of land covered by ice, and α_1 is the correction to the albedo of the land due to the presence of ice.

The precipitation is supposed to increase with temperature, resulting in an increase in ϵ, the ratio of accumulation and ablation rates. The positive feedback of T on ϵ is a crucial but delicate point of this model. The hypothesis behind this choice is that increased temperatures produce both a more active hydrological cycle (more precipitation) and more melting of the ice sheet, but the ratio of the two effects is such that more ice is formed than melted when increasing T. The real dependence of ϵ on T is, of course, very complicated, and at high temperatures ϵ is clearly decreasing for increasing T. The choice $\epsilon \sim T$ should thereby be taken as a local approximation to $\epsilon(t)$ in the small range of temperature where the model is applied. The system of equations which results from coupling the energy balance model of the

previous section with the ice model is

$$\begin{cases} c\dot{T} = Q[1-\gamma(\alpha_0+\alpha_1\mu)-(1-\gamma)\alpha_{oc}(T)]-\sigma g T^4 \\ c'\dot{L} = \frac{1}{L^{\frac{1}{2}}}\{[1+\epsilon(T)]L_T(L,T)-L\}. \end{cases} \tag{2.5}$$

It is clear from the first equation that $\dot{T} \sim -\alpha$, so $\dot{T} \sim -L$ since $\alpha \sim L$. The second equation shows that $\dot{L} \sim \epsilon$. Since ϵ grows with T (an increase in temperature leads to increased precipitation and more accumulation) we have $\dot{L} \sim T$. These equations can be combined to yield $\ddot{T} \sim -T$, the equation for an oscillator. Using parameters appropriate to the earth, this system shows oscillations with a period of a few thousand years and an amplitude of a few degrees Celsius. Note that these temperature fluctuations have a period much shorter than the glacial-interglacial time scale, and thus describe other forms of climate variability. The amplification of external disturbances by climate variability on the glaciation time scales will be reconsidered in lecture 4.

On more general grounds, we recall that autonomous, two-dimensional dissipative dynamical systems with continuous time may display only stationary equilibria or limit cycles at asymptotically large times (the dynamics is deterministic implying that orbits cannot cross at any time, but the phase space is a plane, so points or closed curves are the only non-intersecting geometrical objects with dimension less than 2). More complicated attractors, such as quasi-periodic motions and chaotic behavior, require at least three dimensions in phase space if the system dynamics is described by ordinary differential equations (ODEs). In the following section, we introduce a classic three-dimensional dynamical system displaying chaotic behavior.

2.2 Rayleigh-Benard convection

We now discuss a classic example of a chaotic low-dimensional dynamical system, namely, the Lorenz (1963) model for Rayleigh-Benard convection.

Consider the behaviour of a layer of viscous fluid under gravity, contained between rigid horizontal plates (see figure 2.2). The plates are separated by a distance D and maintained at temperatures T_1 and T_2 at the top and bottom, respectively.

For a fluid with coefficient of thermal expansion $\alpha > 0$ we have denser fluid overlying less dense fluid when $T_2 - T_1 > 0$. The flow which results from this heating depends on the Rayleigh number $Ra = \frac{g\alpha D^3(T_2-T_1)}{\nu\kappa}$, where g is the acceleration due to gravity, ν is the kinematic viscosity of the fluid and κ is its thermal conductivity. The behaviour of this system as a function of Ra is illustrated in figure (2.2). For small Ra, heat is transferred between the plates purely by conduction and there is no motion in the fluid (case (a)). If the Rayleigh number exceeds a critical value the conductive solution becomes unstable and steady convection cells are formed, as shown in case (b). With a further increase of Ra the cells start to oscillate (case (c)) and further increases lead to quasiperiodic and/or chaotic motion. When Ra is sufficiently large the convection becomes turbulent, as illustrated in case (d).

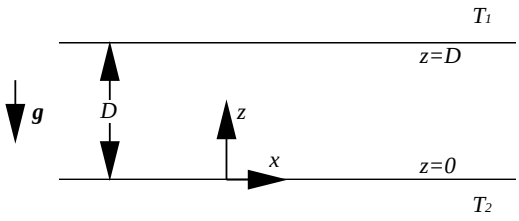

Figure 2.5: Fluid layer contained between two rigid horizontal plates kept at different temperatures.

2.2.1 Derivation of the Lorenz model

The Navier-Stokes equations for an incompressible fluid of density ρ in a gravitational field $\mathbf{g}$ are

$$\rho\frac{\partial \mathbf{u}}{\partial t} + \rho\left(\mathbf{u}\cdot\nabla\right)\mathbf{u} = -\nabla p + \mu\nabla^2\mathbf{u} + \mathbf{g}\Delta\rho \tag{2.6}$$

and

$$\nabla\cdot\mathbf{u} = 0, \tag{2.7}$$

where $\mathbf{u}$ is velocity, p is pressure, μ is viscosity and $\Delta\rho = \rho - \rho_0$ is the local difference in density from the reference value ρ_0. The quantity $\Delta\rho$ can be expressed in terms of the difference ΔT from the temperature at which $\Delta\rho = 0$:

$$\Delta\rho = -\rho_0\alpha\Delta T. \tag{2.8}$$

This system of equations is closed by the heat equation

$$\frac{\partial T}{\partial t} + \left(\mathbf{u}\cdot\nabla\right)T = \kappa\nabla^2 T, \tag{2.9}$$

where κ is the thermal diffusivity.

Next we use the Boussinesq approximation to simplify equation (2.6). This assumes that $\Delta\rho \ll \rho$, so we can replace ρ by ρ_0 on the left-hand side of (2.6), retaining the density variations only in the third (buoyancy) term on the right-hand side. The resulting equation is

$$\frac{\partial \mathbf{u}}{\partial t} + \left(\mathbf{u}\cdot\nabla\right)\mathbf{u} = -\frac{1}{\rho_0}\nabla p + \nu\nabla^2\mathbf{u} - \mathbf{g}\alpha\Delta T, \tag{2.10}$$

where $\nu = \mu/\rho_0$ is the kinematic viscosity and the equation of state (2.8) has been incorporated into the final term. Taking the curl of (2.10) yields an equation for the vorticity $\boldsymbol{\omega} \equiv \nabla\times\mathbf{u}$:

$$\frac{\partial \boldsymbol{\omega}}{\partial t} + \left(\mathbf{u}\cdot\nabla\right)\boldsymbol{\omega} = \left(\boldsymbol{\omega}\cdot\nabla\right)\mathbf{u} + \nu\nabla^2\boldsymbol{\omega} - \alpha\nabla\times\left(\mathbf{g}\Delta T\right). \tag{2.11}$$

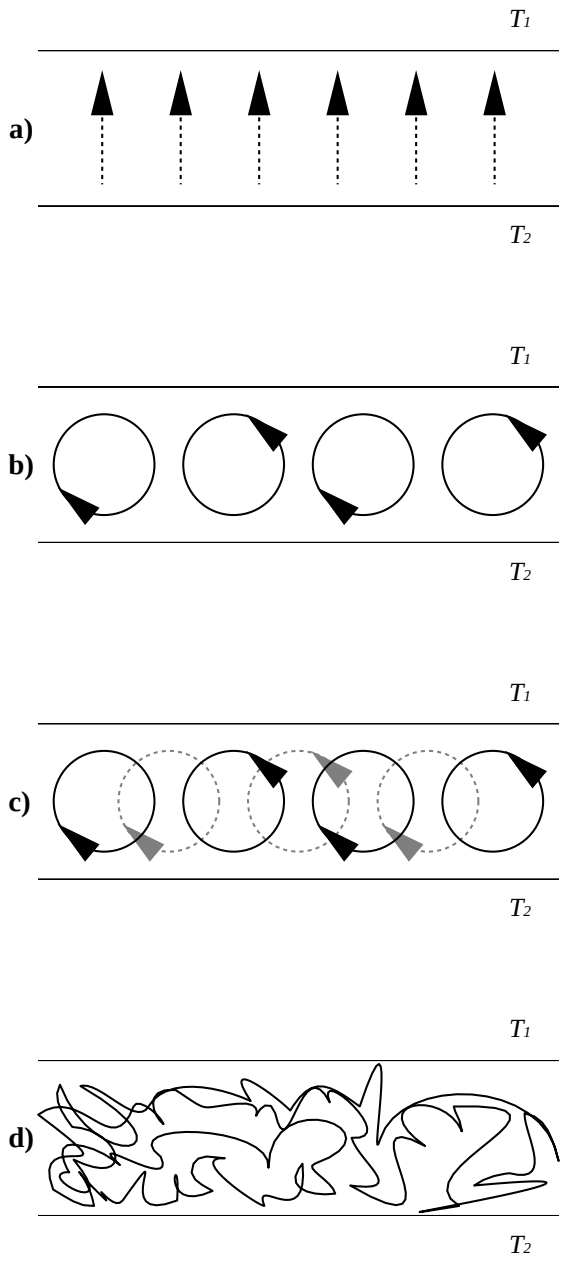

Figure 2.6: Transition to turbulent motion in a fluid layer between two rigid boundaries as the Rayleigh number Ra is increased. (a): conduction only; (b): steady convection; (c): time-dependent convection; (d): turbulent convection.

If we choose Cartesian coordinates so that $\mathbf{g} = (0, 0, -g)$ and assume that all the fields are independent of y, then the vorticity has a non-zero component only in the y direction, $\omega = (0, \omega, 0)$, and (2.11) becomes the scalar equation

$$\frac{\partial \omega}{\partial t} + (\mathbf{u} \cdot \nabla)\, \omega = \nu \nabla^2 \omega - g\alpha \frac{\partial \Delta T}{\partial x}. \tag{2.12}$$

where now the velocity is zero in the y direction, i.e. $\mathbf{u} = (u, 0, w)$. Note that the assumption of two-dimensionality eliminates the first term (vortex stretching) on the right hand side of (2.11). Since the velocity is now two-dimensional and incompressible, it can be written in terms of a streamfunction ψ as $u = \partial\psi/\partial z$ and $w = -\partial\psi/\partial x$. The scalar vorticity is related to ψ by the Poisson equation $\omega = \nabla^2\psi$, allowing the vorticity equation (2.12) to be written in terms of ψ as

$$\frac{\partial \nabla^2 \psi}{\partial t} - [\psi, \nabla^2 \psi] = \nu \nabla^4 \psi - g\alpha \frac{\partial \Delta T}{\partial x}, \tag{2.13}$$

where $[a, b] \equiv \frac{\partial a}{\partial x}\frac{\partial b}{\partial z} - \frac{\partial a}{\partial z}\frac{\partial b}{\partial x}$ is the two-dimensional Jacobian operator.

We now write the temperature field T in terms of a background profile $\overline{T}$ which depends only on z and a perturbation θ:

$$T(x, z, t) = \overline{T}(z) + \theta(x, z, t).$$

The heat equation (2.9) then takes the form

$$\frac{\partial \theta}{\partial t} - [\psi, \theta] - \frac{\partial \psi}{\partial x}\frac{\partial \overline{T}}{\partial z} = \kappa \nabla^2 \theta + \kappa \frac{\partial^2 \overline{T}}{\partial z^2}.$$

In the absence of convection ($\psi = 0$), a linear temperature profile is a stationary solution of the equations of motion. Thus, if we assume a linear background temperature profile of the form,

$$\overline{T} = T_2 + \frac{T_1 - T_2}{D} z,$$

the equation for θ becomes

$$\frac{\partial \theta}{\partial t} - [\psi, \theta] - \frac{\partial \psi}{\partial x}\frac{T_1 - T_2}{D} = \kappa \nabla^2 \theta. \tag{2.14}$$

The governing equations for this system are (2.13) and (2.14).

Conditions of no slip and no normal flow at the upper and lower boundaries imply that $\psi = \nabla^2\psi = 0$ on $z = 0, D$. The temperature at the top and bottom boundaries is fixed, so $\theta = 0$ on $z = 0, D$.

2.2.2 Expansion in Fourier Modes

Given a nonlinear system of partial differential equations:

$$\partial_t \omega = L\omega + N(\omega),$$

where L and N are linear and nonlinear operators respectively, the variable ω can be written as a combination of the eigenmodes $\Phi_j(x)$ of the linear operator (constant in time):

$$\omega = \sum_j a_j(t)\Phi_j(x)$$

and the dynamics is described by the time dependence of the expansion coefficients $a_j(t)$:

$$\frac{da_j}{dt} = \mathcal{F}(\{a_j\}),$$

which is a set of an infinite number of coupled ordinary differential equations.

As an example, the method is applied to a modified Burgers equation:

$$\frac{\partial u}{\partial t} + c\frac{\partial u}{\partial x} + \alpha u\frac{\partial u}{\partial x} = \nu\frac{\partial^2 u}{\partial x^2},$$

with periodic boundary conditions $u(0,t) = u(2\pi,t)$. The eigenmodes of the linear operator are the Fourier modes e^{inx} and the equation becomes:

$$\sum_{n=-\infty}^{\infty}(\dot{a}_n + incu_n)e^{inx} + \sum_{l=-\infty}^{\infty}\sum_{m=-\infty}^{\infty}\alpha a_l ima_m e^{i(l+m)x} = \sum_{n=-\infty}^{\infty}(-\nu n^2)a_n e^{inx}.$$

Considering $l+m=n$, the exponential term e^{inx} can be eliminated and the sum can be split into an infinite number of equations:

$$\dot{a}_n + incu_n + \sum_{l=-\infty}^{\infty} i\alpha(n-l)a_l a_{n-l} = -\nu n^2 a_n.$$

From a numerical perspective, only a finite number of these equations can be solved and so a truncation of the higher order modes is usually performed.

2.2.3 The Lorenz '63 model

It is possible to obtain a simple dynamical model for Rayleigh-Benard convection by expanding equations (2.13) and (2.14) in terms of three Fourier modes. As mentioned above, we assume no slip and no normal flow boundary conditions, i.e., $\psi = \nabla^2\psi = 0$ on $z = 0, D$. The thermal boundary condition is $\theta = 0$ on $z = 0, D$. If we assume ψ and θ to be periodic in x, then they can be represented in terms of infinite Fourier sums. By retaining only the first Fourier mode for the stream function ψ and the first two modes for the temperature θ, we may write the variables as

$$\psi = \frac{(1+a^2)k\sqrt{2}}{a}X\sin(\pi a\xi)\sin(\pi\zeta),$$

$$\theta = \frac{Ra_{cr}(T_1-T_2)}{\pi Ra}[\sqrt{2}Y\cos(\pi a\xi)\sin(\pi\zeta) - Z\sin(2\pi\zeta)],$$

where $\xi = X/D$, $\zeta = Z/D$, a is the aspect ratio of the unstable perturbation, and $Ra_{cr} = \pi^4(1+a^2)^3/a^2$ is the critical Rayleigh number at which the conductive solution becomes unstable to convection.

By substituting the truncated Fourier expansions of ψ and θ into equations (2.13) and (2.14) we obtain three coupled ordinary differential equations for the coefficients X, Y and Z of the expansion:

$$\begin{cases} \dot{X} = -\sigma X + \sigma Y \\ \dot{Y} = -XZ + RX - Y \\ \dot{Z} = XY - bZ, \end{cases} \tag{2.15}$$

where the differentiation refers to the nondimensional time $\tau = \pi^2(1+a^2)kt/H^2$, $R = Ra/Ra_{cr}$ is a normalised Rayleigh number, $b = 4/(1+a^2)$ is related to the aspect ratio of convective cells, and $\sigma = \nu/k$ is the Prandtl number. X is proportional the intensity of the convective motion, Y is proportional to the difference in temperature between the upgoing and downgoing currents, and Z describes the horizontally averaged deviation from the linear temperature profile. This is a dissipative system, since its divergence is negative:

$$\partial_x \dot{X} + \partial_y \dot{Y} + \partial_z \dot{Z} = -\sigma - 1 - b < 0,$$

implying that the volume of the attractor in the three-dimensional phase space is zero.

Fixed points are given by the system:

$$\begin{cases} X - Y = 0 \\ -XZ + (R-1)X = 0 \\ XY - bZ = 0. \end{cases} \tag{2.16}$$

For $R < 1$ there is only one fixed point $\mathbf{X}_0$, $X_0 = Y_0 = Z_0 = 0$, corresponding to a linear (conductive) temperature profile, with no convection.

For $R > 1$ there are two additional fixed points $\mathbf{X}_1$ and $\mathbf{X}_2$, $X_1 = Y_1 = \sqrt{b(R-1)}$, $Z_1 = R - 1$, and $X_2 = Y_2 = -\sqrt{b(R-1)}$, $Z_2 = R - 1$, corresponding to steady convection in parallel rolls.

By a linear stability analysis it can be shown that $\mathbf{X}_0$ is the only stable fixed point for $R < 1$; at $R = 1$ there is a pitchfork bifurcation in which $\mathbf{X}_0$ becomes unstable and $\mathbf{X}_1$ and $\mathbf{X}_2$ appear as new, stable equilibria. If $\sigma > b + 1$, $\mathbf{X}_1$ and $\mathbf{X}_2$ become unstable through a subcritical Hopf bifurcation at $R = R_c = \frac{\sigma(\sigma+b+3)}{\sigma-b-1}$. The consequence of the disappearance of the stable fixed point is chaotic motion (see Sparrow, 1982). In the phase space the attractor of the system (figure 2.7) is a "strange" object, with a non-integer fractal dimension (see below). Roughly speaking, the trajectory of the solution follows a path in phase space that spirals away from one unstable fixed point (say, $\mathbf{X}_1$), then loops in close to the other unstable fixed point ($\mathbf{X}_2$). It then spirals away from this second unstable focus until it loops back to the

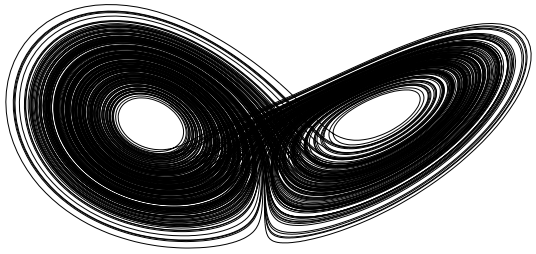

Figure 2.7: Lorenz attractor with $R = 28$, $\sigma = 10$, $b = 8/3$. Shown is the path of the orbit in the phase space (X, Y, Z).

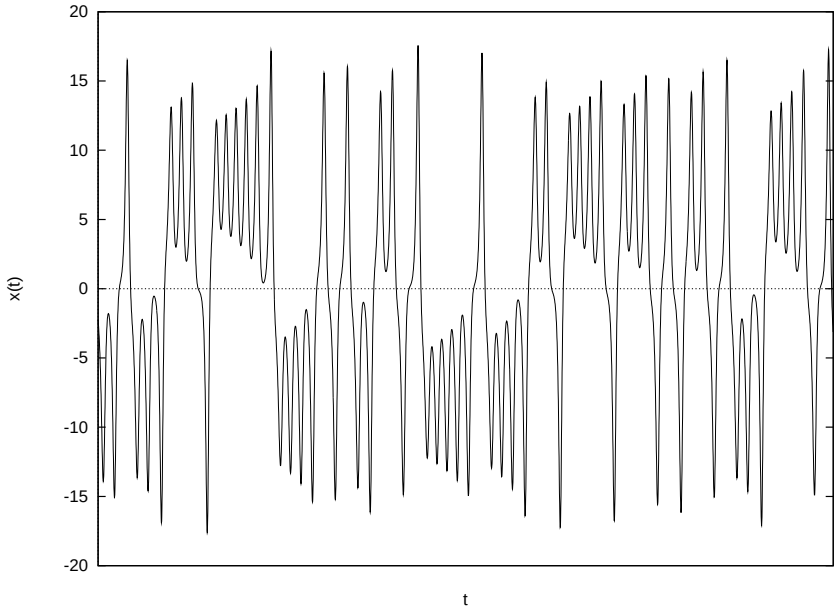

Figure 2.8: Time series of X from the Lorenz system with $R = 28$, $\sigma = 10$, $b = 8/3$.

neighbourhood of the first unstable fixed point. The switching between orbiting around one unstable fixed point and the other follows an irregular, aperiodic sequence.

The time dependence of the X variable is shown in figure 2.8. Note the irregular transitions from positive to negative values of X, corresponding to the system orbiting around one or the other unstable fixed point.

Trajectories started from nearby points on the strange attractor diverge rapidly from one another, though they remain on the attractor. This sensitivity to initial conditions makes prediction of the trajectory impossible in practice even though the system is deterministic. This is the origin of the popular vision of the "butterfly effect" in weather prediction.

2.3 Properties of strange attractors

Strange attractors are intimately associated with chaotic dynamics and unpredictability in dissipative systems. Roughly speaking, a strange attractor is a collection of an infinite number

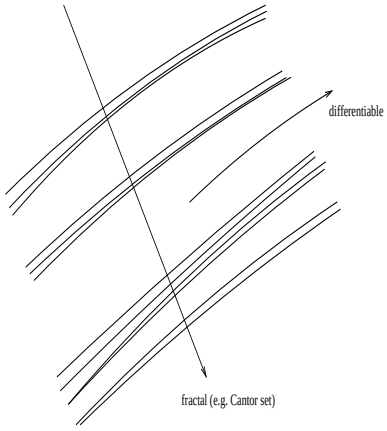

Figure 2.9: Fractal Structure of a Strange Attractor

of unstable periodic orbits that is, in some sense, globally attractive. Geometrically, these objects are very complicated. Chaotic motion can crudely be thought of as the motion of the trajectory of the system as it meanders through this collection of unstable orbits, wandering close to one orbit at one time, then switching to the neighbourhood of another in an apparently random fashion.

There are two basic properties of strange attractors that lead to measures that can be used to characterize these objects. The properties are:

- Sensitive dependence on initial conditions. This sensitivity can be quantified by a "Lyapunov exponent", the exponential rate of divergence of neighbouring trajectories in phase space (evidently, for chaos, this exponent must be positive).
- Fractal structure. Fractals can be characterized by a "Hausdorff dimension" which is not integer and is (usually) larger than the "topological dimension". This feature is associated with the self-similarity (self-affinity) of such geometrical structures.

We discuss these properties more completely below.

In the lectures, we use the term strange attractor to indicate a chaotic attractor with sensitive dependence on initial conditions. Although there are non-fractal chaotic attractors, as well as fractal non-chaotic attractors, in most systems chaotic attractors have a fractal nature. A pictorial image of this structure is shown in figure 2.9.

2.3.1 Lyapunov exponents

Here, we encounter for the first time the issue of predictability in dynamical systems. Given a deterministic dynamical system, we can calculate a future state, say $\mathbf{X}(t)$, from the knowledge of its state at a given time, say $\mathbf{X}_0 = \mathbf{X}(0)$, by (analytically or numerically) solving the equations of motion. However, often the initial conditions are known only with finite precision. Thus, we are interested in knowing how an initial error, or perturbation, on the initial conditions, say δ_0, will evolve in time.

Systems dominated by stationary equilibria or limit cycles are characterized by the fact that the initial error increases at most linearly with time, and thus predictability is assured for long times. In the case of a globally attracting fixed point, the system will always tend to the fixed point itself, and the initial error will decrease with time. On a limit cycle, on the other hand, there is a phase error that may grow at most linearly with time, leading to a slow loss of knowledge about the exact phase of the oscillation.

Now suppose that we consider a system with two stable equilibria and an unstable saddle point between them, such as the double-well oscillator pictured in figure 1.7 of lecture 1. In the vicinity of the unstable fixed point, a small perturbation on the initial conditions may force the system to tend toward one or the other fixed point, thus leading to unpredictability of the final state even for small initial perturbations. This happens, however, only for a very small, special region of phase space, the vicinity of the unstable point, and elsewhere the dependence on initial condition is much less extreme.

The key feature of the saddle point that leads to the system behaving in this way is the "division" of the phase space by the orbits that emerge or converge to the saddle point. These special trajectories are the "unstable" and "stable manifolds" of the saddle point (the set of all points that either diverge from, or converge to, that equilibrium). These particular orbits demark the directions of flow in phase space near the saddle. Importantly, at the locations where these manifold intersect, it takes only a slight change in initial condition to produce a very different evolution (namely, a perturbation for which the initial condition hops across one of the manifolds).

Systems undergoing deterministic chaotic dynamics, such as the Lorenz '63 model discussed above, are also characterized by "sensitive dependence on initial conditions." In these systems, the attractor itself contains infinitely many unstable elements (limit cycles). Like the saddle point considered above, each of the unstable cycles possesses intersecting stable and unstable manifolds that again partition the direction of flow in phase space. Thus, in the vicinity of each cycle, there must be a sensitive dependence on the initial condition. But the main difference between the two-well oscillator and the chaotic system is that the unstable cycles form the dense skeleton of the strange attractor. Hence there are intersecting manifolds densely populating the attractor and there is sensitivity to the initial state throughout the object.

For strange attractors, then, small initial perturbations can amplify exponentially fast and destroy the predictability of the system after a finite time. This behavior can be taken as a definition of deterministic chaos.

A quantitative way of defining sensitive dependence on initial conditions is based on the concept of Lyapunov exponents. If we consider a solution $\mathbf{X}$ of an n-dimensional dynamical system (such as $\dot{\mathbf{X}}=\mathbf{F}(\mathbf{X})$), the evolution of an infinitesimally small perturbation $\delta(t)$ can be considered linear to first order, and the governing equation becomes

$$\dot{\delta} = \frac{\partial \mathbf{F}}{\partial \mathbf{X}}\delta. \tag{2.17}$$

Each one of the n eigenvalues of the matrix $\frac{\partial \mathbf{F}}{\partial \mathbf{X}}$ gives an estimate of the growth rate of an infinitesimal initial perturbation aligned with the corresponding eigenvector of the matrix.

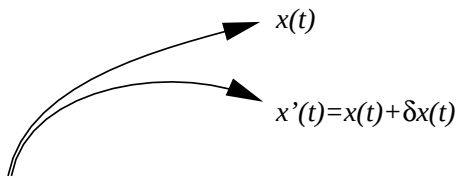

Figure 2.10: Divergence of nearby trajectories in phase space for a chaotic system.

The maximum Lyapunov exponent is then defined as

$$\lambda_{max} = \lim_{t\to\infty} \lim_{\delta_0\to\infty} \frac{1}{t} \ln \frac{\delta(t)}{\delta_0}$$

and it measures the fastest long-time growth rate of an infinitesimal error on the initial conditions.

Since a generic initial perturbation will have components along all the eigenvectors of the matrix $\partial\mathbf{F}/\partial\mathbf{X}$, the fastest growth will in general dominate and the infinitesimal error will approximately grow as $\delta(t) = \delta_0 e^{\lambda_{max} t}$ where $\delta_0 = \delta(t = 0)$, leading to rapid divergence of nearby trajectories (figure 2.10).

A dynamical system is generally considered to be chaotic if $\lambda_{max} > 0$. Note that the presence of the two limits in the previous definition is very important and cannot be neglected nor inverted: the perturbation must be infinitesimal in order to be considered linear, and the average on an infinite time is necessary as the Lyapunov exponent is a measure of the average error growth over the entire trajectory. Locally, the growth rate can be very different and may depend on the part of the attractor spanned during the evolution. For this reason, even if the maximum Lyapunov exponent is useful for the definition of a chaotic system, in practice it does not always give a good indication of how rapidly infinitesimal errors will grow at short times, as this may depend on the initial location on the attractor and on the initial direction of the error. Nor does it describe how finite errors grow.

2.3.2 Fractal Dimension

Due to the instabilities associated with sensitive dependence on initial conditions, most physically interesting strange attractors have a fractal nature. What is a fractal? A fractal is an object whose "fractal dimension", or better, "Hausdorff dimension" D_H is strictly larger than its topological dimension D_T. A fractal set is characterized by some form of scaling; that is, fragments of the sets, when suitably rescaled, display the same properties of the whole set, on every scale.

One way to introduce the fractal dimension of a set is the notion of box-counting. By splitting the phase space domain where the set is contained into square boxes of length ϵ one can count the number of boxes containing at least one point of the set, $N(\epsilon)$ (see figure 2.11). The box-counting dimension is then defined as:

$$D_0 = \lim_{\epsilon\to 0} \frac{\log N(\epsilon)}{\log(1/\epsilon)}. \tag{2.18}$$

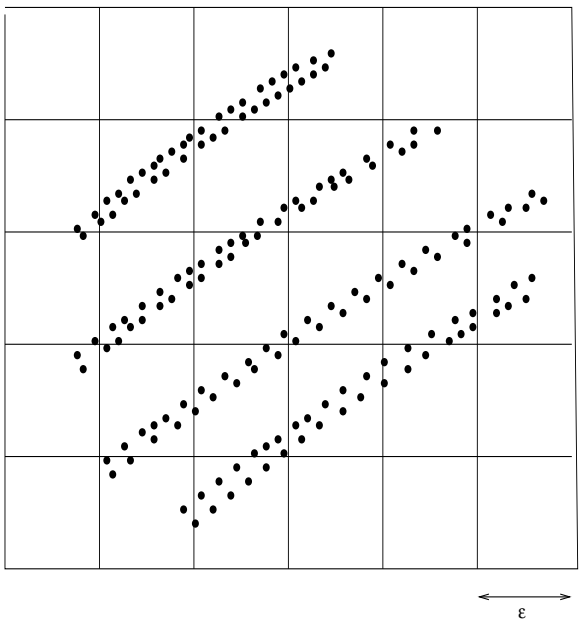

Figure 2.11: The notion of box-counting dimension. The object is divided into square boxes and the number of points is counted in each box. The lengths of the boxes are then successively reduce to generate data to compute D_0 via equation (2.18). Such a set of points could be generated by taking a Poincaré section of a strange attractor like that in figure 2.9.

This dimension coincides with the topological dimension for simple geometrical objects such as points, lines or planes but may be different for more complex objects.

An example of the latter is the Cantor set, which is obtained by taking a segment with unit length, cutting it in thirds, removing the middle third, and repeating the operation on the remaining two disconnected thirds, and so on forever (see figure 2.12). At the beginning, we have one segment with length $\epsilon_0 = 1$, $N(\epsilon_0) = 1$. At the first step, we have two segments with length $\epsilon_1 = 1/3$, $N(\epsilon_1) = 2$. At the second step, we have four segments with length $\epsilon_2 = 1/9$, $N(\epsilon_2) = 4$. At the n-th step, we have 2^n segments with length $\epsilon_n = 1/3^n$. It is easy to see that the fractal dimension of the Cantor set is

$$D_0 = \lim_{n\to\infty} \frac{\log 2^n}{\log 3^n} = \frac{\log 2}{\log 3}. \tag{2.19}$$

Since the topological dimension of the cantor set is $D_T = 0$, it is clear that this set is a fractal.

An extension of the box-counting dimension leads to the multifractal (or Renyi) dimensions D_q. One can define a partition function

$$B(\epsilon, q) = \sum_{i=1}^{N_{box}} [p_j(\epsilon)]^q, \tag{2.20}$$

where $p_j(\epsilon) = \frac{n_j(\epsilon)}{N}$ is the fraction of points found in the j-th box. For $q = 0$, B counts the number of non-empty boxes; thus one retrieves the definition of the box-counting dimension.

Figure 2.12: The Cantor Set

For arbitrary q, the asymptotic scaling of B is $B(\epsilon, q) \sim \epsilon^{(q-1)D_q}$ at small ϵ. One should note that D_q is a monotonically non-increasing function of q. The most frequently encountered multifractal dimension is D_2, since it is the simplest one which is sensitive to statistics and that can also be explicitly calculated in experiments.

2.3.3 Conceptual implications of deterministic chaos

The discovery that even very simple mathematical models can lead to unpredictable behavior has, of course, several conceptual implications. Probably, the two most important ones are:

- The presence of unpredictability in deterministic systems does not require random external influences or quantum fluctuations, and it is an intrinsic property of many dynamical systems;
- An observed irregular and unpredictable behavior does not necessarily imply the presence neither of a large number of degrees of freedom in the system dynamics, nor of randomness, as three nonlinearly coupled variables can generate it.

This "hope for simplicity in unpredictability" has triggered many attemps to discover whether an observed "random" dynamics was really due to turbulent-like behavior or to the presence of a low-dimensional (in phase space) strange attractor. Some of these attempts are described in the next Lecture.

Lecture 3

Time Series Analysis and Phase Space Reconstruction

Ever since the discovery of deterministic chaos and strange attractors, researchers have developed methods of nonlinear time series analysis based on dynamical system theory, with the aim of detecting the possible presence of low-dimensional chaos in measured time series. This lecture is devoted to introducing some of the techniques used to characterize chaos from measured data. Thorough introductions to these subjects are given by Ott *et al* (1994) and Kantz and Schreiber (1997).

3.1 Phase Space Reconstruction

To properly describe the dynamics of a system, one needs to have access to its phase space. However, experimental measurements rarely provide direct information on the whole ensemble of phase-space variables of the system. The typical outcome of an experiment, or of observation, is a time series of a scalar variable, $h(t)$, $t \equiv t_n = n\Delta t$, $1 \leq n \leq N$, whose relationship to the phase-space variables is not known a priori. In such a situation, the first thing to do is to try to reconstruct an approximation to the phase space of the system. One interesting approach to this problem has been proposed, in the early 80's, by Takens (1981) and Packard *et al.* (1981). This is now known as the procedure of time embedding, and it is briefly recalled below.

3.1.1 Time embedding

First, we suppose that our measured time series is a smooth function of *all* the phase space variables, $h(t) = f(\mathbf{X}(t))$. We also note that, in principle, the same information is provided by the set of M phase-space variables, $\mathbf{X} = (X_1, X_2, ..., X_M)$ and by the derivatives up to order $M-1$ of any of them; that is, by $(X_j, dX_j/dt, d^2X_j/dt^2, ..., d^{M-1}X_j/dt^{M-1})$, given the generic situation that X_j interacts with all the other variables in phase space. The extension to the experimental case is then obtained by realizing that a similar information is provided

by the signal $h(t)$ and its time derivatives; that is, by $(h, dh/dt, d^2h/dt^2, ...)$. Since, however, we deal with a signal measured at discrete time intervals, the first derivative is really $(h(t) - h(t-\tau))/\tau$. Takens and Packard *et al.* then suggested to use the time-delayed variables $(h(t), h(t-\tau), h(t-2\tau), ...)$ as an approximate representation of the phase space of the system. This approach is called time embedding, and the space spanned by h and its time-delayed values is called the embedding space. The dimensionality of this space is called the embedding dimension. Schematically, this procedure can be depicted as follows:

$$(\mathbf{X} \equiv (X_1, X_2, ..., X_M)) \tag{3.1}$$

$$\Downarrow$$

$$(X_j, \dot{X}_j, \ddot{X}_j, ...) \tag{3.2}$$

$$\Downarrow$$

$$(h(t), \dot{h}(t), \ddot{h}(t), ...) \tag{3.3}$$

$$\Downarrow \qquad \dot{h} = \tfrac{h(t)-h(t-\tau)}{\tau}$$

$$\mathbf{Z}_M = (h(t), h(t-\tau), h(t-2\tau), ..., h(t-(M-1)\tau)). \tag{3.4}$$

For time series of infinite length and finite variance, Takens (1981) has demonstrated that there is a diffeomorphic equivalence between $\mathbf{X}$ and $\mathbf{Z}_M$ (that is, they have a smooth functional relationship). In this case, the specific value of the time delay is not important. For time series with finite length, the above approach is necessarily heuristic, and the choice of the value of the time delay τ becomes important.

In general, the procedure followed in the analysis of a time series is based on the definition of a hierarchy of embedding spaces of increasing dimension. In each of these spaces, some relevant dynamical measures are computed (such as the dimension of the supposedly existing attractor, the maximum Lyapunov exponent, and so on), until a saturation in the value is reached. That is, saturation is achieved when the value of the chosen dynamical quantity does not change for a further increase of the embedding dimension, M, beyond a saturation value, M_s. In this case, the value of M_s is thought to provide information on the dimensionality of the "true" phase space of the system, and the value of the dynamical quantity that we computed (provided we have selected a quantity which is invariant under phase-space coordinate changes) approximates its true value. While this expectation is justified for long time series generated by low-dimensional dynamical systems, the embedding approach has often been applied to short time series of unknown origin. In this case, troubles can easily be encountered, and false results are often obtained, as discussed in the next section.

3.1.2 Choice of the time delay

An important step in the procedure of time embedding is the choice of the time delay τ. For a time series of finite length, measured with a finite sampling time, too small a value of the time

delay results in a crowding of points along the diagonal of the reconstructed space, and the dynamics cannot be properly unfolded. On the other hand, too large a value of τ leads to a lack of correlation between the different variables in the reconstructed space, with a resulting loss of information. Thus, one needs to choose τ in a range such that the dynamics is unfolded but the values $h(t), h(t-\tau), ...$ are not fully decorrelated. Traditional choices of τ are:

- $T_0/4$ if there exits a dominant period T_0 in the signal.
- The first zero of the autocorrelation function,

$$R(s) = \lim_{T\to\infty} \frac{1}{T} \int_0^T h(t)h(t+s)dt, \tag{3.5}$$

  where $h(t)$ denotes the signal under study.

- The first minimum of the mutual information function,

$$I(\tau) = \sum_{h_1,h_2} p_{jo}(h_1, h_2; \tau) \log_2 \left[\frac{p_{jo}(h_1, h_2; \tau)}{p(h_1)p(h_2)} \right] \tag{3.6}$$

  (Fraser & Swinney 1986), where $p(h)$ is the (empirical) probability of observing the value h and $p_{jo}(h_1, h_2; \tau)$ is the joint probability of observing the value h_1 at some time and the value h_2 a time delay τ afterwards.

In general, it is important to verify that the results of the analysis do not depend too sensitively on the exact choice of τ; that is, they should hold over a sufficiently large range of values of the time delay, centred on the "optimal" value defined by one of the methods mentioned above.

3.1.3 Correlation Dimension

Once one has reconstructed a (pseudo) phase space with dimensionality M, one way to quantify the dynamics underlying a given time series is to measure the dimension of the data set in the reconstructed space. Grassberger & Procaccia (1983) developed a simple algorithm to get an estimate of the attractor dimension. First, we compute the correlation integral,

$$C_M(r) = \frac{2}{N'(N'-1)} \sum_{i=1}^{N'} \sum_{j=i+1}^{N'} \Theta(r - |\mathbf{Z}_i - \mathbf{Z}_j|), \tag{3.7}$$

where Θ is the Heaviside step function and N' is the number of points in the reconstructed (vector) time series $\mathbf{Z}$, $N' = N - (M-1)m$ where $m = \tau/\Delta t$ and Δt is the sampling interval.

We are then interested in the behavior of $C_M(r)$ as r tends to zero. If the system dynamics is governed by a low-dimensional attractor, then the correlation integral has a small-scale power-law behavior, $C_M(r) \propto r^{\nu(M)}$. Below saturation, the value found for the correlation exponent $\nu(M)$ generally depends on M, the embedding dimension. As M is increased, however, for

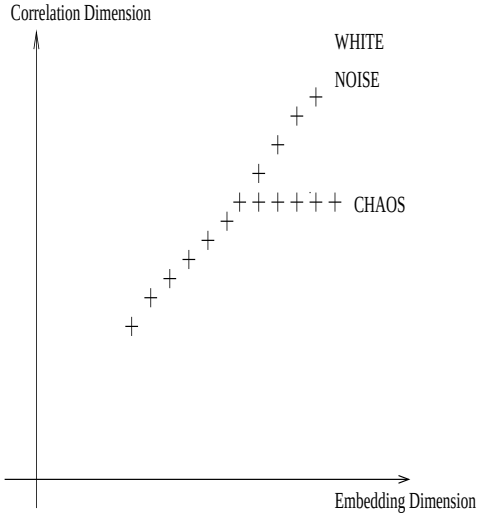

Figure 3.1: Different behavior of the correlation dimension for chaos and white noise

systems dominated by an attractor with finite (and possibly small) dimensionality, the value of $\nu(M)$ approaches a finite limit D_2, called the correlation dimension, which provides an estimate of the fractal dimension of the attractor. Fixed points and limit cycles are characterized by dimension of respectively zero and one, while quasi-periodic motion has a dimension equal to the number of independent (incommensurate) frequencies. Strange attractors, associated with chaotic motion, are usually characterized by a non-integer dimension.

The value of D_2 gives important information on the number of excited degrees of freedom in the system. In particular, phase-space dynamics characterized by a small value of the correlation dimension may be described by a system of a few (usually, at most $2D_2+1$) coupled ordinary differential equations. Note, however, that a (reliable) detection of a finite and small value of D_2 only indicates that a description in terms of a low-dimensional deterministic model should be possible. No information is provided on how the appropriate collective degrees of freedom can be identified.

Conversely, white noise is associated with a non-convergent value of the correlation dimension (see figure 3.1). Thus, if in the analysis of a measured time series no convergence in $\nu(M)$ is observed for increasing M, it is generally assumed that the number of excited degrees of freedom in the system is large: in this case, a stochastic model might be more appropriate.

Two remarks are in order here. Curves plotted on log-log coordinates have often the tendency to look like power laws, even though the power-law behavior is that of the tangent to the curve rather than of the curve itself. For this reason, it is usually better to plot the local logarithmic derivative of the correlation integral, $\nu_M(r) = d\log C_M(r)/d\log r$, versus $\log r$, to verify whether there is a sufficently extended scaling interval where $\nu_M(r)$ is constant, $\nu_M(r) = \nu(M)$. A practical way of obtaining $\nu_M(r)$ is, for example, by taking the local least-square fit of $\log C_M(r)$ versus $\log r$ over three consecutive points.

The second remark concerns the statistical requirements for a reliable estimate of the

correlation dimension. This issue has been discussed by several papers (Smith 1988, Eckmann & Ruelle 1992), with conflicting estimates on the minimal number of points that is required to reliably detect a dimension D_2. Here, we simply say that, on average, $N_{min} \approx 10^{D_2}$ points are required in order to safely detect a correlation dimension D_2. When a convergent correlation dimension D_2 is detected with less than N_{min} points, there is the danger that the convergence of D_2 has been forced by lack of statistics rather than by low-dimensional dynamics.

3.2 Finite dimension from stochastic processes

If a measured time series is produced by low-dimensional (chaotic) dynamics, saturation of the correlation dimension for increasing embedding dimension is observed. On the other hand, in the analysis of measured data one does not know whether the system is low-dimensional. Indeed, this is exactly one of the questions the analysis should answer, and it is not possible to assume the presence of low-dimensional chaos a priori. However, in the early days of phase-space reconstruction and analysis (i.e., in the early 80's), the detection of a finite and small value of the correlation dimension was considered a safe indication of the existence of low-dimensional chaos. In this way, several works claimed the presence of strange attractors in the most diverse systems.

Later on, some studies (Osborne & Provenzale 1989; Provenzale *et al* 1992) revealed that the sole detection of a finite value of the correlation dimension from a measured time series is not enough to infer the presence of low-dimensional chaos, since there are stochastic processes that provide a spurious convergence of the correlation exponent under time-embedding.

These stochastic processes are, in general, characterized by power-law power spectra and self-similar behavior over an extended range of scales. One example is provided by the Gaussian stochastic process defined by

$$s(t_i) = \sum_{j=1}^{N/2} A_j cos(\omega_j t_i + \phi_j), \tag{3.8}$$

where $A_j^2 \propto \omega_j^{-\alpha}$ and ϕ_j are random uniformly distributed phases. In this case, the correlation dimension is given by $\nu = \nu(\alpha) = \frac{2}{\alpha - 1}$ for $1 < \alpha \leq 3$ (see figure 3.2).

A second popular example is the linear Ornstein-Uhlenbeck (OU) process:

$$ds = -\gamma\, s(t)dt + \sigma\gamma^{1/2}dW, \tag{3.9}$$

where $\gamma = 1/T_d$ is the inverse of the signal decorrelation time T_d, σ^2 is the variance of the signal and dW is a gaussian-distributed random increment with $\langle dW \rangle = 0$ and $\langle dW^2 \rangle = 2\,dt$ (a Wiener process). Equation (3.9) generates a scalar time series, $s(t)$, that is gaussian distributed and becomes stationary at large times. The power spectrum of $s(t)$ is $P(\omega) \propto [1 + (\omega/\gamma)^2]^{-1}$, which is of power-law form, $P(\omega) \approx \omega^{-2}$ at high and intermediate frequencies, and it becomes constant at low frequency.

Another example is provided by a nonlinear stochastic process, that may be written as

$$dS = (1/2 - S(t))dt + (2S(t))^{1/2}dW. \tag{3.10}$$

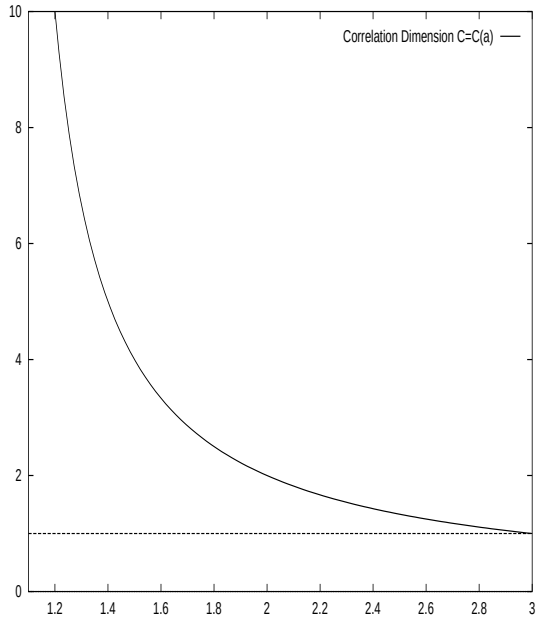

Figure 3.2: Correlation dimension, $\nu(\alpha)$, of the Gaussian stochastic process (3.8).

The time series generated by this process has a power spectrum that is very similar to that generated by the OU process (see figure 3.3), but it is characterized by well-defined intermittency properties and correlated Fourier phases (ref).

The apparent value of the correlation dimension, as computed from time-embedding of $s(t)$ or $S(t)$, depends in this third example on the length T of the time series. For very long series, $T \to \infty$, the correlation exponent $\nu(M)$ grows without bound with M, due to the stationarity of the signals. For time series with intermediate length, however, full stationarity has not yet been reached, and the value of the correlation exponent converges to a finite value ν_c for growing M. This value is related to the approximate self-similarity of the signals, and has nothing to do with the true phase-space dimensionality of the system (which is unbounded since the process is stochastic). This behavior is due to a failure of the time-embedding procedure, which cannot reconstruct the true phase space of the system due to the non-stationarity of the time series. Such a behavior has been observed in several instances, since for many measured time series the record is not long enough to ensure full stationarity. Note also that the time series $S(t)$ generated by the nonlinear process provides a positive answer to nonlinearity tests, showing that nonlinearity and a finite estimate of the correlation dimension from a measured signal (with finite length) is not enough to infer the presence of low-dimensional chaos.

In past years, other stochastic processes have also been shown to induce a spurious convergence of the correlation exponent. This demonstrates the impossibility to distinguish practically between a low order, deterministically chaotic system and a stochastic one, using just the above developed tools. For this reason, various other methods have been developed that allow us to recognize some of these "false positive" results. Some of these methods are described below.

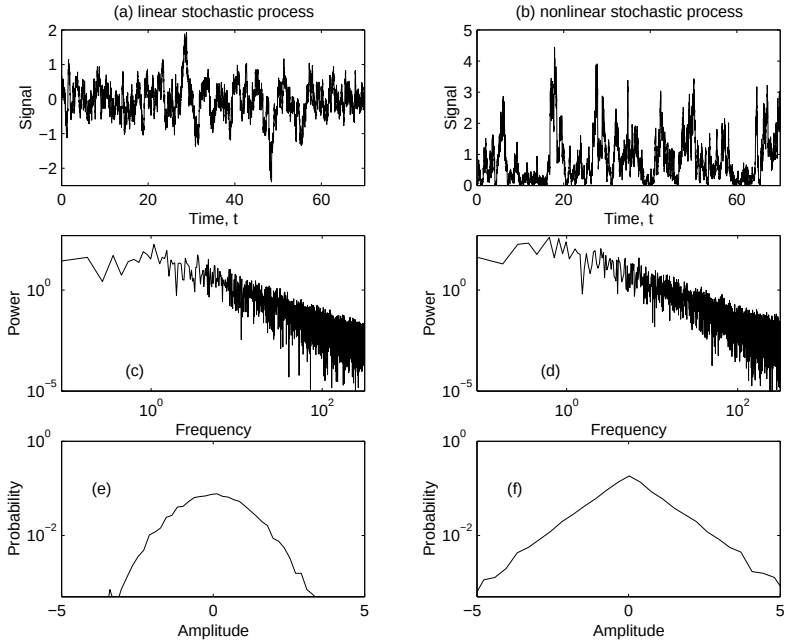

Figure 3.3: Time series for the stochastic processes (3.9) and (3.10), shown in panels (a) and (b) respectively. Panels (c) and (d) show the corresponding Fourier power spectra, and (e) and (f) show histograms displaying the approximate probability distributions of the temporal derivative of the signal.

3.3 Distinguishing chaos from noise

The reason why one cannot detect differences between chaos and noise in the previous cases is because of the intrinsically fractal nature of the noise. The fractal curves encountered above have a fractal dimension completely defined by the spectral slope and thus exhibit saturation. On the other hand, the reconstructed space is not the real phase space of the system, due, for example, to non-stationarity of the signal, or to an insufficient length of the time series. Therefore, by computing the value of the correlation dimension one cannot distinguish between differentiable strange attractors and non-differentiable fractal stochastic curves if they have the same dimension.

In order to solve this problem several methods have been proposed. Most of these methods are based on the concept of "surrogate data." That is, we generate a synthetic time series that has all but one of the properties of the measured signal, in order to verify whether the value of the correlation dimension, or the Lyapunov exponents, depends on the modified property.

3.3.1 Phase randomization

One of the most common tests is that based on the randomization of Fourier phases. This test is the simplest and less refined one of the many available surrogate data techniques; however, it has proven to be quite useful on many occasions. The phase-randomization test allows us to verify whether an observed convergence of the correlation exponent is due to the presence of a self-similar stochastic process. In the case of self-similar stochastic processes, the convergence of the correlation exponent is related to the power-law form of the power spectrum; that is, to the properties of the second-order moment. By contrast, the finite value of the correlation dimension for a low-order deterministic system is due to close returns in phase space; these are in turn related to the distribution of the Fourier phases of the signal.

Based on this observation, it has been suggested (Theiler *et al.* 1992; Osborne *et al.* 1986) to test the origin of an observed convergence in the correlation exponent by generating a synthetic time series having the same power spectrum as the measured data, but random Fourier phases. This surrogate signal has a gaussian distribution with the same second-order moment as the time series under study. If the correlation exponent converges also for this surrogate signal, then the origin of the convergence in the original time series cannot be related to its phase-space structure, and the hypotesis of low-dimensional chaos has to be rejected. The test does not, however, unambiguously identify low-dimensional chaos: if the surrogate signal does not generate a convergent value of the correlation exponent, one cannot conclude that the system is governed by low-dimensional chaos; in this case, other surrogate data tests have to be applied before any safe conclusion might be reached.

3.3.2 Method of close returns

This method uses one of the main properties of strange attractors. It is well known that the phase-space trajectories of a low-dimensional dynamical system return close to their initial positions from time to time, whereas this is not the case for stochastic systems. Consequently, one can plot the separation in space against the separation in time for these two different types

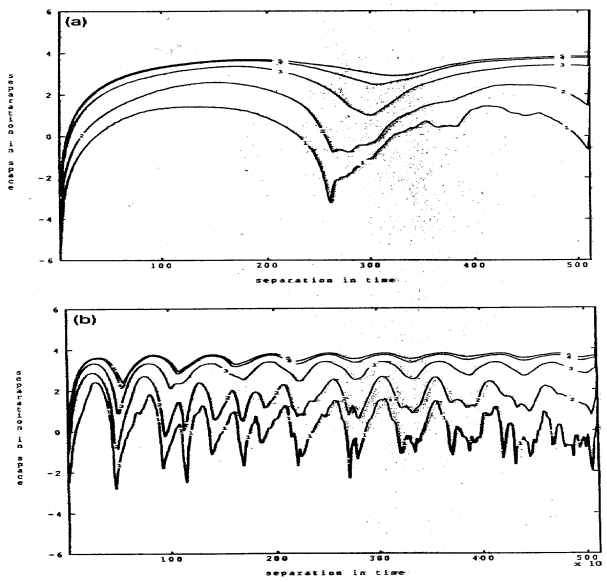

Figure 3.4: Separation in Space .vs. Separation in Time for the Lorenz attractor. Adapted from Provenzale *et al.* 1992.

of systems. Then, the existence of these close returns will yield a non-monotonic graph and a further piece of evidence of the presence of a strange attractor.

Plots of separation in space against separation in time are displayed in figures 3.4 and 3.5. The close returns in the Lorenz model clearly distinguish it from the nonlinear stochastic process.

In general, surrogate data tests have been applied to many apparent detections of low-dimensional chaos from measured data, and most of the time series measured outside controlled laboratory conditions have not survived a careful scrutiny of the results. For example, the light curve of the optical, violently variable quasar 3C 345 is seemingly characterized by a low value of the correlation dimension when analyzed improperly (*e.g.* Provenzale *et al.* 1994). This indicates that the simple view of a low-dimensional attractor in most physical systems is unsatisfactory. Instead, we must search for richer dynamical possibilities, although we do not necessarily need to abandon approaches based on "simple" models. Some of these approaches - chaos outside the ivory tower - are discussed the next lectures.

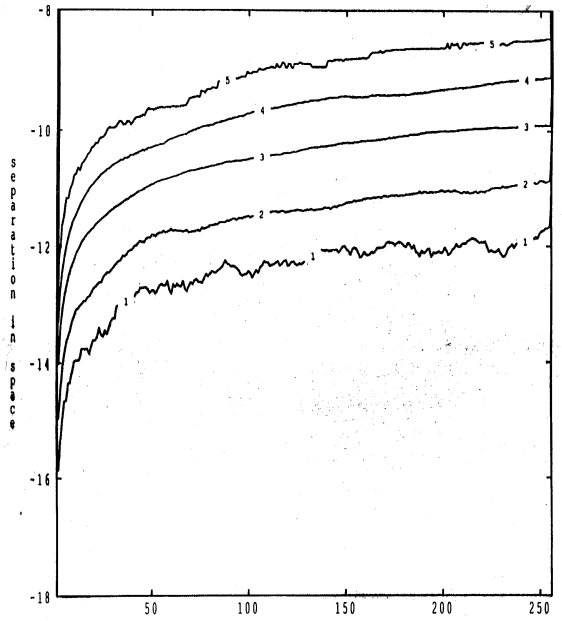

Figure 3.5: Separation in Space .vs. Separation in Time for the nonlinear stochastic process (3.10). Adapted from Provenzale *et al.* 1992.

Lecture 4

Externally Driven Chaos

4.1 Out of the ivory tower

In the first two lectures, we have seen how three-dimensional dynamical systems (such as the Lorenz 63 model) are capable of generating multiple equilibria, periodic and quasiperiodic oscillations and chaotic trajectories without any external forcing mechanism.

Do these models have anything to do with reality? This is indeed an eternal question in dynamical systems theory, and for the simplified approaches described in these notes. At first, simplified models were introduced mainly as metaphors, without claiming a direct link with specific phenomena. Later on, researchers became excited by their simplicity, and tried to literally interpret natural events in terms of low-order, autonomous dynamical systems: Like Frankenstein's monster, modelling by low-order dynamical systems took on a life of its own. More recently, many methods of time series analysis have become available, some of which are reviewed in Lecture 3. The main outcome of the application of such analyses, however, has been a realization that natural phenomena (outside controlled laboratory conditions) are seldomly described by low-order, autonomous dynamical systems. So seldomly in fact, that should one find a genuine low-order, dissipative chaotic system in nature, the discovery should be suitably celebrated (for example, by a bottle of properly aged Barolo).

Given this inability of low-order models to explain natural phenomena, what should we do instead? We have first to remember that our little dynamical system is really just a metaphor. When motivated by a specific problem, we can write a simplified model that provides a mathematical framework to formulate relevant questions. Typically, the model is only appropriate to address the issues for which it has been fabricated. It is a serious mistake to push it beyond its limits, or to use it for completely different questions.

But, once we appreciate the limits, we may press further afield and we need not be so conservative; we must only be ready to modify the metaphors when appropriate. For example, most natural systems are driven by external forcings, are coupled with each other, and have different coexisting time scales. In dealing with these new physical ingredients, it is neither expedient nor feasible to resort to sophisticated models. Instead, it is more sensible to explore these processes by exploiting appropriate simple models. Thus, in the coming three lectures,

we lose our virginal low dimensionality, leave the ivory tower (which lies in ruin around us anyway), and build metaphors for forced and coupled systems. Perhaps, in doing so, we move no closer to reality, but we can nevertheless discover and explore new possibilities and intriguing mechanisms.

4.2 A metaphor for large-scale atmospheric motions

In the following, we introduce another three-dimensional dynamical system, namely the model that Lorenz (1984) proposed as a simplified description of midlatitude atmospheric dynamics. After a brief discussion of the model behavior, we explore what happens when the model is subject to external periodic forcing.

4.2.1 Chaos in the midlatitudes

In 1735 Hadley proposed that the large scale circulation of the atmosphere consisted of air rising at the equator, travelling aloft away from the equator before sinking at the poles (Hadley, 1735). However, this picture neglects the effects of the Coriolis force which leads to geostrophic balance at mid-latitudes. In fact, due to rotation, such a cell (now called the Hadley circulation) would produce easterly winds at midlatitudes, the opposite of what is observed. Thomson (1857) and Ferrel (1859) modified this picture and introduced a second circulation cell which is now called the Ferrel cell (see Figure 4.1). With this modification, westerlies at midlatitudes and easterlies (trade winds) at low latitudes are recovered.

The circulation described by this simple picture is zonally symmetric. However, it is not actually observed. Rather, strong transient perturbations dominate the atmospheric circulation, especially at midlatitudes. These perturbations take the form of strong cyclones (storms) that induce irregularities which completely dominate any ordered zonal pattern such as the Ferrel cell.

In the past, two possible reasons for the lack of zonal symmetry have been proposed. One possibility is that a zonally symmetric circulation is not a solution of the equations of motion, and the basic state is fundamentally asymmetrical. Alternatively, a second possibility is that the Ferrel cell is a solution to the equations, but it is unstable to asymmetrical perturbations; these growing perturbations spawn the mid-latitudes cyclones.

To address this specific issue, Lorenz proposed a simple model for large scale circulation in one hemisphere (Lorenz, 1984). The model equations are

$$\frac{dX}{dt} = -Y^2 - Z^2 - aX + aF \tag{4.1}$$

$$\frac{dY}{dt} = XY - bXZ - Y + G \tag{4.2}$$

$$\frac{dZ}{dt} = bXY + XZ - Z. \tag{4.3}$$

In these equations X represents the intensity of the symmetric westerly wind, which (in the usual thermal wind balance) is proportional to the average meridional temperature gradient

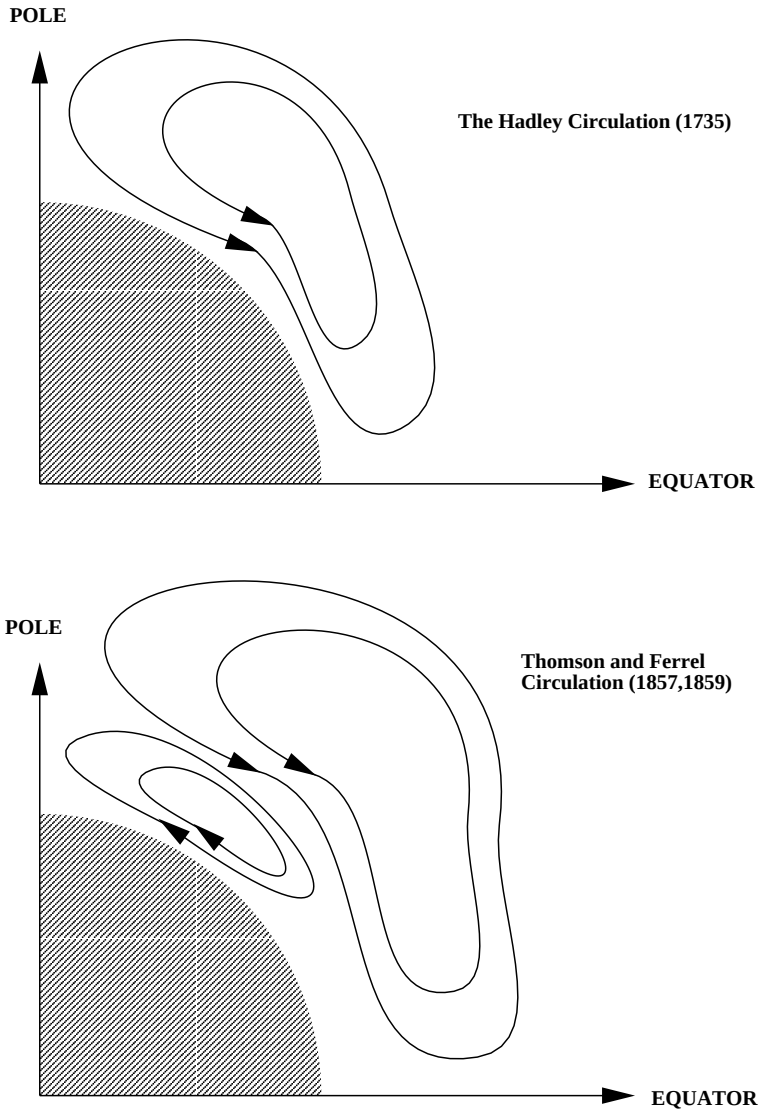

Figure 4.1: A schematic representation of the atmospheric circulations proposed by Hadley and by Thomson and Ferrel.

between Equator and Pole. The variables Y and Z are Fourier amplitudes characterixing a chain of large-scale eddies. The eddies transport heat poleward at a rate proportional to Y^2 and Z^2, which reduces the pole-equator temperature diference and, thence, the wind. The term aF represents the symmetric forcing, due to the Equator-Pole difference in solar heating, and G is a longitunally dependent (nonsymmetric) forcing term that models the temperature differences between continents and oceans. If we ignore the nonlinear coupling terms, then the equations predict that X relaxes to F and Y relaxes to G.

The solutions to the system of equations are bounded:

$$X^2 + Y^2 + Z^2 < E_{max} \qquad t \to \infty, \tag{4.4}$$

for some constant E_{max}. Furthermore, the phase space divergence can be calculated:

$$\frac{\partial \dot{X}}{\partial X} + \frac{\partial \dot{Y}}{\partial Y} + \frac{\partial \dot{Z}}{\partial Z} = -a - 2 + 2X. \tag{4.5}$$

Thus it can be seen that the phase space volume contracts only if $X < 1 + a/2$. Since the phase space volume does not contract everywhere in phase space, attractors may have finite volume.

The fixed points of the system are given by

$$Y = \frac{(1-X)G}{1 - 2X + (1+b^2)X^2}, \tag{4.6}$$

$$Z = \frac{bXG}{1 - 2X + (1+b^2)X^2} \tag{4.7}$$

and

$$a(F - X)(1 - 2X + (1+b^2)X^2) - G^2 = 0. \tag{4.8}$$

From equations (4.6)-(4.8) it can be seen that if $G = 0$ then the fixed points are $X = F$, $Y = Z = 0$. This solution corresponds to the symmetric Hadley circulation. In this case, if $F < 1$ the solution is stable, whereas if $F > 1$ the solution is unstable and eddies are produced by the instability of the symmetric state. For cases when $G \neq 0$ there can be multiple equilibria as shown in Figure 4.2. For small values of G, there is only one solution which is similar to the Hadley circulation (point A). For intermediate values of G there are three equilibria. One of these is similar to the Hadley circulation (point B), the second is unstable (point C) and the third corresponds to an asymmetric, non-Hadley circulation (point D). This final state could be described as "blocked"; that is, a strongly nonzonal circulation whose structure is locked into place as a result of the nonsymmetrical thermal forcing between land and sea (entering through G). This asymmetric circulation is reminiscent of blocking by topographic forcing (Charney & DeVore 1979). For large values of G, only this latter equilibrium exists (point E).

Thus, even such a simple model shows that midlatitude disturbances can be produced by either instability of a symmetric, Hadley-like circulation ($G = 0$,$F > 1$) or as fundamental, non-Hadley states (*e.g.*, case E).

An interesting feature of this model is that it produces multiple steady states (as many other models before it). This multiplicity of attractors, sometimes called *intransitivity*, extends

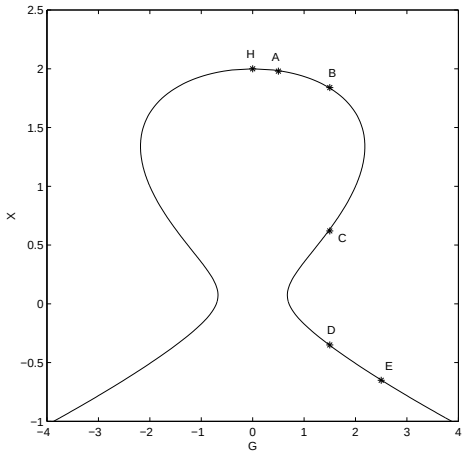

Figure 4.2: The equilibria curve for the Lorenz 84 model plotted in the $G - X$ plane, where X is the strength of the zonal flow and G is the strength of the zonally asymmetric forcing.

also to more complicated solutions such as limit cycles and chaotic attractors: For the case $G = 0$ and $F > 1$, equations 4.1-4.3 have a stable, attracting periodic solution:

$$X = 1, \tag{4.9}$$

$$Y(t) = \sqrt{a(F-1)}\cos(bt - \phi_0), \tag{4.10}$$

$$Z(t) = \sqrt{a(F-1)}\sin(bt - \phi_0). \tag{4.11}$$

This solution undergoes period doubling as G is increased. For $G = 0.8$, there are two coexisting attractors; both are limit cycles (see Figure 4.3). Therefore, for these parameters values, the model has two stable "climate" states. At larger values of G, the two attractors merge and the model behaves chaotically, as shown in Figure 4.4.

4.2.2 Periodic driving of an intransitive system

The model discussed above does not contain any external forcing, and still it is capable of producing an internal (periodic or chaotic) variability. On the other hand, the real atmosphere has significant external forcings at diurnal and annual periodicities, and it is therefore of interest to explore how an external, periodic forcing modifies the internal variability of the model.

For linear systems, periodic forcing introduces a periodic response except at resonance when the frequency of the driver coincides with an internal frequency of the driven system. For nonlinear systems, even a simple periodic driving may generate a vart range of new and interesting effects.

A particularly interesting case is when one of the control parameters of the system (e.g., F or G in the Lorenz 84 model) is paramterically driven. Notably, if the parameters are driven

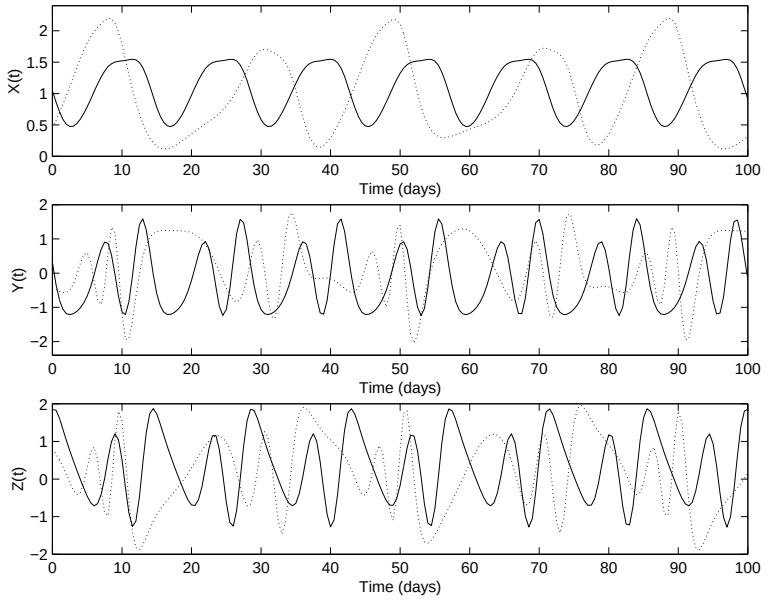

Figure 4.3: Time series of X, Y and Z for the two stable periodic solutions that exist when $G = 0.8$. The solution shown by solid lines is the "weak" attractor, and that by dotted lines is the "strong" one. Note that one time unit of the model corresponds to 5 days, and that $a = 0.25$, $b = 4$ and $F = 8$.

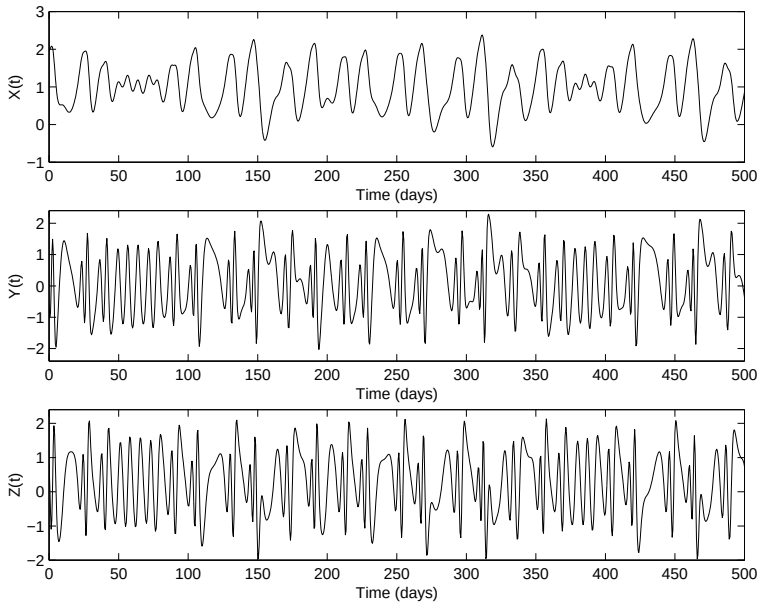

Figure 4.4: Time series of the aperiodic behavior of X, Y and Z when $G = 1$, $a = 0.25$, $b = 4$ and $F = 8$.

through a point of bifurcation of the the unforced system, then "switching" can occur as the system turns "on" and "off" (this idea recurs in the next lecture). For example, take the Lorenz 84 model in the vicinity of a transition from periodicity to chaos, and vary F periodically such that its extreme values correspond to periodic or chaotic behavior in the undriven system. In this case, the system undergoes transitions between these two regimes, switching between regular cycling and chaos. Sometimes, the timescale for switching can be lengthy, and this introduces a simple form of low-frequency (interannual) variability into the model. However, this behavior strictly depends on the fact that the system is close to a bifurcation.

Another interesting case, with richer dynamics, is obtained when the system is intransitive, and has at least two attractors. In the simple case of multiple steady states, periodic driving can precipitate regular transitions of the system from one equilibrium to the other. Clearly, the driver must have a sufficient amplitude as to force the system to cross the potential barrier between the two equilibria (equivalently, for a simple oscillator, to modify the form of a double potential well and allow the system to roll from one equilibrium to the other).

Even more interesting is when the undriven system has time-dependent multiple states, such as periodic oscillations or chaotic attractors. This case was considered by Lorenz (1990), who studied a situation where the system is forced to move through a bifurcation between periodicity and chaos, with the addition feature that the periodic dynamics is intransitive (as in figure 4.3).

Lorenz's motivaton was climatological, and the periodic perturbaton modelled the seasonal cycle. More specifically, Lorenz used the model described above, but with F parameterically

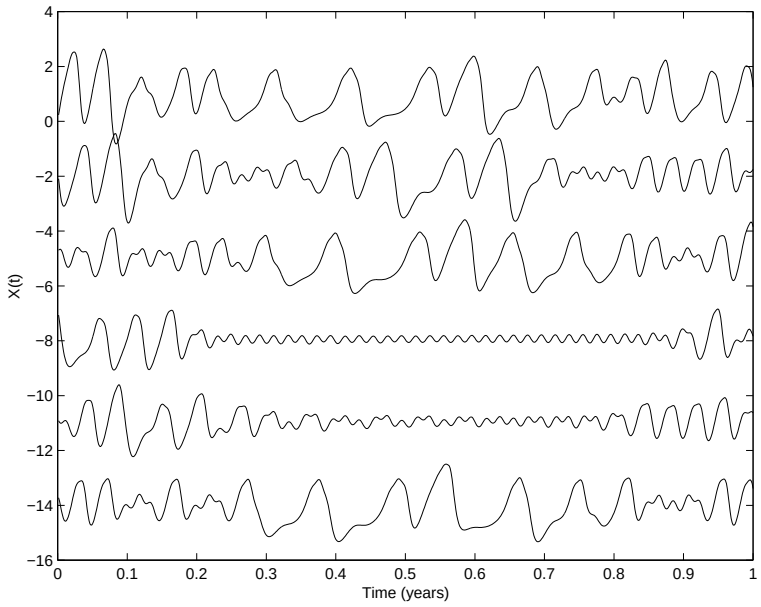

Figure 4.5: The variations in X for the case when $G = 1$, $A = 0.25$, $b = 4$, and $F = 7+2\cos(2\pi t/\tau)$, with τ corresponding to 12 months. The time series are divided into successive yearly segments and offset downwards.

forced to represent the variation in the Equator-Pole temperature difference from summer to winter. Lorenz identified the chaotic, transitive regime found at larger values of F (figure 4.4) with winter and the periodic, intransitive regimes at lower F with summer (figure 4.3). The summer regime has a so-called "weak" attractor which has a small basin of attraction and a small oscillation amplitude (the solid lines in figure 4.3), and a "strong" attractor with a larger basin and larger oscillations (the dotted lines in figure 4.3). An example with $A = 0.25$, $b = 4.0$, $G = 1.0$ and $F = 7.0 + 2.0\cos(2\pi t/T)$, where T corresponds to 12 months is shown in Figure 4.6.

As suggested above, this system changes from a chaotic behavior in winter to a periodic dynamics during summer. However, during summer the system can approach either the weak or the strong periodic attractor, depending on the conditions encountered at the end of the winter. During winter the system loses almost all memory of its state in the previous summer, and at the end of the winter it lies at a point on the chaotic attractor which is practically independent of the conditions at the beginning of the winter. Thus, the probability of approaching the weak or the strong attractor in the following summer depends chiefly on how the winter attractor is distributed within the basins of the two summer limit cycles. This produces irregular sequences of weak and strong summers, which generate significant low-frequency variability.

The interesting dynamics generated by this model is due to both the passage of the system through a bifurcation, and, even more importantly, to the intransitivity of the summer dynamics. We are thus faced with a dynamically "bimodal" system where the choice between

the two possible states is dictated by a chaotic process. Presumably, we could have obtained similar effects by considering a purely intransitive dynamics where, at periodic intervals, an external random noise resets the system and forces it to choose again one of the two possible states. The interest of the Lorenz 84 model, however, is that this process is obtained in a very simple and self-consistent, deterministic way.

4.3 A stochastically forced model of the thermohaline circulation

We next consider another type of external forcing, namely, random white noise acting on a low-order dynamical system. This case is quite important as most systems are subject to the influence of unresolved "turbulent" dynamics that can alter the simple behavior of the unforced model. In particular, we consider the effects of random noise acting as a driver in the equations of motion. We have encountered a simple example of this in Lecture 3, when dealing with the (linear and nonlinear) Langevin equation. In that case, the deterministic dynamics was extremely simple. By contrast, here we consider situations where the deterministic part has an interesting behavior even without external noise. Note, also, that the case of dynamical noise is more relevant and much more complicated than pure additive noise superposed onto a signal produced by a low-order system, as happens, for example, if there is a random error in taking measurements.

As a specific example, we consider the noise-driven dynamics of a simple box model of the thermohaline circulation of the ocean, following Cessi (1994). Again, most of the interesting effects are due to the intransitive nature of the unforced model.

The oceanic thermohaline circulation (THC; see Whitehead 1995, for a review) is due to the joint effect of temperature and salinity on water density. Consider, in particular, a simple model of an ocean that extends from the Tropics to high latitudes. If, over some extensive region of ocean, the water is denser at the surface than at the bottom, then fluid sinks and drives a convection current through the entire ocean. This circulation can maintain itself if there is a suitable influx or outflux of the two components contributing to the local density (heat and salt). Such fluxes are provided by differential solar heating, evapouration and precipitation.

The density ρ of sea water may be approximately expressed as

$$\rho - \rho_0 = \alpha_s(S - S_0) - \alpha_T(T - T_0), \tag{4.12}$$

where T is temperature, S is salinity, and ρ_0 is a reference density with salinity S_0 and temperature T_0. Thus, density increases on lowering the temperature, or in raising the salinity.

At high latitudes, surface cooling may be very effective. In the Atlantic, this happens in the Labrador Sea, for example. In the Mediteranean, cooling takes place in the Gulf of Lyon south of Marseille and in the northern Adriatic Sea. Thus, cold water sinks at these high latitudes, and a "direct" circulation is established with warm surface water flowing from the tropics to high latitudes, and cold bottom water flowing toward the Equator. This is the

circulation pattern observed today in the Atlantic and the Pacific, with the Gulf Stream being part of the northward "conveyor belt" transporting heat at high latitudes.

On the other hand, intense evaporation at low latitudes generates salty water at the surface in the tropics, and precipitation and the melting of ice produces fresh surface water at higher latitude. If the evaporation or flux of fresh water is large enough, then the contribution of salinity to density may become more important than that of temperature. In this case, the surface water becomes denser at low latitudes, and sinking occurs in the tropics. Then, the surface flow becomes Equatorward, and it is composed of fresh, cold, high-latitude water. The bottom flow is a warm and very salty current flowing towards high latitudes. This type of circulation, "inverted" with respect to that observed today, may have dominated the oceanic circulation in some periods of the past, such as intervals of deglaciation characterized by a large amount of fresh water produced in high-latitude seas from melting glaciers.

In the early sixties, Stommel (1961) proposed a simple low-order model for the thermohaline circulation. This model reduces the oceanic pool to two homogeneous boxes, representing respectively the high-latitude and the tropical halves of the original pool. In such a *box model*, box 1 represents the tropical ocean and box 2 is the high-latitude ocean. The variables of the model are T_1, T_2, S_1, S_2, where T_j is the temperature and S_j the salinity of box j, for $j = 1$ and 2.

The evolution of the system is then modelled by the following equations:

$$\frac{dT_1}{dt} = -\frac{1}{\tau_r}\left(T_1 - \frac{\theta}{2}\right) - \frac{1}{2}Q(\Delta\rho)\Delta T \tag{4.13}$$

$$\frac{dT_2}{dt} = -\frac{1}{\tau_r}\left(T_2 + \frac{\theta}{2}\right) + \frac{1}{2}Q(\Delta\rho)\Delta T \tag{4.14}$$

$$\frac{dS_1}{dt} = \frac{F(t)}{2H}S_0 - \frac{1}{2}Q(\Delta\rho)\Delta S \tag{4.15}$$

$$\frac{dS_2}{dt} = -\frac{F(t)}{2H}S_0 + \frac{1}{2}Q(\Delta\rho)\Delta S, \tag{4.16}$$

where Δ denotes the difference between the two boxes:

$$\Delta T = T_1 - T_2, \qquad \Delta S = S_1 - S_2, \qquad \Delta\rho = \alpha_s \Delta S - \alpha_T \Delta T. \tag{4.17}$$

In equations 4.11 and 4.14, τ_r is the time scale on which the temperature in boxes 1 and 2 relaxes towards $T_0 + \theta/2$ and $T_0 - \theta/2$ respectively. $F(t)$ models the concentrating effect of evaporation in the tropics, or the dilution by precipitation and melting in high-latitude regions; H is the depth of the ocean. This model differs from the original Stommel model in that different "boundary" conditions for salinity are used. In the Stommel model, both temperature and salinity have restoring boundary conditions. Here, restoring boundary conditions are retained for temperature, while for salinity a fixed salinity flux ($F(t)$) is imposed.

The quantity $Q(\Delta\rho)$ is the water flux due to the density difference $\Delta\rho$ between the two boxes. In the past, various forms of $Q(\Delta\rho)$ have been proposed. These include:

$$(i) \qquad Q_1 = \tau_d^{-1}, \tag{4.18}$$

where τ_d is another relaxation time. This is a constant water flux, independent of $\Delta\rho$, and generates linear equations with at most one stable equilibrium.

$$(ii) \qquad Q_2 = \tau_d^{-1} + \frac{9}{v}|\Delta\rho|, \tag{4.19}$$

where v is another parameter. This form of the flux is appropriate for connecting capillary pipes, and was the form originally proposed by Stommel. Recent analyses of ocean circulation models have made the suggestion that this may provide an appropriate parameterization of the water flux (Rahmstorf 1996).

$$(iii) \qquad Q_3 = \tau_d^{-1} + \frac{9}{v}(\Delta\rho)^2, \tag{4.20}$$

a form of the flux based on simple theories of turbulence.

In this model, it is convenient to introduce new variables given by the temperature and salinity differences, ΔT and ΔS. One then obtains, for the evolution of ΔT and ΔS:

$$\frac{d\Delta T}{dt} = -\frac{1}{\tau_r}(\Delta T - \theta) - Q(\Delta\rho)\Delta T \tag{4.21}$$

and

$$\frac{d\Delta S}{dt} = \frac{F(t)}{H}S_0 - Q(\Delta\rho)\Delta S. \tag{4.22}$$

These are the basic equations of the THC two-box model. We next introduce the following nondimensional variables:

$$x = \frac{\Delta T}{\theta} \qquad y = \frac{\alpha_s \Delta S}{\alpha_T \theta} \qquad t' = \tau_d^{-1} t. \tag{4.23}$$

On substituting these variables, with the choice $Q = Q_3$, into equations (4.21) and (4.22), we find the following equations:

$$\frac{dx}{dt} = -\alpha(x-1) - x(1 + \mu^2(x-y)^2) \tag{4.24}$$

and

$$\frac{dy}{dt} = p(t) - y(1 + \mu^2(x-y)^2), \tag{4.25}$$

where

$$\alpha = \frac{\tau_d}{\tau_r}, \qquad \mu^2 = 9\frac{\tau_d(\alpha_T\theta)^2}{v} \qquad \text{and} \qquad p = \frac{\alpha_s S_0 \tau_d F(t)}{\alpha_r \theta H}. \tag{4.26}$$

Equations (4.25)-(4.26) are the nondimensional equations of the THC box model.

In general, the diffusive time scale τ_d is much larger than the relaxation time τ_r, and so the value of α is usually very large. This allows us to simplify the equations still further: On assuming $\alpha \gg 1$, the above equations become

$$x = 1 + O(\alpha^{-1}) \tag{4.27}$$

and

$$\frac{dy}{dt} = -[1 + \mu^2(y^2 - 1)]y + p(t) + O(\alpha^{-1}). \tag{4.28}$$

For the case of constant salinity flux p, Eq. (4.28) can be written in the form of an overdamped oscillator with potential $V(y; p)$:

$$\frac{dy}{dt} = -\frac{\partial V}{\partial y}, \tag{4.29}$$

where

$$V(y; p) = \mu^2 \left(\frac{y^4}{4} - \frac{2y^3}{3} + \frac{y^2}{2} \right) + \frac{y^2}{2} - py \tag{4.30}$$

describes a double-well potential. Thus, the system has two stable equilibria: one corresponds to a direct, temperature-driven circulation, and the other to an inverted, salinity-driven circulation. The two equilibria are separated by a potential barrier and, in the absence of external forcing, the system settles to one of the two steady circulations.

The presence of external noise may, however, induce transitions from one equilibrium state to the other. Cessi explicitly considered the case of a random perturbation superposed on the mean salinity flux. In this case we write $p(t) = \bar{p} + p'(t)$, where $\bar{p}$ is the mean and $p'(t)$ is the perturbation in the salinity flux. Here, p' is modelled described by white noise. The system discussed above now behaves like a particle in the time-independent potential, $V(y; \bar{p})$, subject to a Brownian force, $p'(t)$.

If p' is large enough, the presence of the potential $V(y; \bar{p})$ plays a minor role, and the particle undergoes almost unconstrained Brownian motion. On the other hand, if p' is so small that the perturbed particle cannot cross the potential barrier between the two wells of $V(y; \bar{p})$, then the resulting motion takes the form of a noisy fluctuation around one of the two stable equilibrium points. For intermediate stengths of p', the particle still feels the potential, but it is now able to randomly jump from one well to the other. The resulting motion is a random fluctuation between the two equilibria, with a significant fraction of time spent around each fixed point and intermittent jumps from one state to the other. This case was studied in detail by Cessi, and illustrates how random dynamical noise may induce irregular fluctuations from one attractor to another. Of course, the noise should be of large enough amplitude to force the system to cross the potential barrier between different attractors.

4.4 Stochastic Resonance

In the models described above, if the amplitude of the periodic forcing or noise is too small, then the system does not cross the barriers between the unperturbed attractors. However, if both kinds of perturbations are present, then interesting new effects can arise even when both are sub-threshold. More specifically, for an oscillator with a double potential well, a resonance can occur between the periodicity of the forcing and the (probabilistic) escape rate from each potential well induced by the noise (Benzi *et al.* 1981; McNamara & Weisenfeld 1989; Bulsara & Gammaitoni 1996). This phenomenon has been named *stochastic resonance*.

To illustrate this phenomenon, consider the equation,

$$\frac{dX}{dt} = -\frac{\partial U}{\partial X} + F(t) + A\sin(\omega_0 t), \tag{4.31}$$

where F is a white noise term with the properties $\langle F\rangle = 0$ and $\langle F(t)F(t')\rangle = 2D\delta(t-t')$. Here $\langle ..\rangle$ means ensemble average and $\delta(t-t')$ is a Dirac delta function.

For a potential with a given shape, U, the noise induces occasional escapes from the well. This is characterized by the Kramers escape rate and depends on the noise amplitude, D. Stochastic resonance occurs when the periodicity $2\pi/\omega_0$ of the forcing matches the escape time.

The resonance can be visualized by imagining a quartic potential U with two wells, whose shape is periodically modified by the forcing. At certain phases of the modulation, one of the wells is lower than the other. At that specific time, it is "easier" for the system to pass from the higher equilibrium to the lower. Half a period afterwards, the opposite situation is encountered, and the system is more likely to switch back. If the amplitude of the noise is such that the escape time is similar to the period of the oscillation of the potential well, one observes the birth of a noisy periodicity at the frequency of the forcing. As a result, the system becomes an amplifier, capable of enhancing a small (sub-threshold) external periodic forcing through its noise-driven internal dynamics.

The idea of stochastic forcing was originally introduced by Benzi *et al.* (1982) and Nicolis (1982) as a mechanism for cycles of glaciation, and has been explored further in hundreds of papers since then. The main motivation for this explanation arises from various records of past climatic variability (e.g., the ratio $\delta^{18}O/\delta^{16}O$ in sea sediment cores; see Ghil & Childress 1987) which indicate that glaciations during the last million years possess broad periodicities at about 100,000, 40,000 and 20,000 years. Interestingly, similar periodicities are present in the variations of the Earth's orbital parameters, suggesting a direct orbital forcing on the terrestrial climate. However, by itself, the variation due to orbital changes is definitely too small to account for the large temperature difference between glacial and interglacial periods. Thus, if we want to insist on this explanation, an amplification mechanism is needed.

Stochastic resonance has been proposed explicitly as such a mechanism. In this context, the potential wells are associated with the multiple equilibria of the global climate due to the ice-albedo feedback (see Lecture 2), the periodic forcing is the variation of the Earth's orbit, and the white noise is provided by high-frequency temperature fluctuations in the atmosphere and oceans. To see how the model works, consider the energy balance equation introduced in Lecture 2:

$$c\frac{dT}{dt} = Q(t)[1-\alpha(T)] - \sigma g(T)T^4, \tag{4.32}$$

where the solar forcing Q is now taken to be time-dependent:

$$Q(t) = Q_0(1 + A\cos\omega_0 t) \ . \tag{4.33}$$

Variations in eccentricity of the Earth's orbit have a period of $2\pi/\omega_0 \approx 100,000$ years and an amplitude of $A \approx 10^{-3}$ in units of the mean solar constant, Q_0. For constant solar forcing ($A = 0$), equation (4.32) has three equilibrium solutions, T_1, T_2 and T_3. If the system is located

at one of the stable fixed points, is far from any bifurcations and adjusts rapidly to changes in Q, then the temperature variations through the eccentricity cycle can be computed from the equilibrium curve, $T = T(Q)$, found from equating the right-hand side of (4.32) to zero. For $A = 10^{-3}$ and $T = T_1$ or T_3, this predicts a variation of about 0.1^oC, which is much smaller than the inferred difference in the mean global temperatures between glacial and interglacial periods.

The addition of white noise, however, may cure the problem, as it can lead to stochastic resonance. It is not difficult to see that the addition of a white-noise term with appropriate amplitude to the right-hand side of equation (4.32) is the standard setup of stochastic resonance. Provided the resonance is of sufficient quality, this can force the system to jump from one stable equilibrium to the other, with an amplified, noisy periodicity of 100 kyr.

To conclude, may we say that stochastic resonance is the right explanation for glaciation cycles? Clearly, it is not easy to answer this question. Stochastic resonance is a very important concept, which can be extended to more general situations including non-periodic external forcing, coloured noise, and high-frequency chaotic dynamics replacing stochastic noise. The main problem with this type of resonance, however, is that the noise amplitude must be rather finely tuned to the shape of the potential and to the amplitude and period of the driver in order to obtain significant amplification. For example, stochastic resonance has been invoked in several biophysical and physiological amplification mechanisms; here, however, one can imagine that the system has evolved to a state in which amplification is optimized (e.g., natural selection could have tuned the shape of the potential). In the climatic case, however, there is no reason why the resonance should be there a priori, and it would be a fortunate coincidence if the amplitude of the noise induced by weather variability were resonating with the shape of the climatic potential and the periodicity of the orbital variations. Of course, more work is needed in order to understand whether some form of resonance can be observed in more complicated dynamical systems with less stringent requirements.

Lecture 5

Chaos driving Chaos

In Lecture 4 we have explored some examples of what can happen when a nonlinear dynamical system is driven by external periodic forcing, noise, or a combination of both. Here, we briefly consider the case of a nonlinear system, call it system B, which is driven by another nonlinear system (the driver), which we call system A. A particularly interesting situation is when there is no feedback of the driven system on the driver. Such systems are often more easily understood than systems that drive each other. Mathematically, the global system formed by A plus B is said to have a *skew-product structure*. An example of this is provided by the solar forcing on terrestrial climate, where the Sun is the driver, the climate is driven, and most people think that there is no feedback of the Earth's climate on the solar output.

5.1 On-off intermittency

In driven-driver systems with skew-product structure, many interesting things can happen. Among these, we concentrate on the phenomenon called *on-off intermittency*, which produces bursting behavior in the output of the driven system (see e.g. Platt, Spiegel & Tresser 1993a). A second possible phenomenon is synchronization, which we consider in the next lecture.

Consider the general system

$$\dot{\mathbf{X}} = \mathbf{F}(\mathbf{X}, \mathbf{Y})$$

and

$$\dot{\mathbf{Y}} = \mathbf{G}(\mathbf{Y}),$$

with $\mathbf{X} \in \mathcal{R}^k$, $\mathbf{Y} \in \mathcal{R}^{n-k}$. The dimensionality of the whole system is n. We suppose that the global system has an invariant manifold in the subspace $\mathbf{X} = \mathbf{0}$. That is, if $\mathbf{X} = \mathbf{0}$ initially, then it will remain so, whatever the vaue of $\mathbf{Y}$. We also suppose, however, that the stability of the manifold $\mathbf{X} = \mathbf{0}$ depends on the value of $\mathbf{Y}$. More specifically, we briefly ignore the evolution equation for $\mathbf{Y}$ and consider $\mathbf{Y}$ to be a constant parameter in the equation determining $\mathbf{X}$. Then, the invariant object, $\mathbf{X} = \mathbf{0}$, has stability characteristics depeding on the value of $\mathbf{Y}$. The important feature of the system is that there is a region of the phase space for $\mathbf{Y}$ for which

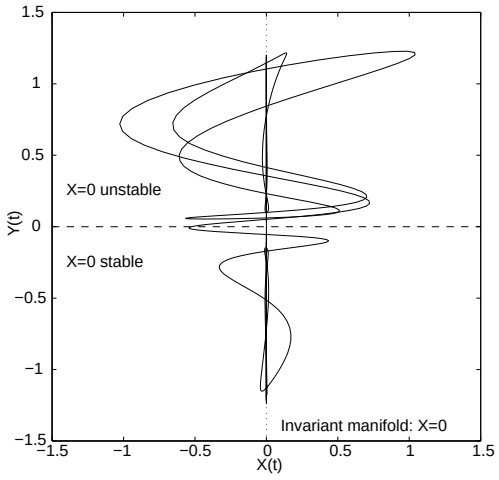

Figure 5.1: Effect of the variations of the driver Y on the dynamics of X. The variable Y controls the stability of the invariant manifold $X = 0$ of the driven system; where Y is positive, $X = 0$ is unstable, and where it is negative, the invariant manifold is stable.

$\mathbf{X} = \mathbf{0}$ is stable, the region $\mathcal{S}$ say. But if $\mathbf{Y}$ lies outside this region, then $\mathbf{X} = \mathbf{0}$ is unstable:

$$Y \in \mathcal{S} \Rightarrow \mathrm{X} = 0 \, is \; stable$$

$$Y \notin \mathcal{S} \Rightarrow \mathrm{X} = 0 \, is \; unstable.$$

Now let $\mathbf{Y}$ evolve according to its own equation. The driver is set up such that the trajectory of the solution, $\mathbf{Y}(t)$ wanders through the phase space, with some periods of time spent largely in $\mathcal{S}$, then other intervals mainly outside this region. This means that the driver alternates between periods in which it typically stabilizies the invariant manifold, and intervals over which it destabilizes $\mathbf{X} = \mathbf{0}$. As a result, the variable $\mathbf{X}$ may spend long periods of time in the proximity of $\mathbf{X} = \mathbf{0}$, and undergo sudden bursts of activity far from $\mathbf{X} = \mathbf{0}$ when the driver makes that manifold unstable.

In the simplest case, $\mathbf{X} = \mathbf{0}$ is a fixed point, but in general the invariant manifold can contain an attractor of whatever dimensionality less than k. On-off intermittency thus provides a simple mechanism for bursting away from an attractor in low-dimensional systems. Figure 5.1 illustrates the behaviour.

A simple example of on-off intermittency is provided by the map,

$$X(n+1) = R(n)\, X(n)\, [1 - X(n)] \tag{5.1}$$

in which we vary the control parameter, $R(n)$, according to another logistic map:

$$R(n) = aY(n) + b \tag{5.2}$$

and

$$Y(n+1) = 4Y(n)[1 - Y(n)] \tag{5.3}$$

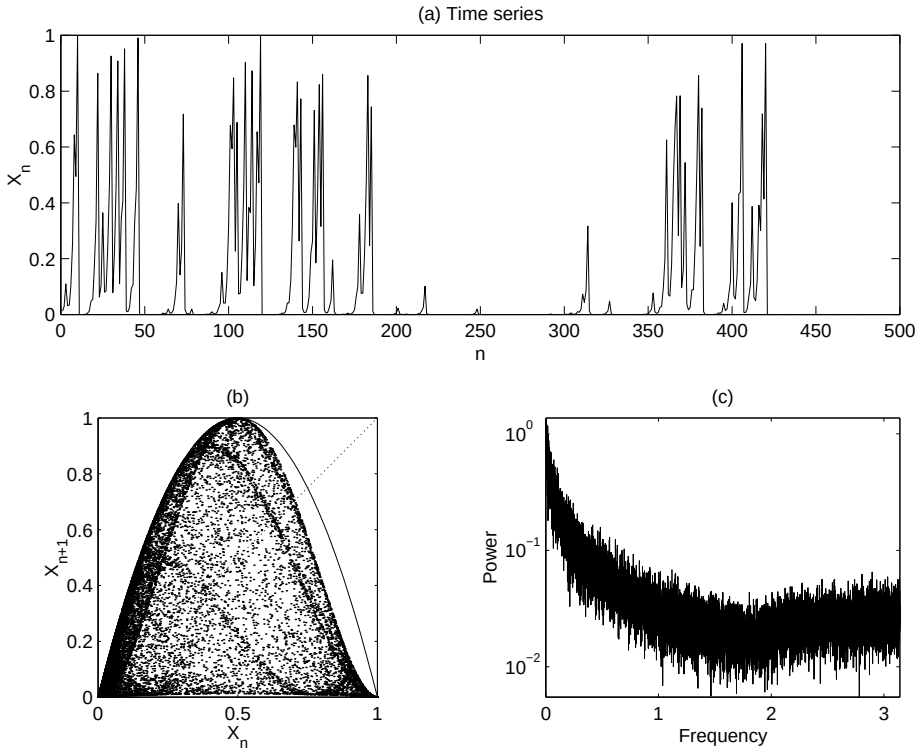

Figure 5.2: On-off intermittency in the coupled maps (5.2)-(5.3). Panel (a) shows a short time series of X_n; the dotted lines indicate the corresponding signal of Y_n. In (b) we display X_n against X_{n+1}, and in (c) a power spectrum obtained from averaging spectra from ten different realizations of the system.

with $a = 3.95$ and $b = 0.05$. Figure 5.2 shows a time series of $X(n)$, which shows the bursty behavior typical of this form of intermittency. Time series of this kind are characterized by a *red* power spectrum (i.e., a spectrum with ever-increasing variance at low frequencies Balmforth *et al.* 1999; see figure 5.2c).

5.2 A model of the intermittent solar cycle

On-off intermittency has been proposed as a possible mechanism for the alternation between active and inactive periods in the solar dynamo (Platt, Spiegel & Tresser 1993b).

Sunspots are formed where strong magnetic fields inhibit fluid convection and the flow of heat in the turbulent solar envelope; where the fields pierce the solar photosphere, the magnetized fluid appears dark. The spots persist for timescale of order weeks, and understanding their origin is one of the most challenging problems in solar physics.

One of the most surprising aspects of sunspot phenomemology is the *solar cycle*: the

number of sunspots observed on the solar surface varies roughly periodically with a timescale of eleven years or so. Though this eleven-year cycle appears to have existed for centuries, it does not appear to have maintained a constant amplitude. Notably, during the "Maunder Minimum" in the seventeenth century, there was a significant shortage of sunspots.

To rationalize the appearance of the Maunder Minimum (and other apparent declines in the solar activity) we turn to another metaphor. This time we interpret the Minimum in terms of the "off" period of an intermittent, low-order dynamical system. The particular system we choose is that described by Platt, Spiegel & Tresser. There are crude physical arguments supporting this model; at the risk of sounding ridiculous, we repeat some of these.

The solar cycle is basically a magnetohydrodynamical phenomenon. Our image behind the cycle is one in which magnetic flux is amplified by dynamo action in the convective solar envelope, then is swept into localized tubes by the action of turbulemt eddies. These tubes contain sufficient flux to impede the fluid flow and maintain their structure in the face of the turbulence. Upto this point, the image is plausible and largely agreed upon by solar physicists; beyond it, however, the image becomes sketchy and more controversial. The tubes are transported around by large-scale convective cells and ultimately expelled beneath the convection zone. Here, they build up in a thin zone between the radiative interior and the convective envelope where there is a high degree of shear due to the differential solar rotation. This is the solar tachocline. Here too, there is dynamo action due to the differential rotation. But it is the evolution of this magnetic layer on a longer timescale that may be responsible for producing the solar cycle.

To model the magnetic tachocline we take a nonlinear oscillator such as might be expected from a simple dynamo process:

$$\dot{x} = \beta x - \omega y - (x^2 + y^2)x \tag{5.4}$$

and

$$\dot{y} = \omega x + \beta y - (x^2 + y^2)y, \tag{5.5}$$

where ω is the frequency of the oscillator, and β is its growth rate. x and y could be, for example, the time-dependent amplitudes of a spatial mode as in the Galerkin projection described in lecture 2.

If β were constant, the oscillator models the magnetic content of the tachocline and its amplification through the action of differential rotation. But there is also the magnetic flux tubes that are expelled from the convection zone above, and "rain down" onto the tachocline. We account for this effect by adopting a time-dependent form for β that includes a term modelling the fluctuating process which adds to the field. In particular, we describe the turbulent convective dynamo by the Moore-Spiegel model (Moore & Spiegel 1966):

$$\ddot{X} = AX - X^3 - B\dot{X} + Z \tag{5.6}$$

$$\dot{Z} = -\delta[Z - CX(X^2 - 1)], \tag{5.7}$$

where A, B,δ and C are parameters. Again, $X(t)$ and $Z(t)$ could be the amplitudes of Galerkin modes. Then, we define

$$\beta = \beta_0(X - X_0), \tag{5.8}$$

where β_0 and X_0 are constants. This form for β is then fed into the oscillator equations (5.4)-(5.5).

A solution to our model system (5.4)-(5.8) is shown in figure 5.3. This shows how the activity in $x^2(t)$ bursts intermittently in the fashion of the on-off mechanism. Note that the dimensionless time unit corresponds to several years; the duration of the quiescent phases is of order 50 years.

Notably, outbursts are closely correlated with the periods over which $X(t)$ takes positive values. Evidently, in this model, the Maunder minimum and it predecessors should have a rough periodicity given by the timescale on which the Moore-Spiegel oscillator crosses from one side of the "bowtie" to the other (about 50 of the dimensionless time units). This feature of the model is not actually consistent with observations, calling, perhaps, for some further parameter tuning.

A simple modification of this model, that provides a more realistic alternance between active periods and "Grand Minima" (quiescent phases such as the Maunder Minimum), is obtained by breaking the skew-product structure of the system and introducing a small feedback of (x, y) on (X, Z) (Claudia Pasquero, *Thesis of Laurea*, 1996). This specific example indicates that, often, a richer behavior is found in systems which do not have a pure skew-product structure, but rather allow for a small feedback of the driven system on the driver. In these systems, the basic mechanism of on-off intermittency is still present, even though it is slightly modified by the presence of the (small) feedback. In the words of Ed Spiegel, these are systems with "broken asymmetry."

5.3 In search for the motor

We now return to pure skew-product nonlinear systems, and consider their properties from the point of view of time series analysis. In particular, we can imagine a situation where we measure only the output of the driven system B (thus considering what one might call a non-generic variable), and try to reconstruct some of the properties of the whole system, or of its individual constituents, A (the driver) and B.

Among the possible questions, we concentrate on the following one: Given that we have measured the output of the driven system, what can we say about the properties of the driver? In this context, we consider the driven system as a nonlinear dynamical filter acting on the driver, and we want to extract the characteristics of the driver embedded in the driven behavior. An example of this situation is when we attempt to extract from analysis of climatic data the hidden solar forcing.

In general, this question does not have a simple or unique answer, as the possibility of detecting a sign of the driver in the dynamics of the driven system depends on the nature of both systems, and on the strength of the driving. Thus, we qualify the above question, and explore whether we can at least distinguish between stochastic and deterministic driving in a system undergoing on-off intermittency (Platt, Spiegel & Tresser 1993a; von Hardenberg *et al.* 1997).

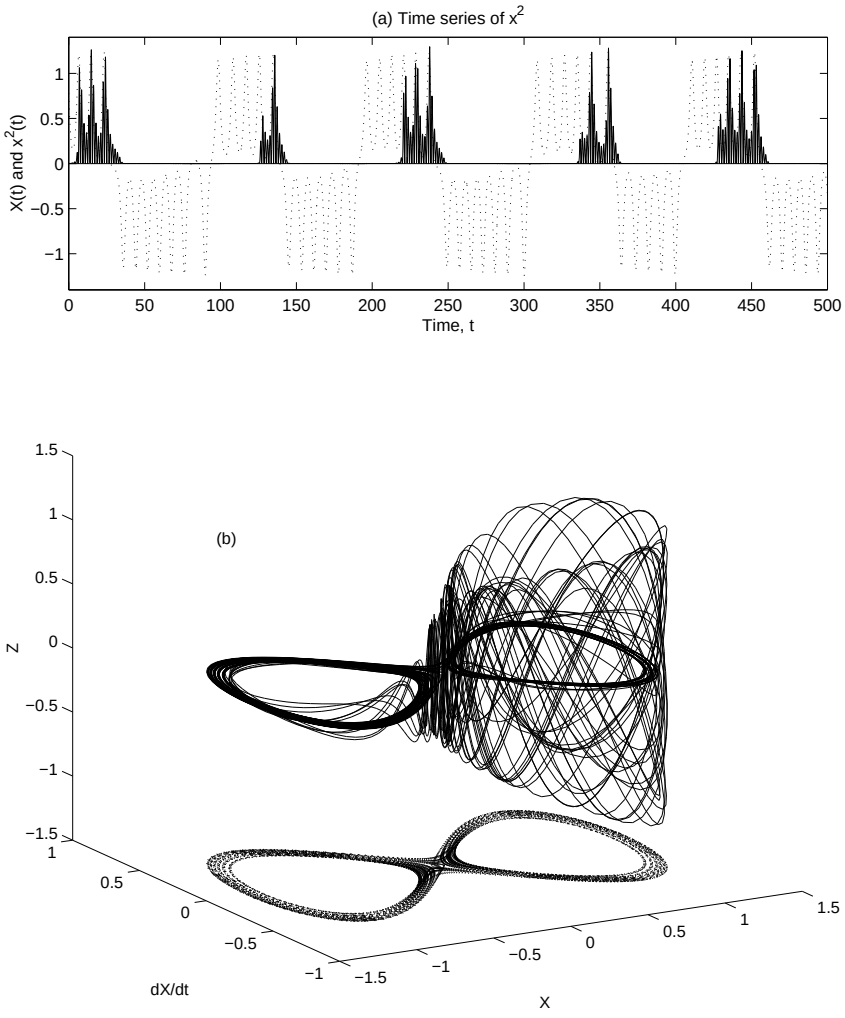

Figure 5.3: Intermittent solution of the system (5.4)-(5.8), with $A = 0.7$, $B = 0$, $C = -0.5$, $\delta = 0.03$, $\omega = 2$, $\beta_0 = 1$ and $X_0 = -0.15$. Panel (a) shows a time series of $x^2(t)$ (solid lines) and $X(t)$ (dotted lines), and panel (b) shows a phase portrait in $(X, \dot{X}, x)-$space; the projection of the Moore-Spiegel attractor is also displayed.

To this end, consider a simple tent-like map

$$x_{n+1} = \begin{cases} \mu x_n & x_n \leq \frac{1}{4} \\ \frac{\mu}{3}(1 - x_n) & x_n > \frac{1}{4}, \end{cases} \tag{5.9}$$

where μ is the control parameter. This map has a fixed point at $x_n = 0$; it is stable for $\mu < 1$ and unstable otherwise. For $\mu > 1$ there is another fixed point at $x_1 = \mu/(\mu + 3)$, which is stable for $\mu \leq 3$ and unstable otherwise.

Now, let us suppose that the control parameter is not constant, but varies according to another dynamics, which pushes it across the bifurcation sequence of the driven system. The dynamics of the control parameter is described by

$$\mu = a y_n \tag{5.10}$$

where a is a coupling constant. For the driver y_n, we take either a stochastic model,

$$y_n = \text{ white noise}, \tag{5.11}$$

or a low-dimensional dynamical system,

$$y_{n+1} = 2y_n (\text{mod } 1). \tag{5.12}$$

In both cases, the driven map displays on-off intermittency, with long periods of quiet behavior intermixed with spikes of strong activity. Figure 5.4 shows two time series of the x_n variable, for the deterministic driver (panel a) and the white noise driver (panel b). In general, the amount of bursting is controlled by the value of a, and it is possible to find (different) values of a such that signals produced by the deterministically and the stochastically driven maps are apparently indistinguishable.

The indistinguishability extends also to simple calculations of the correlation dimension D_2, the Lyapunov exponents, or other dynamical measures obtained from a time embedding of the output of the driven system. For example, using $a = 2.88$ for the white noise and $a = 3.5$ for the deterministic driver gives the same correlation dimension in the embedded output signal. In other words, standard techniques do not appear to be able to distinguish stochastic and determinisitic, on-off signals. Worse still, the application of surrogate data tests (phase randomization, etc) is also of limited help, as the two signals remain apparently indistinguishable.

However, a clear (albeit qualitative) difference between the stochastic and deterministic drivers can be seen by plotting x_{n+1} vs x_n (panels (c) and (d) of figure 5.4; see also figure 5.2). The stochastic driver has a power-law divergence in the density of points near the origin and a uniform distribution of points far from the origin, while the deterministic driver has complicated large-scale structures in addition to the density divergence around $x = 0$. The strong clustering of points near the origin is a result of the off periods, present for both stochastic and deterministic driving, and it strongly influences the dimension determination. In fact, the approximate power-law distribution of points near the origin in phase-space induces a spuriously small value of the correlation dimension, that wipes out the dynamically significant

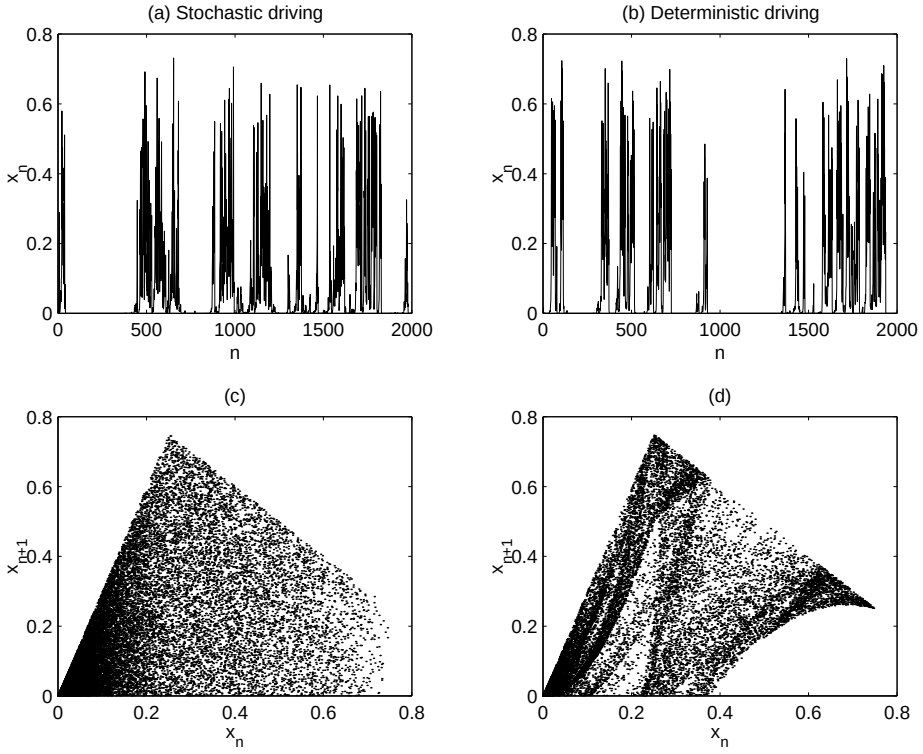

Figure 5.4: On-off intermittency in the coupled maps (5.9)-(5.12). The first two panels show short time series of x_n for (a) stochastic and (b) deterministic driving. Panels (c) and (d) show the same results plotted on the (x_n, x_{n+1}) plane. $a = 3$.

differences between the stochastic and the deterministic driving which are present in the other portions of phase space.

To distinguish properly between the two drivers, one needs to reduce the effect of the points near the origin. To this goal, Hardenberg *et al.* have proposed to modify the definition of distance in phase space, in order to "spread" the points clustered near $x = 0$ and consequently allow for the dynamical differences to appear. With this modification, it was then shown that the correlation dimension takes the correct value, allowing for a distinction between the two types of driver. This result was achieved, however, only after a close scrutiny of the data, as the "automatic" procedures employed did not provide the correct results. This story indicates that one has to be careful when analysing the dynamics generated by on-off intermittent signal, as standard methods can give misleading results. Nevertheless, in this specific case, the other side of the coin is that a careful analysis of the reconstructed dynamics gives information on the nature of the driver, even if though it is processed by a bursting, nonlinear dynamical filter.

5.4 More intermittency

In this lecture we have explored some of the properties of systems undergoing on-off intermittency. However, "intermittency" is an abused term in nonlinear dynamics. For this reason, we now briefly mention some of the main usages of this term.

The most elementary, and general, definition of intermittency is in terms of the probability distribution of extreme fluctuations. For an intermittent system, large fluctuations (extreme events) are much more probable than for a gaussian process. In this sense, a system with slowly-decaying tails in the probability distribution of the dynamical quantities that characterize it can be called intermittent. Thus, an intermittent signal has non-gaussian probability distributions (for example, with exponential or power-law tails), and it cannot be generated by a linear process. The linear Orstein-Uhlenbeck process discussed in Lecture 3 is non-intermittent, while its nonlinear extension, also discussed there, is "intermittent." (This is evident from the probability distributions displayed in that lecture; figure 3.3.) Note, however, that a simple nonlinear change of variables may make a linear signal to appear intermittent. Thus, this definition of intermittency does not distinguish between signals produced by a truly nonlinear dynamical system and linear signals that have been nonlinearly transformed.

A more quantitative measure of intermittency is provided by the study of the (possibly) multifractal properties of the signal. Multifractality can be uncovered by evaluating the structure functions of order m:

$$S_m(\tau) = < |x(t+\tau) - x(t)|^m >_t$$

where $x(t)$ is the time series under study and $< .. >_t$ indicates a time average along the signal. The parameter m defines the order of the moment. For a signal characterized by scaling properties (a fractal signal), one has that

$$S_m(\tau) \propto \tau^{\zeta(m)}$$

at small τ. Moreover, for a multifractal, intermittent signal, $\zeta(m)$ increases more slowly than m, and so $\zeta(m)/m$ is a decreasing function. Thus, detecting decreasing values of $\zeta(m)/m$ for increasing m is a sign of intermittency. One must keep in mind, however, that statistical errors and limitations become stronger and stronger as the order of the moment increases, and spurious positive results can be easily found (see e.g. Provenzale *et al.* 1993).

Another way of quantifying intermittency is by the evaluation of the generalized dimensions, D_q. For a multifractal signal, the generalized dimensions, D_q, decrease with increasing q. Various definitions of the generalized dimensions are possible; here, we use the simplest and most intuitive one. To this end, first define a probability measure, $p(t)$, from the measured signal $x(t)$. For example, one may use $p(t) = x(t)$ for a signal produced by one of the intermittent maps discussed above, or $p(t) = (dx/dt)^2$ for a signal provided by a velocity measurement in a turbulent flow. The choice of the measure is crucial, and it should be dictated by the physics of the system under study. Unfortunately, many details of the results depend on the choice of the measure. Definitions which do not employ a measure are possible, and used in several contexts. Here, however, for simplicity we stick to the definitions based on a measure $p(t)$.

Once we choose a measure, we then define

$$P_i(\Delta) = \int_{t_i - \frac{\Delta}{2}}^{t_i + \frac{\Delta}{2}} p(t)\, dt$$

and

$$B(\Delta, q) = \sum_{i=1}^{L} [P_i(\Delta)]^q$$

where time is been divided into L segments of duration Δ. Note also that the above definition is not correct for $q = 1$, in this case one should use

$$B(\Delta, 1) = \sum_{i=1}^{L} [P_i(\Delta)] \log P_i(\Delta)$$

If the chosen measure is self-affine, then in the limit $\Delta \to 0$ one finds that

$$B(\Delta, q) \sim \Delta^{(q-1)D_q}$$

where the D_q's are the generalized fractal dimensions, and q is the order of the moment.

If the measure is almost always non-zero on the time axis (so the measure "fills" the line), then $D_0 = 1$. This implies that the chosen measure has no fractally-distributed "holes" on the time axis. For monofractal, non-intermittent measures, $D_q = D_0$ for all q. In contrast, for an intermittent measure the generalized dimensions D_q decrease with increasing q.

For example, the linear Ornstein-Uhlenbeck process of Lecture 3 generates signals with $D_q \approx 1$ for all q, when the measure $p(t) = (dx/dt)^2$ is used. By contrast, the nonlinear version of the process generates multifractal signals which are intermittent: $D_0 = 1$ and $D_q < D_{q'}$ for $q > q'$. For this process, therefore, the simple definition of intermittency based on the

distribution of the dynamical variable coincides with the more sophisticated definition based on the multifractal nature of the signal.

In the dynamical systems folklore, at least another definition of intermittency has been introduced (Pomeau & Manneville 1980). This type of intermittency is observed when the system is close to a bifurcation. A particularly visible example arises for a one-dimensional map near a saddle-node bifurcation. Figure 5.5 shows one such example; this is the logistic map, with parameter r set to be just below the point at which the period–3 orbit appears in a saddle-node bifurcation. As shown in the first panel, the third iterate of the map then contains three points that are very close to the diagonal; these points touch the diagonal and develop into equilibria as we pass through the saddle node on raising r. Whenever the system passes close to one of these points, it spends a significant amount of time in that "bottleneck". As a result, one observes long periods of quiescent behavior with occasional bursting away from the region where the curve representing the map and the 45^o line almost intersect. This behavior, however, is strictly associated with an incipient saddle-node (or other) bifurcation and requires a very fine tuning of parameters. It is therefore less generic than the on-off intermittent bursting discussed above.

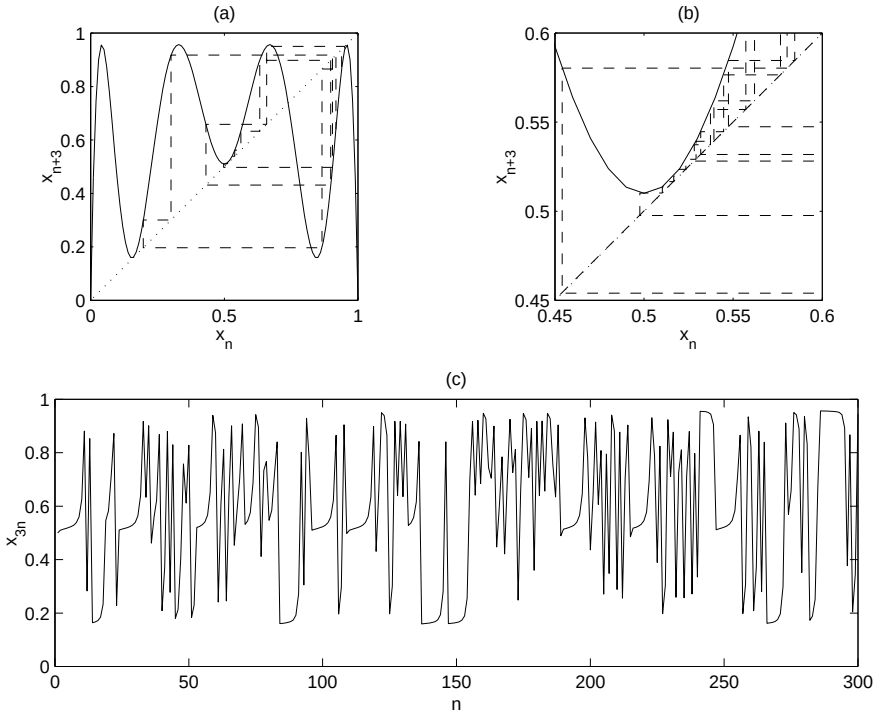

Figure 5.5: Pomeau-Manneville type I intermittency in the logistic map, $x_{n+1} = rx_n(1 - x_n)$ with $r = 3.827$. Every third iteration is shown which illustrates the close passage of the trajectory (the dashed lines) to the points that, for larger r, develop into the period-3 orbit. The first panel shows the map, and the second a magnification around the middle "bottleneck". The third panel shows part of the time series.

Lecture 6

Coupled Chaos

In lecture 5 we have studied the situation where one system (the driver) forces another (the driven). We now turn to the general issue of the dynamics of coupled systems.

There are many instances in which such dynamics are relevant to geophysics and astrophysics. For example, oceanographers often account for the atmosphere in terms of only a simply wind forcing in their circulation models, and meteorologists occasionally ignore the ocean altogether. But, as every climate dynamicist appreciates, the two are intimately coupled, and many phenomena in the global climate arise as a result of the coupling.

In this lecture we focus on some consequences of coupling that can be explored using simple dynamical systems. The possible synchronization of dynamically similar systems is the first such consequence that we discuss. The second issue we raise is, given that the system we consider is composed of coupled elements with complicated internal dynamics, how much can we say about the full system if we have information from only one of its subsystems. It turns out that a full reconstruction is impossible. Then we follow on to explore systems with widely different timescales, and describe tools that attempt to distinguish between fast and slow dynamics. These tools have some degree of success and lead us to hope that it might prove possible to "filter out" the faster dynamics in favour of understanding the slower processes that are at work in real applications.

These latter issues have obvious application to weather prediction, where we attempt to forecast the future of a complicated, coupled system with many timescales given information from only certain observing "sites" on certain subsystems.

6.1 Synchronization of Coupled Systems

In 1673, Huygens observed the phase-locking of two clocks. He attributed this *synchronization* to a weak coupling of the clocks. However, the phenomenon occurs in much more general situations, and with whole arrays of coupled systems. For example, one of the most spectacular (and also frequently cited) properties of populations of coupled nonlinear oscillators is the convergence to mutual synchrony which is observed in many contexts, ranging from firefly communities and networks of neurons to charge density waves.

These examples invariably involve simple oscillators for which coupling opens up the possibility of synchronization in phase; the oscillators, in fact, need not even be identical. But the systems that we hope to explore in geophysics and astrophysics are composed of much more complicated subsystems. In fact, the subsystems we would typically like to couple together are chaotic. But, can chaotic systems synchronize?

One of the hallmarks of chaos is the sensitivity to the initial condition of the system. This means that two identical systems with slightly different initial states will diverge from one another in phase space exponentially quickly. This idea conveys the impression that chaotic systems are difficult to control and, in particular, if we couple two together, the systems are unlikely to follow identical orbits. In fact, this is not the case; chaotic systems can synchronize.

To illustrate the point consider two identical dynamical systems that, in isolation, are described by the equation $\dot{\mathbf{x}} = \mathbf{f}(\mathbf{x})$. We may coupled the systems together in various ways, some of which will be mentioned shortly. However, for the moment, we introduce one of the simplest form of coupling:

$$\dot{\mathbf{x}}_1 = \mathbf{f}(\mathbf{x}_1) + \epsilon(\mathbf{x}_2 - \mathbf{x}_1) \qquad \text{and} \qquad \dot{\mathbf{x}}_2 = \mathbf{f}(\mathbf{x}_2) + \epsilon(\mathbf{x}_1 - \mathbf{x}_2). \tag{6.1}$$

Here, ϵ measures the strength of the coupling.

Clearly, if $\epsilon = 0$, the two systems are uncoupled and freely evolve. Provided the two systems are chaotic, there is no reason to believe that they will synchronize. However, $\mathbf{x}_1 = \mathbf{x}_2$ is nevertheless a solution. In fact, this is a solution for all ϵ; that is, it is an invariant manifold. We call this object the *synchronization manifold* of the coupled system, and it is described by an orbit of the uncoupled equations. Note that the synchronization manifold must be an invariant manifold of the full system, or synchronization is not possible. This means that non-identical systems do not normally synchronize.

For ϵ sufficiently small, the coupling is too weak to affect appreciably each subsystem and so they must again evolve almost independently. The sensitivity to initial condition implies that the two susbsystems diverge from one another if they are initially close. Hence the synchronization manifold is in this sense *unstable*.

At large coupling strength, on the other hand, the largest terms in the equations are the coupling terms, and so (as Ed Spiegel puts it) "they must be zero". In other words, there are no terms in the equations that can balance the strong coupling other than the time derivative:

$$\dot{\mathbf{x}}_1 \sim \epsilon(\mathbf{x}_2 - \mathbf{x}_1) \qquad \text{and} \qquad \dot{\mathbf{x}}_2 \sim \epsilon(\mathbf{x}_1 - \mathbf{x}_2). \tag{6.2}$$

This simplified system predicts a relaxation to the synchronization manifold. Equivalently, when ϵ is large, we *slave* the subsystems to one another and adiabatically eliminate one variable in favour of the other (to use the terminology of amplitude expansions).

Thus even chaotic systems can synchronize. This remains the case even for very different forms of coupling as some of the examples to follow indicate. Before describing these examples, we first formalize the definition of stability of the synchronization manifold.

Consider the coupled systems,

$$\dot{\mathbf{x}}_1 = \mathbf{F}(\mathbf{x}_1, \mathbf{x}_2; \epsilon) \qquad \text{and} \qquad \dot{\mathbf{x}}_2 = \mathbf{F}(\mathbf{x}_2, \mathbf{x}_1; \epsilon). \tag{6.3}$$

This generally expresses the form of two symmetrically coupled systems with coupling strength ϵ. We consider an orbit in the synchronization manifold, $\mathbf{x}_1 = \mathbf{x}_2 = \mathbf{x}$, and then perturb the system around this trajectory:

$$\mathbf{x}_1 = \mathbf{x} + \mathbf{u}_1 \qquad \text{and} \qquad \mathbf{x}_2 = \mathbf{x} + \mathbf{u}_2, \tag{6.4}$$

with $|\mathbf{u}_1| \ll 1$ and $|\mathbf{u}_2| \ll 1$. By substituting these forms into the system (6.3) and linearizing, we arrive at

$$\dot{\mathbf{u}}_1 = \mathbf{F}_1\mathbf{u}_1 + \mathbf{F}_2\mathbf{u}_2 \qquad \text{and} \qquad \dot{\mathbf{u}}_2 = \mathbf{F}_2\mathbf{u}_1 + \mathbf{F}_1\mathbf{u}_2, \tag{6.5}$$

where

$$\mathbf{F}_1 = \left[\frac{\partial \mathbf{F}(\mathbf{x}_2, \mathbf{x}_1; \epsilon)}{\partial \mathbf{x}_1}\right]_{\mathbf{x}_1=\mathbf{x}_2=\mathbf{x}} \qquad \text{and} \qquad \mathbf{F}_2 = \left[\frac{\partial \mathbf{F}(\mathbf{x}_2, \mathbf{x}_1; \epsilon)}{\partial \mathbf{x}_2}\right]_{\mathbf{x}_1=\mathbf{x}_2=\mathbf{x}}. \tag{6.6}$$

Thus,

$$\dot{\mathbf{u}}_1 + \dot{\mathbf{u}}_2 = (\mathbf{F}_1 + \mathbf{F}_2)(\mathbf{u}_1 + \mathbf{u}_2) \tag{6.7}$$

and

$$\dot{\mathbf{u}}_1 - \dot{\mathbf{u}}_2 = (\mathbf{F}_1 - \mathbf{F}_2)(\mathbf{u}_1 - \mathbf{u}_2). \tag{6.8}$$

The formulation of the stability problem in terms of the sums and differences effectively organizes the perturbation in terms of a component that preserves the synchronization and one that destroys it. The second component therefore describes perturbations away from, or *transverse* to, the synchronization manifold.

Both linear systems (6.7) and (6.8) are not straightforward to solve: the coefficients embodied in $\mathbf{F}_1 \pm \mathbf{F}_2$ involve the variables describing the synchronized, chaotic trajectory. Thus we can only make sense of stability in terms of a temporal average. In fact, the system (6.7) corresponds to the stability of the orbit inside the synchronization manifold, and therefore is identical to the system that one must solve to compute the Lyapunov exponents, λ, of the uncoupled system.

Likewise, the solution of the transverse stability equation (6.8) is understood in terms of exponents much like Lyapunov exponents:

$$\mathbf{u}_\perp \equiv \mathbf{u}_1 - \mathbf{u}_2 \sim \exp \Lambda t \qquad \text{as } t \to \infty. \tag{6.9}$$

The synchronization exponent, Λ, is sometimes called the *transverse stability* or *Lyapunov exponent*, or the *conditional Lyapunov exponent*. Provided the leading exponent, Λ_1 say, is negative, the synchronization manifold is stable in the sense of a linearized perturbation and an infinite-time average.

The organization into synchronized and transverse perturbations follows also for systems that are not coupled symmetrically. Hence, we may define transverse stability exponents whatever the form of coupling. These dictate the stability of the synchronization manifold. However, since we can only understand the stability exponents in terms of the limits of infinite time and infinitesimal perturbation, there are some limitations on how useful these exponents really are in predicting synchronization: sometimes systems can desynchronize due to finite time and amplitude effects even in situations in which the stability exponents predict that the synchronization manifold is stable (Pecora *et al.* 1997).

We next describe some specific examples of synchronizing chaotic systems. These illustrations all involve cases in which the subsystems can synchronize *exactly*. That is, situations for which $\mathbf{x}_1 - \mathbf{x}_2 \to 0$ as $t \to \infty$. However, more general forms of synchronization are also possible. For example, systems can synchronize upto an amplitude scaling, a phase lag, or some particular functional relationship. There are also weaker forms of synchrony in which the phase of the oscillators shows some degree of synchrony, but the amplitudes remain unsynchronized; this is called "phase synchronization" (Rosenblum *et al.*, 1996). With these generalized definitions, it becomes possible to synchronize non-identical chaotic elements.

Complete replacement

The most commonly cited example of chaotic synchronization involves a special form of coupling that involves the complete replacement of a variable in one subsystem with the corresponding variable from another (Pecora & Carroll 1990). This coupling is quite different from that used above because one system evolves independently of the other, and we must throw away the equation for the replaced variable, which is now redundant. This one-way coupling scheme is also called "master-slave" synchronization, and is an example of a system with skew-product structure.

By way of example, we couple two Lorenz '63 systems $\{x_1, y_1, z_1\}$ and $\{x_2, y_2, z_2\}$ via the complete replacement $x_2 \to x_1$. This produces the system,

$$\begin{aligned} \dot{x}_1 &= -\sigma(y_1 - x_1) \\ \dot{y}_1 &= -x_1 z_1 + r x_1 - y_1 \\ \dot{z}_1 &= x_1 y_1 - b z_1 \\ \dot{y}_2 &= -x_1 z_2 + r x_1 - y_2 \\ \dot{z}_2 &= x_1 y_2 - b z_2. \end{aligned} \tag{6.10}$$

Alternatively, we may write the system in terms of the Lorenz equations and two equations for the differences, $\Delta_y = y_2 - y_1$ and $\Delta_z = z_2 - z_1$:

$$\begin{aligned} \dot{\Delta}_y &= -x_1 \Delta_z - \Delta_y \\ \dot{\Delta}_z &= x_1 \Delta_y - b \Delta_z. \end{aligned} \tag{6.11}$$

A pictorial representation of the synchronization manifold, given by $\Delta_y = \Delta_z = 0$, is displayed in figure 6.1. Parameter values are the usual $r = 28$, $\sigma = 10$ and $b = 8/3$. The solid lines show a solution that converges to the synchronizes manifold, suggesting that this object is stable.

In fact, the coupled system *always* synchronizes: equations (6.11) can be combined into the relation,

$$\frac{1}{2}\frac{d}{dt}(\Delta_y^2 + \Delta_z^2) = -\Delta_y^2 - b\Delta_z^2. \tag{6.12}$$

The right-hand side of this expression is always negative, provided one of Δ_y and Δ_z is finite (and b is positive). This indicates the differentiated quantity on the left must decrease in time to its minumum value, which is $\Delta_x = \Delta_y = 0$. Thus, synchronization is the fate of the system. (This argument amounts to the identification of a Lyapunov functional.)

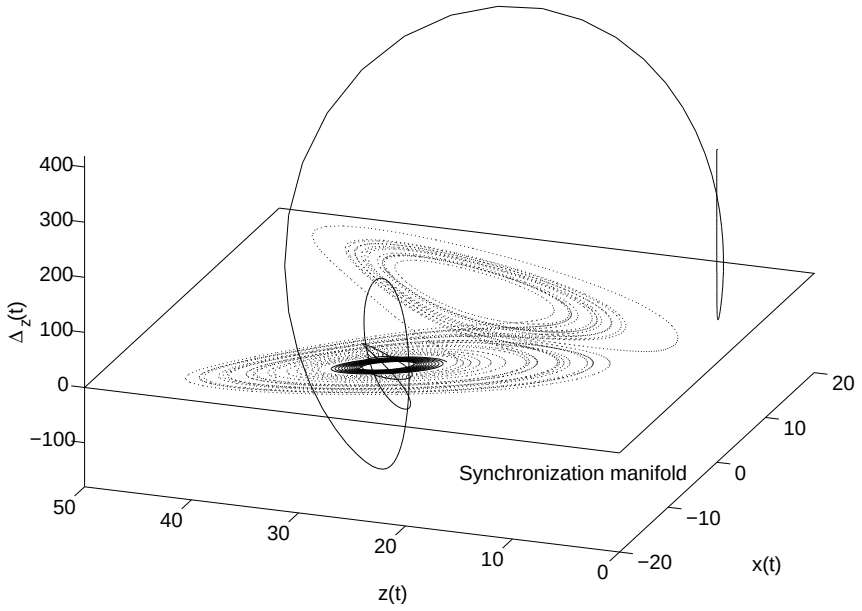

Figure 6.1: A projection of the synchronization manifold for two Lorenz '63 systems coupled through the complete replacement of the $x-$variable of one subsystem. The solid line shows a sample orbit converging to synchrony.

Coupled Rossler systems

Both the coupled Lorenz systems and the example used to introduce the concept of chaotic synchronization exhibit synchronization, but this behaviour is by no means automatic. Moreover, for different forms of coupling, it is not necessarily the case that the systems synchronize for sufficiently large coupling strength.

For example, two Rössler systems can be coupled as follows:

$$\begin{aligned} \dot{x}_1 &= -(y_1 + z_1) \\ \dot{y}_1 &= x_1 + a y_1 \\ \dot{z}_1 &= b + z_1(x_1 - c) \\ \dot{x}_2 &= -(y_2 + z_2) + \alpha(x_1 - x_2) \\ \dot{y}_2 &= x_2 + a y_2 \\ \dot{z}_2 &= b + z_2(x_2 - c) \end{aligned} \tag{6.13}$$

(*cf.* Pecora *et al.* 1997). This is a form of diffusive coupling (as used in the introduction to this lecture), but it appears only in one of the equations.

The stability of this diffusively-coupled system is determined by the equation,

$$\frac{d}{dt}\begin{pmatrix} x_\perp \\ y_\perp \\ z_\perp \end{pmatrix} = \begin{pmatrix} -\alpha & -1 & -1 \\ 1 & a & 0 \\ z & 0 & x - c \end{pmatrix}\begin{pmatrix} x_\perp \\ y_\perp \\ z_\perp \end{pmatrix}, \tag{6.14}$$

where $x_\perp = x_1 - x_2$ and so on.

The leading transverse Lyapunov exponent is shown in figure 6.2 as a function of coupling strength α; where this is negative, the system is predicted to synchronize. As indicated by the figure, the synchronization manifold is unstable for small values of the coupling parameter α, but successful synchronization is achieved for intermediate values of α. This is perhaps not so surprising. More interestingly, we see that with stronger coupling, Λ becomes positive once more and the systems *desynchronize*.

In the limit of large α, the leading order balance in the equation for x_2 requires that $x_1 = x_2$. Thence,

$$\begin{aligned} \dot{x}_1 &= -(y_1 + z_1) \\ \dot{y}_1 &= x_1 + a y_1 \\ \dot{z}_1 &= b + z_1(x_1 - c) \\ \dot{y}_2 &= x_1 + a y_2 \\ \dot{z}_2 &= b + z_2(x_1 - c). \end{aligned} \tag{6.15}$$

In other words, the diffusive coupling is equivalent to complete replacement. Complete repacement of x in coupled Rossler systems is known not to be successful for synchronization at these parameter values. Hence, in this regard, the ultimate rise of Λ to positive values at larger α is expected.

Synchronization in coupled maps

In the two previous examples, the coupled system contained two elements with skew product structure; one system evolved independently of the other. Now we relax this constraint and

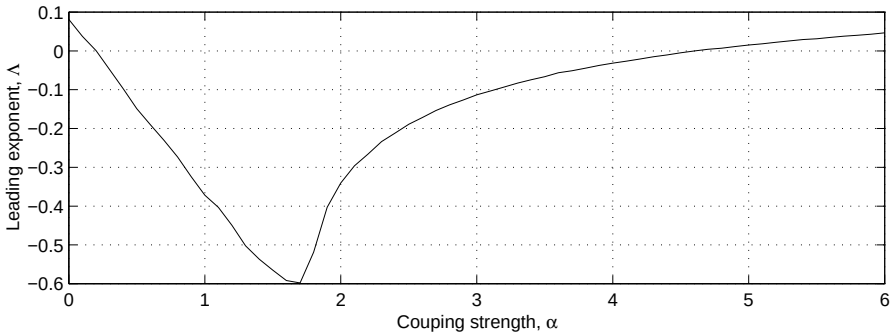

Figure 6.2: Strength of the leading transverse Lyapunov exponent Λ as a function of coupling strength parameter α for $a = 0.2$, $b = 0.2$ and $c = 9$.

consider a model with arbitrarily many elements that are coupled to either the whole ensemble (global coupling) or to two neighbouring elements (local coupling). Thus, we consider the global synchronization of a lattice. The particular model we choose is a coupled-map lattice which has been used by Kaneko and co-workers to explain many phenomena (Kaneko 1993).

The elements of the lattice are one-dimensional chaotic maps whose uncoupled form is $x_{n+1} = f(x_n)$. With *global coupling* of all the elements, the lattice equations become

$$x_{n+1}(i) = (1-\epsilon) f\left[x_n(i)\right] + \frac{\epsilon}{L} \sum_{j=1}^{L} f\left[x_n(j)\right], \tag{6.16}$$

where i and j are lattice indices, L is the number of elements in the lattice, and ϵ ($0 \leq \epsilon \leq 1$) is the coupling strength. This kind of model is considered in detail in Jacobson's report elsewhere in this volume.

For strong coupling, the chaotic lattice synchronizes globally (Kaneko, 1989; Ding & Yang, 1997). This is illustrated in figure 6.3 for a lattice described by $f(x) = 1 - ax^2$ (the logistic map again).

However, below a critical coupling strength, ϵ_c, the system desynchronizes. This threshold value depends on the largest Lyapunov exponent, λ, of the uncoupled map:

$$\epsilon_c = 1 - e^{-\lambda}. \tag{6.17}$$

For coupling values just under the critical threshold, the lattice displays on-off intermittent desynchronization (Fig 6.4).

One can also *locally* couple the map elements:

$$x_{n+1}(i) = (1-\epsilon) f\left[x_n(i)\right] + \frac{\epsilon}{2} \left(f\left[x_n(i-1)\right] + f\left[x_n(i+1)\right] \right). \tag{6.18}$$

This two-way, nearest-neighbour coupling is equivalent to a discretized diffusion across the lattice.

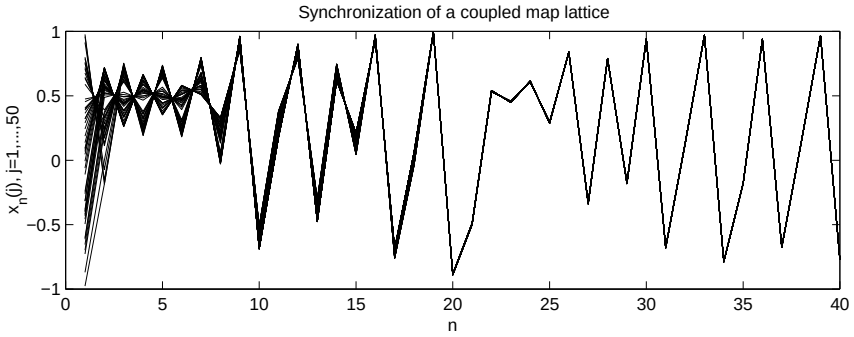

Figure 6.3: The synchronization of a globally coupled map lattice for $a = 1.9$ and $\epsilon = 0.5$ from random initial conditions lying in the range $[-1, 1]$.

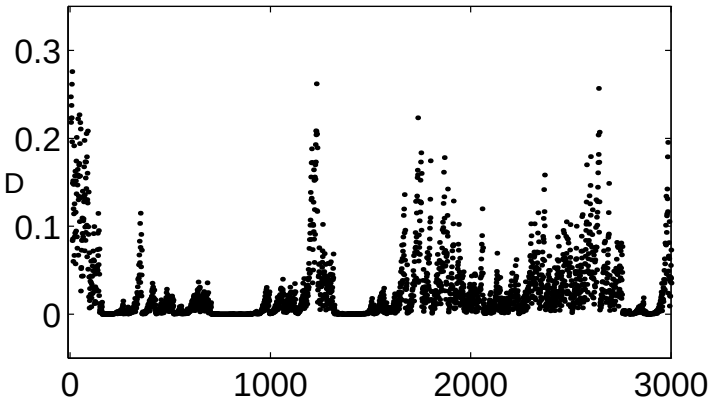

Figure 6.4: The value of $d = \frac{1}{L}\sum_{i=1}^{L} |x(i) - \bar{x}|$ as a function of n for 100 globally-coupled logistic maps with $a = 1.9$. The coupling parameter ϵ is 0.41, slightly less than $\epsilon_c = 0.43$.

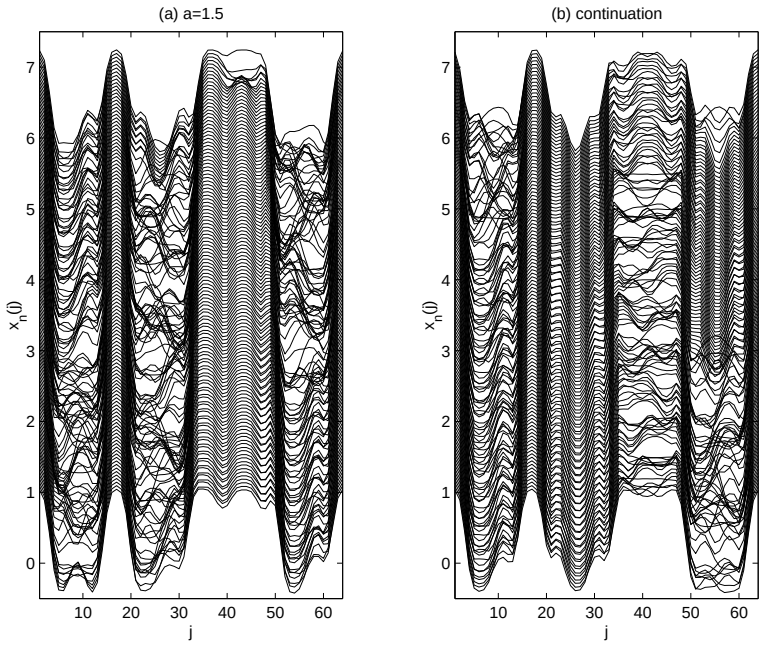

Figure 6.5: Evolution of a locally coupled map lattice for $a = 1.5$ and $\epsilon = 0.5$. Panel (b) is a continuation of (a).

In contrast to the global coupling case, the transverse Lyapunov exponents for local coupling are found to depend on the lattice size L. Synchronous chaos is only found in systems consisting of fewer than a critical number of elements L_m, with the maximum system size depending on the behavior of the individual map. Specifically, the leading transverse Lyapunov exponent can be shown to be

$$\Lambda = \lambda + \ln[1 - \epsilon + \epsilon \cos(2\pi/L)] \tag{6.19}$$

(Ding & Yang, 1997), which imples that the maximal lattice size is given by the largest integer $L < L_m$, where

$$L_m = 2\pi \left[\cos^{-1} \left(\frac{e^{-\lambda} - 1 + \epsilon}{\epsilon} \right) \right]^{-1} . \tag{6.20}$$

For example, when $a = 2$, $\lambda = \ln 2$ and the maximal system size is at most 6 (occuring for $\epsilon = 1$).

The origin of this limitation is that desynchronization sets in through a "long-wave" instability. Hence the only option for stable synchrony is to exclude the unstable range of wavenumbers by introducing a minimum wavenumber via the finite dimension of the lattice. When this is not possible, the coupled map lattice shows a wide range of spatio-temporal complexity as shown, for example, in figure 6.5 (see also Kaneko, 1993).

This figure shows anything but synchronization. But neither does it show a collection of chaotically evolving, independent elements. Instead there is a mixture of spatially local order

and confined regions of chaos. This is, of course, how one would like to imagine the spatially extensive natural systems that we deal with, which is why coupled map lattices and their relatives remain so popular.

A model of interhemispheric teleconnections

Finally, we turn to a GFD application of the synchronization theory (Duane, 1997). The meteorlogical basis of this model is an observed correlation between weather systems in the midlatitudes of the northern and southern hemispheres. Such correlations have been termed "teleconnections" by Bjerknes (1966). One of the important properties of such teleconnections is that they may be mediated by atmospheric Rossby waves. As a result, the connection between the hemispheric midlatitudes cannot be strong: Rossby waves propagating in midlatitudes, where winds are predominantly westerly, cannot traverse the equatorial regions because they become evanescent in regions of eastward flow (this can be understood from the linear dispersion relation of Rossby waves, see Duane's article). Nevertheless, the equatorial eastward winds are observed to be occasionally interrupted by localized weather patterns with internal, westward flow. Rossby waves then propagate through the narrow "ducts" that these patterns create, coupling the two midlatitudinal regions.

An important property of this coupling is that it takes a finite amount of time for the Rossby waves to propagate through the ducts. Thus one hemisphere does not immediately experience the effect of conditions in the other, but there is a delay.

We attempt to rationalize the correlation suggested by observations in terms of chaotic synchronization. We consider two Lorenz '63 systems $\{x, y, z\}$ and $\{x_1, y_1, z_1\}$ coupled through an auxiliary variable s:

$$\begin{aligned} \dot{x} &= \sigma(y - x) \\ \dot{y} &= r(x - s) - y - (x - s)z \\ \dot{z} &= -\beta z + (x - s)y \\ \dot{x}_1 &= \sigma(y_1 - x_1) \\ \dot{y}_1 &= r(x_1 + s) - y_1 - (x_1 + s)z_1 \\ \dot{z}_1 &= -\beta z_1 + (x_1 + s)y_1. \end{aligned} \tag{6.21}$$

If we select

$$s = c(x - x_1), \tag{6.22}$$

where c is the coupling strength ($0 \leq c \leq 1$), then the system (6.21) synchronizes. This simple model suggests that an explanation of this kind is possible. But (6.22) assumes that the coupling takes immediate effect.

One can generalize the model to allow a time lag in the coupling. In particular, one can replace (6.22) with the differential equation,

$$\dot{s} = \Gamma \left[-s + c(x - x_1) \right], \tag{6.23}$$

where Γ is the time scale on which s relaxes. In the limit of $\Gamma \to \infty$, one adiabatically eliminates s through the relation (6.22), and so the system reduces to the case above.

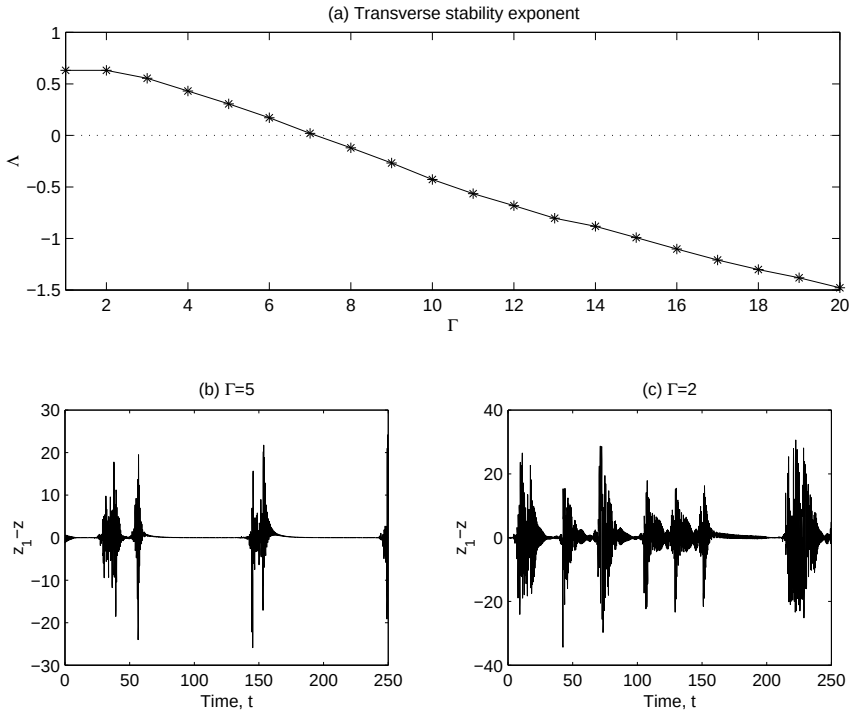

Figure 6.6: Synchronization of the coupled Lorenz systems (6.21) and (6.23). Panel (a) shows the transverse stability exponent against relaxation rate Γ. Panels (b) and (c) illustrate the intermittent synchronization that appears when the synchronization manifold loses stability, for $\Gamma = 5$ and $\Gamma = 2$ respectively. The other parameters are $c = 1$, $r = 28$, $\sigma = 10$ and $b = 8/3$.

For the more general situation using (6.23) with Γ finite, a range of synchronization results is found. For sufficiently large Γ, the systems still synchronize (as verified by a direct computation of the trasverse stability exponent, see figure 6.6), but as Γ is reduced, the stability of the synchronization manifold is lost. Instead, the system displays on-off intermittent desynchronization (figure 6.6, panels (b) and (c)). This sort of desynchronization is characterized by episodic bursts of wild departure from the synchronization manifold, after which the system returns to synchrony for some macroscopic length of time. This kind of behavior is the result of the synchronization manifold becoming slightly unstable as the time lag is increased. A trajectory of the coupled system may wander near or on the manifold for long periods of time before encountering conditions which cause it to desynchronize.

Though perfect synchrony can be lost for the time-lagged coupling, there remains a close correlation between the two subsystems as a result of the on-off intermittency. Duane observes similar effects in more complicated, though still relatively low-order, atmospheric models. In fact, the observed correlation between weather patterns at midlatitude in either hemisphere is far from precise (decribed further by Duane). But whether this reflects an origin that can be described by the on-off synchronization of two coupled, low-order systems is far from clear.

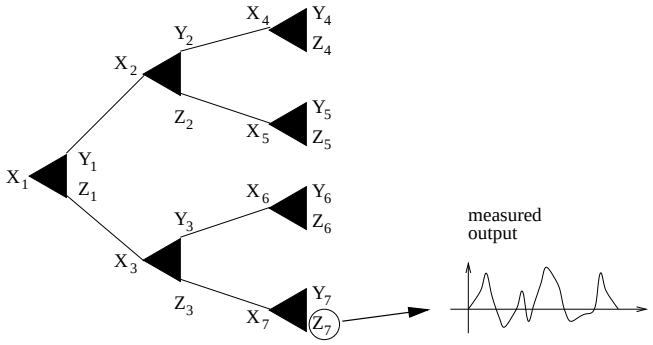

Figure 6.7: Coupling scheme for the seven Lorenz '84 systems.

6.2 Reconstructing the dynamics of coupled systems

We now turn to the issue of reconstruction. In particular, we ask the fundamental question of whether the dynamics of the full network can be inferred from a finite-length time series of just one variable from one subsystem. To answer the question we turn to metaphorics: we use a relatively simple network of coupled low-order dynamical systems to assess conventional reconstruction techniques.

We take a model proposed by Lorenz (1991; see also von Hardenberg *et al.*, 1997) . that consists of seven elements coupled through the network illustrated in figure 6.7. The coupling scheme represents some kind of cascade through subsystems of different scales, and can be extended to much larger systems. The cascade is meant to reflect some sort of analogy with turbulence (but it is clearly ludicrous to imagine that there is any real correspondence).

Each uncoupled element is a Lorenz '84 system, with parameters set such that individually each subsystem is chaotic. The equations of motion for the j^{th} system are

$$\left.\begin{array}{rcl} \dot{X}_j &=& -(Y_j^2 - Z_j^2) - a(X_j - F) + U_j \\ \dot{Y}_j &=& X_j(Y_j - bZ_j) - (Y_j - G) + V_j \\ \dot{Z}_j &=& X_j(bY_j + Z_j) - Z_j + W_j \end{array}\right\} \text{for } j = \{1, 2, \cdots, 7\}, \tag{6.24}$$

in which the coupling variables are

$$\left.\begin{array}{rcl} U_{2j} &=& -cY_j \\ U_{2j+1} &=& -cZ_j \\ V_j &=& c(X_{2j} - 1) \\ W_j &=& c(X_{2j+1} - 1) \end{array}\right\} \text{for } j = \{1, 2, 3\}, \tag{6.25}$$

and the parameters are set to $a = 0.25$, $b = 4$, $F = 8$ and $G = 1$. We allow the coupling strength, c, to vary.

Poincaré sections for three different values of c are shown in figure 6.8. For small coupling, the section looks similar to the uncoupled case. But as the coupling strength increases, the section becomes less reminiscent of a low-order dynamical system; the appearance becomes

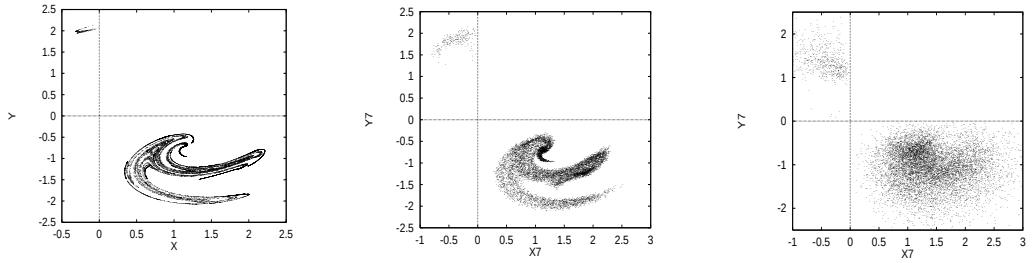

Figure 6.8: Poincaré maps in an X, Y plane for one member of the networked Lorenz systems of Fig. 6.7 and Eqs. (6.24) and (6.25). An isolated system ($c = 0$) is depicted in the left panel. In the middle panel, the systems are weakly coupled ($c = 0.1$). The right panel shows a map for strongly coupled systems ($c = 1.0$). Adapted from von Hardenberg (1996; *Thesis of Laurea*).

"noisier". This is presumably reflecting the fact that as we increase the coupling, the signal from each element becomes more characteristic of the entire system rather than an individual member. However, for low coupling strength, the signal from one of the subsystems has a strong, low-dimensional character and is relatively weakly influenced by the remainder of the high-dimensional network. This feature of the signal spells disaster for standard dimensional reconstruction techniques as we now illustrate.

The correlation dimension D_2 of one Lorenz '84 subsystem with these parameters values is estimated to be $D_2 \approx 2.19$. However, the coupled system has a dimensionality of something more like 15. We attempt to estimate this high dimensionality by taking the output from the seventh subsystem, $Z_7(t)$, as shown in figure 6.7. This signal provides synthetic data to test the reconstruction.

The standard time-embedding techniques using the time series of Z_7 lead to estimates of the correlation dimension as a function of the embedding dimension as shown in figure 6.9. This correlation dimension displays a slow convergence with embedding dimension and may seem to indicate rather lower values of D_2, especially for low coupling strengths ($D_2 \approx 5$ is suggested for $c = 0.1$); this is the effect of the superficial, low-dimensional character of the time series. This character masks the "jitter" due to the coupled network and hides the true dimensionality. The jitter actually leads to the very slow rise of D_2 beyond the initial levelling off. The correct conclusion to draw from figure 6.9 is that the computation simply does not converge.

This result implies that standard dimensional estimates may be misleading if the system in question is weakly coupled to other nonlinear systems. More specifically, one should exercise some care in interpretting the plots of D_2; the apparent convergence at low values is totally false, and the method simply fails to give an answer.

If we construct a signal using the output from more than one subsystem, the standard

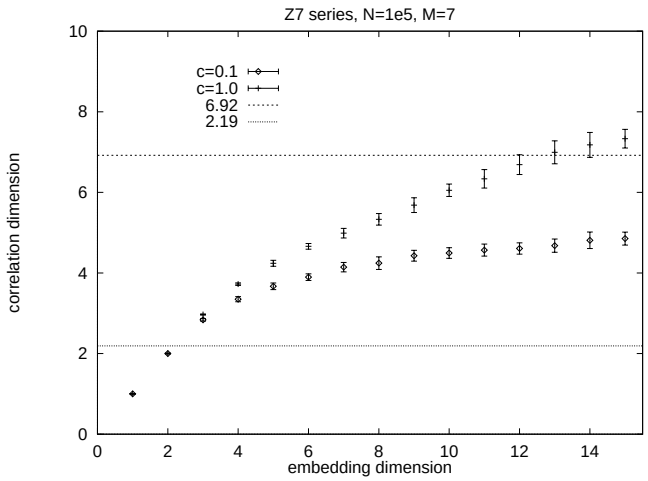

Figure 6.9: Correlation dimension estimates versus embedding dimension for the system (6.24),(6.25) with three values of the coupling coefficient c. The time delay is 0.025. Adapted from von Hardenberg (1996; *Thesis of Laurea*).

reconstruction techniques fare better. For example, if we use the signal $\sum_{l=1}^{7} Z_l(t)$ (*cf.* Lorenz, 1991), the estimated correlation dimension clearly shows no convergence as a function of embedding dimension over the range shown in figure 6.9. Hence, given more information about the network, it seems likely that we will not be deceived into hypothesizing the existence of low-dimensionality.

However, there is a serious problem in taking the reconstruction any further. Basically, the coupled system has so large a dimension that the time series that is actually needed to estimate D_2 is prohibitively long for any application or reasonable computation (as mentioned in lecture 3, we estimate that the length of time series needed for the current example is 2.5×10^{13} if the measurements are spaced apart by time intervals of 0.025, the delay used for the embedding in figure 6.9).

All this raises the question of how useful reconstruction really is. Clearly, for a complicated (possibly coupled) system, it is simply useless and prone to lead to spurious results. Some other method for exploring the underlying dynamics is evidently necessary.

Despite this failure, the structure of figure 6.9, with its two characteristic slopes separated by a "knee" is intriguing, and possibly conveys some information. Perhaps, as speculated by Lorenz, the shape can be used to measure some property of the inividual subsystem. But exactly what is not clear. Some systems consisting of many elements do show what one could describe as "extensive" properties: statistical measures such as correlation dimension scale approximately linearly with system size, suggesting that each subsystem can be described by a characteristic dimension. Perhaps this characteristic dimension can be extracted from figure 6.9 in some fashion.

6.2.1 Filtering a fast subsystem

Given the failure of reconstruction to estimate the correlation dimension, we consider it a bleak possibility that we might ever rebuild the structure of a complex system from a limited sampling of its dynamics. This calls for a change of perspective. The one we adopt is suggested by the arguments mentioned above, namely that in "extensive" systems, the subsystems are characterized by certain properties: Even though we cannot reconstruct the entire system, can we ignore most of its complicated components and instead determine the dynamics of a single subsystem?

This alternative approach has the advantage that, if successful, we can then "filter" out the most complicated ingredients of the problem (that we might never understand anyway), and focus on the pieces that might elementally control the phenomenon in question. Indeed, a frequently encountered feature of natural systems is variability on multiple timescales, with the fastest timescales corresponding to turbulence. Yet we commonly believe that it is the slower (or longer) scales that describe the essential features of many geophysical and astrophysical phenomena, with turbulence playing a more minor role (such as providing the source of damping via energy cascade to the dissipation scale). Can we isolate these slower scales and understand them independently of the turbulence?

A partial answer to this question comes from looking at a simple system consisting of two coupled elements with different timescales. In particular, by using tools such as the "finite-size" Lyapunov exponent, we can estimate some properties of the slow subsystem even if the faster subsystem is not resolved or stochastic (Boffetta *et al.* 1998).

Finite-Size Lyapunov Exponents (FSLE)

We define the finite-size Lyapunov exponent (Aurell *et al.* 1996) in terms of the growth of a finite error in a trajectory lying on the attractor of the system. Let $T_r(\delta)$ denote the time taken for an error with initial size δ to grow to a size $r\delta$. For example, $T_2(\delta)$ is the "error-doubling time" if we start with error δ. Then, the FSLE is given as

$$\lambda(\delta) = \frac{1}{\langle T_r(\delta) \rangle} \ln r, \tag{6.26}$$

where the angular brackets denote an ensemble average over many realizations.

Evidently, when $\delta \to 0$ and the initial error becomes infinitesimal, $\lambda(\delta) \to \lambda_{max}$, the leading, conventional Lyapuonv exponent. But as δ becomes large, the error becomes comparable to the size of the attractor itself. At this stage, the error can no longer continue to amplify exponentially; it becomes constrained by the attractor's geometry. Thus we expect the finite-size Lyapunov exponent to behave in the manner illustrated in figure 6.2.1.

In practice, the exponent is computed by taking two systems that in phase space are initially δ apart, and evolving them foward in time until the difference between them exceeds $r\delta$. This introduces a further technicality concerning the *direction* of the initial error, and not just its size, δ. If we begin from some arbitrary finite error in the initial point in phase space, then there is also an immediate convergence to the attractor. But the finite-size Lyapunov exponent is a measure of error growth on the attractor itself, and so the initial relaxation

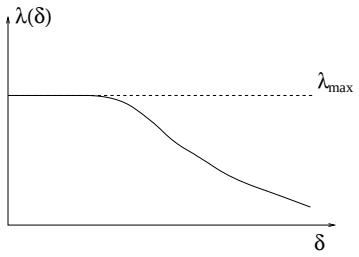

Figure 6.10: The FSLE as a function of δ

should be filtered out somehow. This amounts to taking the initial error to be aligned with the most unstable direction. Practically, we begin the computation of the two orbits from an error of size $\delta_{min} \ll \delta$, and then begin the construction of $\lambda(\delta)$ once the error amplifies through δ. Provided the relaxation to the attractor is sufficiently rapid, δ is then aligned as required.

Coupled maps

We illustrate the finite-size Lyapunov exponents using a pair of coupled maps:

$$\begin{aligned} x_s(n+1) &= (1-\epsilon) f_s(x_s) + \epsilon g[x_s, x_f] \mod 1 && (6.27)\\ x_f(n+1) &= (1-\epsilon) f_f(x_f) + \epsilon g[x_s, x_f] \mod 1 && (6.28)\\ f_s &= e^{\lambda_s} x_s \mod 1 \\ f_f &= e^{\lambda_f} x_f \mod 1 \\ g &= \cos[2\pi(x_s + x_f)]. && (6.29) \end{aligned}$$

Two sample orbits to this system, starting from nearby initial conditions, are shown in figure 6.11.

We compute two trajectories for these maps from an initial condition of $\delta(1) = \delta_{min} = 10^{-9}$. This generates a sequences of growing errors, $\delta(1) \to \delta(2) \to \delta(3)...$, from which locate values of δ and $r\delta$, then read off their integral temporal separation. The ensemble average of repeated computations of this kind then provides the data needed to compute $\lambda(\delta)$. An example of $\lambda(\delta)$ is shown in figure 6.12.

For small δ, the exponent falls close to the Lyapunov exponent of the fast subsystem, λ_f. Evidently, the doubling of a small error is controlled by the fast subsystem. However, for larger errors, the exponent converges to values nearer the Lyapunov exponent of the slow subsystem, λ_s. This reflects the dominance of the slow dynamics in controlling the larger error growth. There is a natural explanation of this effect: as δ grows from the original, initial error, δ_{min}, the slow subsystem barely evolves over the periods over which small errors amplify. Hence the error grows mainly due to the effect of the chaotic dynamics of the fast subsystem. Eventually, however, the error in the fast subsystem reaches a maximum due to geometrical constraints. At this stage, the growth of the error becomes dominated by the slower growth of the other subsystem.

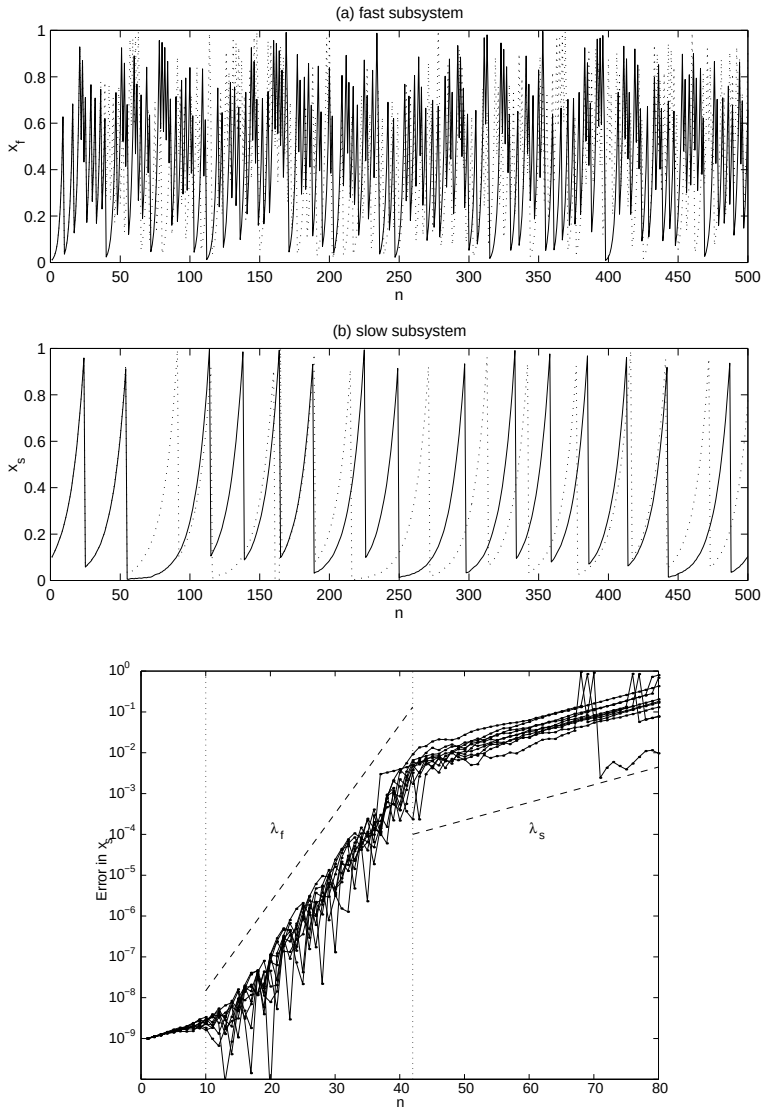

Figure 6.11: Time series of (a) x_f and (b) x_s for the coupled maps (6.27)-(6.29). In panel (c) we show the growth of an error of 10^{-9} for ten realizations of the system. The error growth is divided into three regimes; for $n < 10$, there is an initial relaxation onto the attractor. For $10 < n < 42$ the error grows roughly exponentially with the larger Lyapunov exponent, λ_f. Finally, for $n > 42$, the error develops according to the slow dynamics with exponent λ_s.

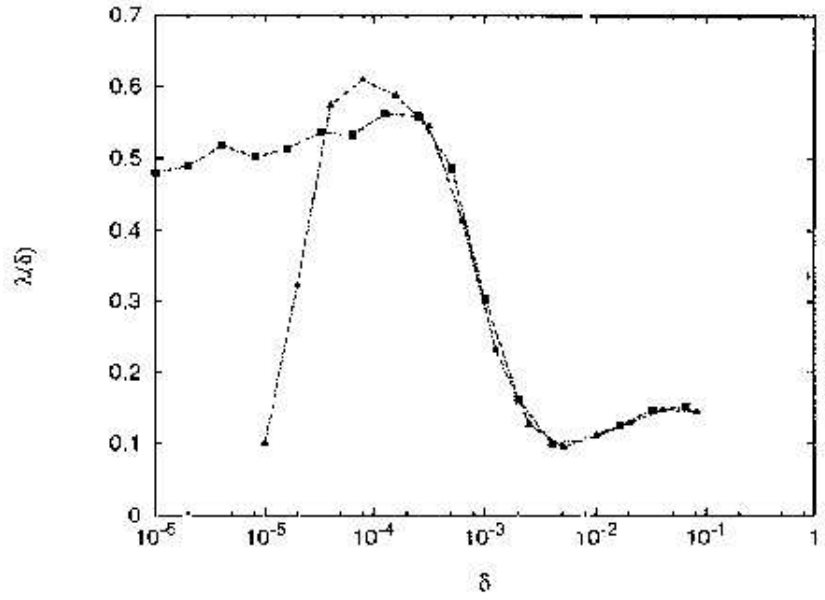

Figure 6.12: FSLE as a function of δ for the coupled maps (6.27)-(6.29), with $r = 2$, $\lambda_s = 0.1$ and $\lambda_f = 0.5$, and $\epsilon = 2 \times 10^{-3}$. Errors are measured in terms of the differences in x_s between two solutions, and 10^4 realizations were used to compute the ensemble average of $T_2(\delta)$. Note that the system is driven by the fast subsystem for small values of δ and by the slow subsystem for larger values. The case shown by triangles indicates the results if the initial perturbation is not aligned with the unstable direction; that is, if $\delta_1 = 10^{-5}$, the smallest value of δ for which we plot λ. (Adapted from Boffetta *et al.* 1998.)

The effect is illustrated in panel (c) of figure 6.11, which shows error development for ten realizations of the coupled system. The initial relaxation to the attractor is evident for $n < 10$. Subsequently, the error amplifies roughly exponentially, first with the Lyapunov exponent of the fast subsystem, and then with that of the slow subsystem.

Also shown in Fig. 6.12 are results computed by taking initial perturbations that were not aligned with the unstable direction. This gives a qualitatively different graph in which the convergence to λ_f at small δ is not apparent. Here, then, the relaxation from the initial condition masks the error growth due to the fast subsystem.

Nevertheless, in both cases shown in the figure, the large-error growth is dominated by the dynamics of the slow subsystem and this can be extracted easily from the results. This gives us hope that we can, with suitable technology, filter the fast subsystem, and measure quantities such as λ_s directly. However, from an experimental perspective, the extraction of information pertaining to the fast subsystem is probably impossible: it is unlikely that under experimental conditions we can resolve the growth of a small error, even if we could unmask the small$-\delta$ behaviour of $\lambda(\delta)$ from the obscuration due to intial relaxation.

The situation becomes even worse when the fast subsystem has high dimension. We illustrate this in figure 6.13 which shows the results for $\lambda(\delta)$ when we replace the fast subsystem in (6.28) by stochastic noise. For the stochastically forced system, the exponent rises to ever higher values as we lower δ. At larger error, however, we still observe the dominance of the slow system and can again measure λ_s.

Computing the FSLE from a Time Series

Experimentally, we do not have access to the equations or solutions from controlled initial conditions. Instead, we must measure some characteristic quantity and build a phase space through an embedding procedure. Then we can attempt to construct finite-size Lyapunov exponents by finding segments of the time series in which the system passes through the same neighbourhood of phase space. That is, we locate two portions of the trajectory that fall close to each other. These segments are analogous to solutions with close-by initial conditions, and we may then define error growth from the differences in the subsequent evolution.

By way of illustration, consider the coupled Lorenz equations,

$$\dot{x_s} = -\sigma(x_s - y_s) \tag{6.30}$$
$$\dot{y_s} = -x_s y_s + (r + \epsilon z_f)x_s - y_s \tag{6.31}$$
$$\dot{z_s} = x_s y_s - b z_s \tag{6.32}$$

and

$$\dot{x_f} = -a\sigma(x_f - y_f) \tag{6.33}$$
$$\dot{y_f} = a(-x_f y_f + r x_f - y_f) \tag{6.34}$$
$$\dot{z_f} = a(x_f y_f - b z_f). \tag{6.35}$$

Thus the fast subsystem acts to perturb the Rayleigh number of the slow subsystem, much as one might envision experimental noise or small-scale turbulence.

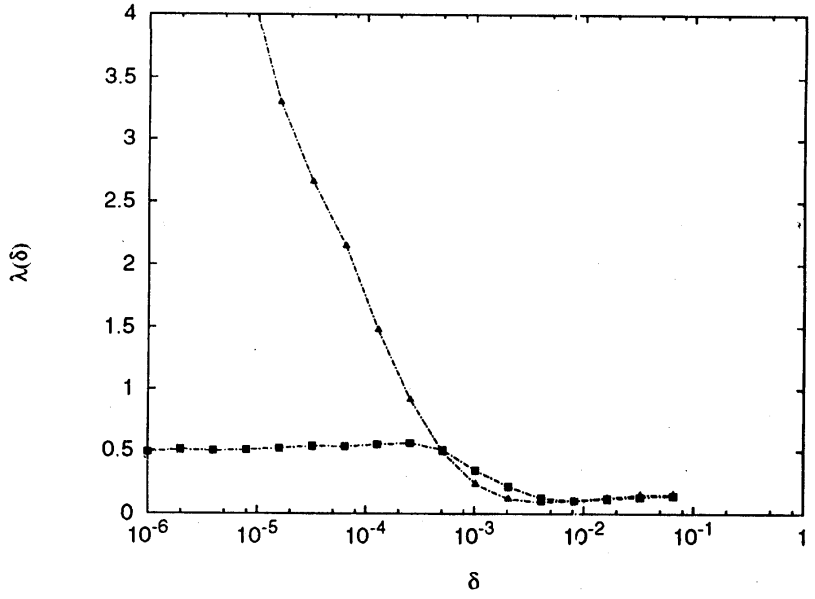

Figure 6.13: Finite-size Lyapunov exponents for the map (6.27) with x_f a random variable uniformly distributed in [0,1] (shown by filled triangles). Again, $r = 2$, $\lambda_s = 0.1$, and $\epsilon = 2 \times 10^{-3}$. Errors are measured in terms of the differences in x_s between two solutions, and 10^4 realizations were used to compute the ensemble average of $T_2(\delta)$. For comparison, the filled squares show the computation for the deterministic version of the system. (Adapted from Boffetta *et al.* 1998.)

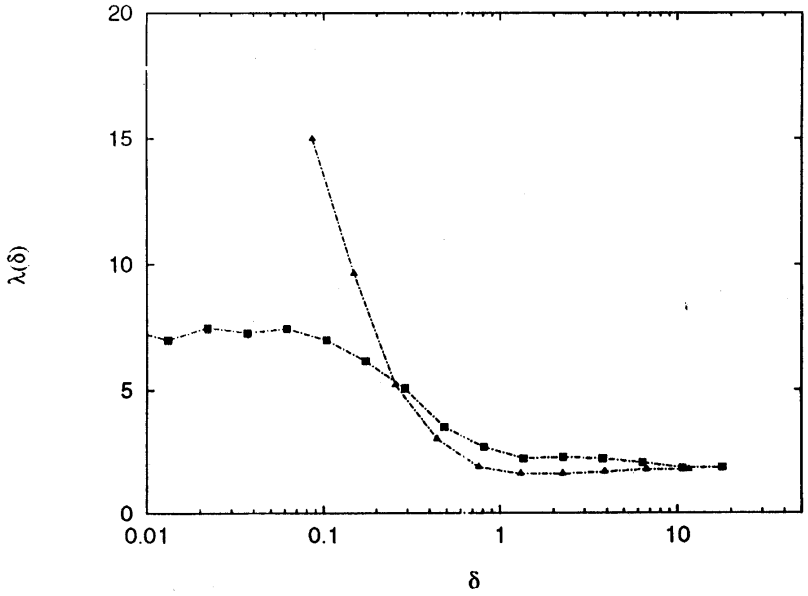

Figure 6.14: The FSLE as a function of δ obtained from the time series for the coupled Lorenz system with $\epsilon = 0.05$, $r = 45.92$, $\sigma = 16$ and $b = 4$. The parameter $a = 5$ and so $\lambda_s \approx 1.5$ and $\lambda_f = 5\lambda_s \approx 7.5$. The filled triangles show results for a three dimensional embedding with time delay of 0.02 and 5×10^5 points. The filled squares show the result from directly computing the exponent from initial-value solutions to the equations. (Adapted from Boffetta *et al.* 1998.)

The factor of a on the right-hand side of (6.33)-(6.35) can be removed on rescaling time in those equations, in which case we recover the Lorenz model for the fast subsytem. Thus, given the Lyapunov exponent of the Lorenz model, λ_s (which is also the exponent for the uncoupled slow subsystem), we can immediately read off the fast subsystem's exponent: $\lambda_f = a\lambda_s$.

We now evolve the system and generate synthetic data from the output of the slow subsystem. With the usual embedding procedures and the identification of segments of the time series that can be used to monitor error growth, we compute the finite-size Lyapunov exponents shown in figure 6.14. Also shown is the exponent computed directly from solutions to the equations.

Because the experimental procedure necessarily involves an embedding, the results for $\lambda(\delta)$ depend on the dimension of the embedding space, M. Importantly, as shown in figure 6.14, we appear to be able to resolve the convergence to λ_s once the embedding dimension exceeds that of the slow subsystem. From a practical perspective, this suggests that the procedure is useful.

There is also some suggestion that $\lambda(\delta)$ converges to λ_f at small δ, when the embedding space is as large as that of the full system (in figure 6.14, the emdebbing space is too small to observe convergence at small δ). But this again is obscured by our inability to aligne δ

with the direction of maximum error growth. And if the fast system is of high dimension, it is unlikely that time series will ever be of sufficient length to achieve this convergence. Hence this facet of the construction is not that useful.

6.3 Prediction and the utility of FSLEs

If we knew all of the properties of a system at a particular instant, then we could, in principle, evolve the system forwards in time and determine its state at any future moment. Practically, however, we do not know every detail of a system and our computations are imprecise. This means that there is always an uncertainty in the initial position of our system, be it either from our ignorance or our impecision. This uncertainty constitutes an error in following the system that amplifies and eventually wrecks our prediction of the future state. In other words, predictability is determined by the initial uncertainty and how this error grows.

For chaotic systems, we measure predictability in terms of a "prediction time", $t_\sigma(\delta)$, that depends on the initial error, δ, and a tolerance, σ, that we allow in the observations. From our definition (6.26), we estimate

$$t_\sigma = \frac{1}{\lambda(\delta)} \ln \frac{\sigma}{\delta}, \tag{6.36}$$

with $r = \sigma/\delta$. Therefore, the finite-size Lyapunov exponents can be interpreted alternatively as giving the prediction time.

Previously, some studies used the leading, conventional Lyapunov exponent in place of $\lambda(\delta)$ in the estimate of the prediction time in (6.36). However, the usual Lyapunov exponent measures the growth rate of an error averaged over all time, or equivalently over the whole of the attractor. But the development of an error varies significantly over the attractor and therefore at different instants in time (in fact, errors can still magnify even for systems with negative Lyapunov exponents). Consequently, the conventional Lyapunov exponent is not always very useful in estimating the predictability time; it is more naturally determines by the finite-size exponents.

These remarks were essentially made by Lorenz (1996) in the context of predictability of

atmospheric motions. Lorenz used the model equations,

$$\frac{dX_k}{dt} = -X_{k-1}\left(X_{k-2} - X_{k+1}\right) - X_k - \frac{hc}{b}\sum_{j=1}^{J} Y_{j,k} \tag{6.37}$$

$$\frac{dY_{j,k}}{dt} = -cbY_{j+1,k}\left(Y_{j+2,k} - Y_{j+1,k}\right) - cY_{j,k} + \frac{hc}{b}X_k \tag{6.38}$$

with

$$\begin{aligned} k &= 1, \ldots, K \\ j &= 1, \ldots, J \\ X_{k-K} &= x_{k+K} = X_k \\ Y_{j-J,k} &= Y_{j,k-1} \\ Y_{j+J,k} &= Y_{j,k+1}, \end{aligned}$$

where h, c and b are all parameters. Rough meaning is given to the variables in these equations by identifying the index k as referring to a set of longitudinal sectors at a given latitude, and j as reflecting a finer subdivision of each sector. Thus, the quantities X_k refer to some slowly varying atmospheric quantity, whilst the variables $Y_{j,k}$ represent some small-scale fields.

The growth of errors in the system (6.37)-(6.38) follows a pattern much like the coupled maps or Lorenz systems used above: the growth of a small error is dominated by the fast dynamics of the small-scale subsystems; larger error development is controlled by the large-scale subsystems.

Lorenz likened the dynamics of this coupled system to more complicated models of atmospheric phenomena such as the El Nino Soutern Oscillation (ENSO). The role of the slow system is played by the upper layer of the ocean, as X_k models sea-surface temperature; this responds rather slowly to atmospheric forcing due to the ocean's high heat capacity. But the atmospheric weather systems that migrate overhead, and which constitute the other part of the coupled climate system, vary much more quickly and on shorter scales; these are the fast subsystems.

The important feature of the coupled system is that the large-error growth, being dominated by slow dynamics, is relatively mild. Thus, although the prediction time of the atmospheric systems may be very short, there is some hope for predictability of the slower subsystems. ENSO itself is often characterized by sea surface temperatures, and models that attempt to predict the onset of these events exploit that data. Thus part of the success of those models may hinge on the predictability of the slow scales. Essentially, what may happen is that the atmospheric weather patterns are filtered out; they influence the dynamics of the large scales only through a weakly coupled, random forcing.

Lecture 7

Coherent Structures

Until now, we have discussed aspects of the dynamics of low-dimensional deterministic systems, extending our understanding to coupled and forced models. Chaotic behavior, unpredictability and bifurcations have been some of our companions in the journey.

Another crucial issue in nonlinear dynamics, that has been discarded until now, concerns the formation of "order," or of "structures," from the disordered background filling the universe. Why individual, ordered structures exist, is not a trivial question. It is so nontrivial, that nobody really knows the answer. Although some people - from time to time - have claimed to have discovered the deep truth underlying the formation of coherent patterns, no fully satisfactory answer to this question is available. For example, it is not even clear whether there are a few universal mechanisms of pattern formation, that are active in different systems. Or whether every specific case is different from any other, and each mechanism has its individuality and does not play any role in other context. Nonetheless, the issue of pattern formation is perhaps one of the deepest, and the one that touches us most directly in all science. After all, we are coherent patterns ourselves (at least sometimes), possessing the curious attitude to order our perceptions of the world around us, and to try to order and control the world itself...

7.1 Types of coherent structures

In nature, there are several different types of coherent patterns. For example, mechanisms of pattern formation are present in many reaction-diffusion systems (see the lecture notes by Fauve in a previous GFD volume for a thorough discussion of this issue).

Here, we are concerned with simple coherent structures that are present in fluid systems, such as rapidly rotating fluids and magnetofluids. In this context, a coherent structure is a localized, individual fluid state that persists for times much longer than a local dynamical time (to be properly defined). Often, these coherent structures are associated with the presence of an external ordering field, that makes the system anisotropic and induces an inverse cascade (from small to large scales) of some relevant dynamical quantities. The structures that form are often stationary solutions of the equations governing the system dynamics, and they usually live as localized entities emerging from a turbulent background.

Some examples of such coherent structures are:

- Localized nonlinear waves (e.g. solitons) arising from equations like the Korteweg-de-Vries equation, $\eta_t + c\eta_x + a\eta\eta_x + b\eta_{xxx} = 0$, or the sine-Gordon equation, $\phi_{tt} - c\phi_{xx} = a \sin\phi$. Here, subscripts indicate partial derivatives.

- Coherent jets, that are formed either as free fluid streams (e.g., the jet stream in the high atmosphere), or as boundary currents due to the presence of differential rotation and rigid boundaries (e.g., the Gulf Stream).

- Coherent vortices, which form spontaneously in rotating turbulent flows, and contain most of the energy and circulation of the system.

- Coherent flux tubes, which emerge as coherent concentrations of current in anisotropic magnetohydrodynamical flows.

This lecture and the following one are devoted to the discussion of coherent vortices and flux tubes. Coherent vortices are spectacular entities whose presence is revealed in any turbulent fluid flow that is subject to strong rotation, or in any conducting fluid immersed in an external magnetic field. Geophysical and astrophysical examples of energetic coherent vortices include the Great Red Spot on Jupiter, and similar spots on other giant gaseous planets; Gulf Stream rings arising from meandering instabilities of that jet; Meddies, mesoscale Mediterranean eddies generated by the instability of the salty outflow from the Mediterranean Sea into the Atlantic Ocean; atmospheric blocking, a big coherent vortex bound to the topography; mid-latitude atmospheric cyclones; the winter stratospheric polar vortex; "plasmoids" generated in the magnetopause of the Earth; galaxies in the intergalactic turbulence and star systems in interstellar space; starspots, coherent magnetic flux tubes whose best-known example is provided by Sunspots; and, possibly, coherent vortices on accretion disks.

7.2 The quasi-geostrophic approximation

To be specific, and stay simple, we study the dynamics of coherent vortices in the framework of the quasi-geostrophic (QG) approximation for a barotropic fluid. This approximation provides a simplified description of large scale oceanic flows and of shallow-layer atmospheric motions, provided nonadiabatic effects and baroclinicity can be neglected.

To derive the barotropic QG approximation, we first discuss the standard shallow-water system (for a thorough derivation see Pedlosky 1987). Call H the average vertical extent of the fluid layer, and L a typical horizontal scale of motion. For large-scale geophysical flows, H is usually much smaller than L, as the thickness of the dynamically active fluid layer is at most a few kilometers while the horizontal size of motion may reach hundreds or thousands of kilometers. In fact, we can define "large-scale" flows as those for which $\delta = H/L \ll 1$.

In the limit of $\delta \to 0$, for a layer of constant density ρ, the *shallow-water approximation* can be introduced. This approximation assumes hydrostatic support in the vertical direction

and then explicitly factors out the dependence on z. The equations of motion then become

$$\frac{\partial u}{\partial t} + u\frac{\partial u}{\partial x} + v\frac{\partial u}{\partial y} - fv = -g\frac{\partial \eta}{\partial x}, \tag{7.1}$$

$$\frac{\partial v}{\partial t} + u\frac{\partial v}{\partial x} + v\frac{\partial v}{\partial y} + fu = -g\frac{\partial \eta}{\partial y}, \tag{7.2}$$

$$p = \rho g(h - z) + p_0 \tag{7.3}$$

and

$$w = (h_0 - z)\left(\frac{\partial u}{\partial x} + \frac{\partial v}{\partial y}\right) + u\frac{\partial h_0}{\partial x} + v\frac{\partial h_0}{\partial y}, \tag{7.4}$$

where $\mathbf{v} = (u, v, w)$ is velocity, p is pressure, g is the acceleration of gravity, and f is the Coriolis parameter. Also, $\eta(x, y, t)$ is the free surface, and $h_0(x, y)$ describes the topography of the bottom.

The shallow-water potential vorticity is defined as

$$q_{sw} = \frac{\omega + f}{h}, \tag{7.5}$$

where $\omega = v_x - u_y$ is the relative vorticity, and $h = H + \eta - h_0$ is the total layer depth. The potential vorticity q_{sw} is conserved in the absence of forcing and dissipation:

$$\frac{D}{Dt}\left(\frac{\omega + f}{h}\right) = 0, \tag{7.6}$$

where D/Dt is the material (Lagrangian) derivative.

In the limit of strong rotation, circulations at the Coriolis frequency are faster than any other motions in the system and $f \ll U/L$. Hence the Rossby number $\epsilon = U/fL \ll 1$ (U being a velocity scale). The shallow water equations can then be expanded in powers of ϵ. This produces the quasi-geostrophic approximation and corresponds to filtering the fast modes of the system (gravity waves).

We expand the shallow-water expression for potential vorticity and keep only terms of $O(\epsilon)$:

$$q' = \omega' - \frac{\eta'}{R^2} + h_0', \tag{7.7}$$

where the primed variables are dimensionless (e.g., $\omega = U\omega'/L$). Here $R^2 = (L_R/L)^2$, where $L_R = \sqrt{gH}/f$ is the barotropic Rossby radius of deformation. Furthermore, we assumed $h_0' = h_0/H$ to be of the order of the Rossby number.

To a similar order of approximation, the expression for D/Dt becomes $D/Dt = \partial/\partial t + \mathbf{u}\cdot\nabla$ where $\mathbf{u}$ is the shallow-water geostrophic velocity, and is given by $\mathbf{u} = (-\partial\psi/\partial y, \partial\psi/\partial x)$. The geostrophic stream-function ψ is related to the free-surface elevation η by

$$\psi = \frac{\eta g}{f}, \tag{7.8}$$

which in dimensionless form becomes $\psi' = \eta'$. Hence, the potential vorticity q' can be expressed as

$$q' = \nabla^2\psi' - \frac{\psi'}{R^2} + h_0{}'. \tag{7.9}$$

Then conservation of potential vorticity in the (barotropic) QG approximation can be stated as:

$$\frac{\partial q'}{\partial t} + [\psi', q'] = 0 \tag{7.10}$$

where $[A, B]$ is the Jacobian operator $A_x B_y - A_y B_x$.

In the above discussion, we have considered the Coriolis parameter f to be constant. But this frequency actually varies with latitude. On a spherical planet, the local value of the Coriolis parameter is $f = 2\Omega \sin\phi$ where Ω is the rotation rate of the system and ϕ is the local latitude. If we consider motions which do not extend over a broad range of latitudes, then it is justified to take a reference value for ϕ (say, ϕ_0) and to take $f = f_0 = 2\Omega \sin\phi_0$ as a constant. For motions with large scale meridional extent, however, the variation of the Coriolis parameter with latitude can no longer be discarded. The first order approximation used to correct for this effect is the so-called "beta-plane" approximation. By Taylor-expanding f and keeping only the first order term, one obtains

$$f = 2\Omega \sin\phi_0 + 2\Omega \cos\phi_0(\phi - \phi_0) = f_0 + \beta y \tag{7.11}$$

with $\beta = 2\Omega \cos\phi_0/R_e$ and $y = R_e(\phi - \phi_0)$. Here R_e is the radius of the Earth.

In the quasi-geostrophic approximation it is assumed that $\beta \ll f_0/L$. More specifically, the dimensionless β parameter, defined as $\beta' = \beta L^2/U$, is assumed to be of the order of the Rossby number. One can then rewrite the potential vorticity as $q' = \nabla^2\psi' - \psi'/R^2 + \beta' y' + h_0{}'$. The conservation of potential vorticity reads (for convenience, from now on we skip the primes)

$$\frac{\partial}{\partial t}\left(\nabla^2\psi - \frac{\psi}{R^2}\right) + [\psi, \nabla^2\psi + h_0] + \beta\frac{\partial\psi}{\partial x} = 0. \tag{7.12}$$

If there is neither topography ($h_0 = 0$), beta-effect ($\beta = 0$, also called the f-plane), nor free surface ($L << L_R$, i.e. $\frac{1}{R^2} \to 0$) the QG equation reduces to the two-dimensional Euler equation,

$$\frac{\partial}{\partial t}\nabla^2\psi + [\psi, \nabla^2\psi] = 0. \tag{7.13}$$

We organize our discussion of coherent structures by first considering the dynamics of turbulence in the dissipative version of the two-dimensional Euler equation. Then we continue on to describe the modifications introduced when we deal with the added ingredients in the QG approximation. The discussion spans two lectures.

7.3 2D Turbulence

The two-dimensional Euler equations admit an infinite number of conserved quantities. Two quadratic invariants that are of particular importance are the kinetic energy,

$$E = 1/2 \int (\nabla\psi)^2 dxdy, \tag{7.14}$$

and the enstrophy,

$$Z = 1/2 \int (\nabla^2 \psi)^2 dx dy \ . \tag{7.15}$$

The Euler equations are non-dissipative (i.e., conservative). In most systems, however, dissipation is present, and to be consistent with a dissipative world we have to include this physics in the QG approximation. The standard form is a Newtonian dissipation term, $D_N = \nu \nabla^2 \omega$, that is added to the right-hand-side of the Euler equation. Alternatively, Rayleigh friction takes the form $D_R = -K\omega$ (this represents, for example, bottom friction). *Hyperviscosity* provides a general expression for dissipation, $D_s = (-1)^{s-1} \nu_s \nabla^{2s} \omega$, and includes both the standard Newtonian case ($s = 1$) and Rayleigh friction ($s = 0$). In numerical simulations, a hyperviscous dissipation with $s > 1$ is often used. This approach, although artificial, attempts to confine the effects of dissipation to very small scales, and so allows us to reach higher values of the (equivalent) Reynolds number.

The equations for freely-decaying (i.e., dissipated but not forced) 2D turbulence then read

$$\frac{\partial}{\partial t} \nabla^2 \psi + [\psi, \nabla^2 \psi] = (-1)^{s-1} \nu_s \nabla^{2s} \nabla^2 \psi. \tag{7.16}$$

For this version of the problem, energy and enstrophy are are no longer exactly conserved, but they are almost so for sufficiently small viscosity. (In fact, one may show that the energy dissipation vanishes in the limit for $\nu \to 0$; for this reason, energy is sometimes called a "rugged invariant" of the system.)

The approximate conservation of energy and enstrophy in two-dimensional, nearly inviscid systems has some important consequences, which are best appreciated in the comparison with 3D turbulence.

In nearly inviscid three-dimensional turbulence, energy is the only approximate invariant, which we may write as

$$E = \int \mathcal{E}(k) dk, \tag{7.17}$$

where $\mathcal{E}(k)$ is the spectral energy density. The image of 3D turbulence is then associated with the celebrated "cascade" of energy to small length scales; energy injected into the system at long wavelengths becomes channeled down to small wavelengths by nonlinear interactions. Thus, the large "energy-bearing eddies" feed motions of increasing fine scale until energy is ultimately dissipated on the "dissipation scale". The range of motion between these two limits is the "inertial range". For isotropic turbulence, one finds that $\mathcal{E} \sim k^{-5/3}$ in the *Kolmogorov scaling* suitable for the inertial range.

In two dimensions, on the other hand, enstrophy is also approximately conserved, and it may be written as

$$Z = \int \mathcal{Z}(k) dk = \int k^2 \mathcal{E}(k) dk. \tag{7.18}$$

Now, consider a fluid element of scale k_0 transfering energy and enstrophy into the scales k_1 and k_2 (see figure 7.1). Energy and enstrophy conservation require that

$$\mathcal{E}(k_0) = \mathcal{E}(k_1) + \mathcal{E}(k_2) \qquad \text{and} \qquad k_0^2 \mathcal{E}(k_0) = k_1^2 \mathcal{E}(k_1) + k_2^2 \mathcal{E}(k_2). \tag{7.19}$$

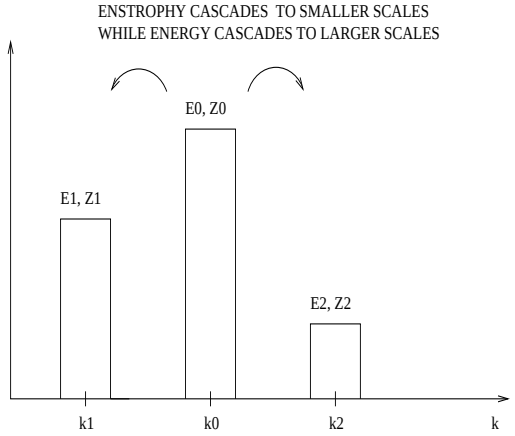

Figure 7.1: Energy and Enstrophy Cascades in 2D Turbulence

Thus

$$\mathcal{E}(k_1) = \frac{k_2^2 - k_0^2}{k_0^2 - k_1^2}\mathcal{E}(k_2). \tag{7.20}$$

For example, if $k_1 = k_0/2$ and $k_2 = 2k_0$, then we observe that $\mathcal{E}(k_1) = 4\mathcal{E}(k_2)$. In other words, more energy is transfered to larger scales than to smaller ones. But similar arguments indicate that $\mathcal{Z}_1 \equiv k_1^2\mathcal{E}(k_1) = k_2^2\mathcal{E}(k_2)/4 = \mathcal{Z}_2/4$, and so enstrophy is channeled primarily in the opposite direction.

Thus, the simultaneous conservation of energy and enstrophy induces a "direct" cascade (i.e., from large to small scales) of enstrophy and an "inverse" cascade (from small to large scales) of kinetic energy (see e.g. Kraichnan & Montgomery 1980). This suggests that in a two-dimensional fluid (or, a fluid which is subject to strong rotation), larger and larger structure forms, in association with the flow of energy to small wavenumbers. Indeed, numerical simulation and laboratory experiments have revealed the formation of strong, long-lived vortices that contain most of the energy and the enstrophy of the system and live much longer than typical circulation times (defined, for example, as the typical rotation time of a particle inside a vortex). The qualitative appearance of 2D turbulence is thus a random, low-energy background turbulent field intermittently punctuated by strong individual vortices (McWilliams 1984 and 1990).

Simulation and experiments have also offered us a picture of the typical evolution of freely-decaying 2D turbulence. Beginning from a random vorticity field (with energy localized over a narrow band in wavenumber) there is a brief phase of strong energy dissipation, followed by a period of vortex generation, during which small vortices are generated by the inverse cascade. After the first burst of vortex formation, the dynamics becomes characterized by vortex-vortex

interactions. Three significant types of interaction occur: long-range interactions between well-separated, isolated vortices (that can be approximately modelled by systems of point vortices), temporary dipolar pairing between neighbouring vortices of opposite sign, and strong inelastic interactions between closely spaced vortices of the same sign. The inelastic interaction between vortices of similar sign frequently leads to vortex mergers. Consequently, the number of vortices decreases and their typical sizes increase. This generates a vortex population with a broad distribution of size and circulation. At very late times, for systems with zero average vorticity in periodic or bounded domains, the inverse energy cascade and mergers ultimately result in a single vortex dipole with the largest spatial scale allowed. This dipole is usually characterized by a very small "nonlinearity", $[\psi, \nabla^2\psi] \approx 0$, and it decays slowly due to dissipation.

Figure 7.2 shows the vorticity field in a representative numerical simulation of freely-decaying 2D turbulence. The vorticity is shown at intermediate times when many vortices are still present.

7.4 Properties of individual vortices

Broadly speaking, a coherent vortex is a region of circulating flow that keeps its identity for times much longer than the local eddy turnover time T_Z, which can be defined as $T_Z \approx Z_v^{-1/2}$ where Z_v is the local average enstrophy. Although the formation of coherent vortices has often been associated with the inverse energy cascade, there is - up to now - no fully satisfactory explanation of why coherent vortices form in rapidly rotating fluids. The formation of coherent vortices is probably the most important topic of 2D turbulence; it is reassuring that new generations of fluid mechanicians still have room to study interesting issues.

Given that we do not know why vortices form, we can nevertheless study what their properties are. But first we need a sensible definition of the vortices themselves; simply identifying persistent circulating motions as vortices is not a very precise definition.

One way of parameterizing the complex structure of 2D turbulence is based on the definition of the Okubo-Weiss parameter, Q, which measures the relative contribution of the squared strain S^2 and of the squared vorticity ω^2. More specifically, $Q = Q(x, y, t) = S^2 - \omega^2$, where $S^2 = {S_n}^2 + {S_s}^2$, $S_n = \partial_x u - \partial_y v$ and $S_s = \partial_x v + \partial_y u$; here S_n and S_s are the normal and shear components of strain, respectively.

Regions dominated by rotation are called elliptic, and are characterized by $Q < 0$. Regions that are dominated by strain and deformation are termed hyperbolic and have $Q > 0$. The value of Q can be thought of as defining the behavior of advected particles in the *frozen* velocity field: regions with $Q > 0$ are characterized by local exponential divergence of nearby particles, while regions with $Q < 0$ are characterized by an approximately constant separation between nearby particles. Of course, this does not bear any direct information on the chaotic or regular nature of the trajectories of advected particles in the evolving field, but the idea is occasionally useful.

The relevance of the Okubo-Weiss parameter Q may be further understood by applying the divergence operator to the incompressible Navier-Stokes equation in the limit of vanishing viscosity, or for a statistically stationary situation where forcing and damping balance each

other. One obtains in this case

$$\nabla^2 p = -\frac{1}{2}Q \tag{7.21}$$

where p is the pressure. This diagnostic equation is valid for all time and it provides a link between the value of Q and the local nature of the flow field.

Based on the values of Q, three main regions can be identified in 2D turbulence:

- Vortex cores, which are characterized by strong negative values of Q.
- Strain cells surrounding the vortices, which are characterized by large positive values of Q.
- The background, where Q fluctuates between small positive and negative values. Depending on the sign of Q, the background field may be further divided into non-coherent elliptic and hyperbolic patches.

The core of coherent vortices is thus characterized by the strong dominance of rotation over strain, and is is associated with a region where Q assumes strongly negative values. The edge of a coherent vortex can then be defined as the innermost contour for which $Q = 0$.

From a Lagrangian viewpoint, there is a significant difference between a vortex core and the external field. Inside vortex cores, the fluid motion is essentially laminar and particle trajectories are regular. This can be quantified by considering the relative dispersion between pairs of nearby particles, which is defined as the average, squared distance between two particles that were initially released close to one another. Inside a vortex, nearby particles display a very small relative dispersion along the radial direction (Provenzale, 1999). Along the azimuthal direction, though, the differential rotation of the vortex induces a relative dispersion that grows linearly in time. Outside vortices, on the other hand, one observes exponentially growing separations between nearby particles.

Coherent vortices in barotropic turbulence can therefore be interpreted as islands of regular Lagrangian dynamics in a chaotic background. It is interesting to note that these regular islands are not fixed in space and time; they wander chaotically through the turbulent field and have finite lifetime. The lack of chaoticity inside the vortices indicates that Lagrangian transport is very weak there. Instead, mixing occurs on a diffusive time scale determined by the combined action of viscosity and differential rotation inside the vortex.

Another important property of coherent vortices is that their boundaries act as relatively impermeable barriers to mixing: there is almost no exchange of particles across the periphery of an isolated vortex. Thus, particles inside a coherent vortex tend to remain there for long times, and to be transported with the vortex motion.

This behavior of coherent vortices can be understood by noting that a strong vorticity gradient is present at the vortex edge. In two-dimensional turbulence, relative vorticity is a material invariant when forcing and dissipation are absent. In the presence of forcing, dissipation or weak three-dimensional effects, vorticity is not exactly conserved and fluid particles can cross contours of constant vorticity. But if the perturbing effects are weak, particles cannot significantly change their vorticity "label". Thus, regions of uniform or gently variable

vorticity can be easily traversed by fluid particles, but regions of large vorticity gradient act as transport barriers.

Thus, mixing in vortices can be very slow and particles often become bound there. To some degree this remains true even during vortex interactions, because the cores of the interacting vortices can remain relatively intact during the interaction. However, mixing can be accelerated by strong vortex interactions which substantially disrupt the structure of the core. This happens, for example, in vortex mergers; when one vortex is much larger than the other it tears the weaker vortex apart into sheared filaments (see the next lecture). Any particles that were contained in the weaker vortex become thrown out into the chaotic background, or are entrained into the surviving structure.

The general picture of 2D turbulence that emerges is thus a low-energy background field, over which strong vorticity concentrations move and interact with one another. These coherent structures dominate the dynamics of the system, and undergo both long-range, elastic interactions and strongly inelastic processes such as straining and merging. These coherent vortices keep their identity for long times, and can be defined as regions of laminar motion where fluid particles are trapped, even though they are immersed in a turbulent sea of disorganized motion. The vortices themselves follow chaotic trajectories in the flow, and from time to time they release the fluid entrained in them during strong interactions.

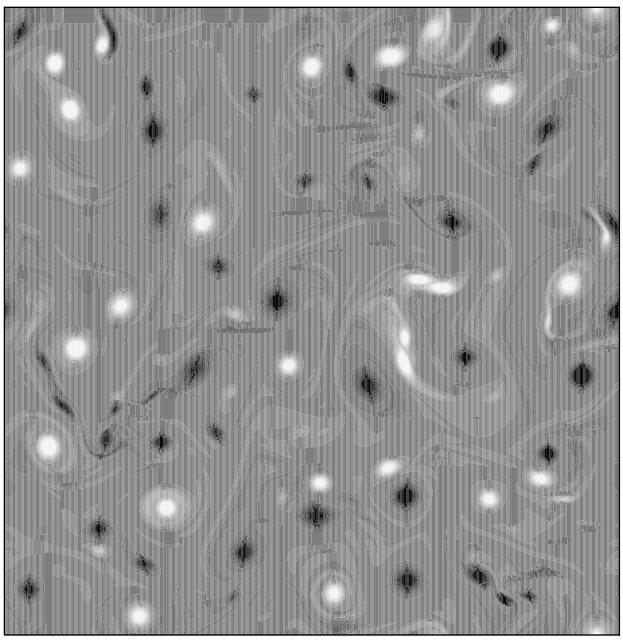

Figure 7.2: Numerical simulation of freely decaying, two-dimensional turbulence. Shown is the vorticity at time $t = 10$. The simulation began from an initially random vorticity field characterized by the energy spectrum $E(k) = E_0 k^6/(2k_0 + k)^{18}$ and random Fourier phases. Here $k_0 = 30$ and E_0 is a normalization factor which is fixed by requiring the initial average energy $E/L^2 = \frac{1}{L^2}\int E(k)dk = 0.5$. Boundary conditions are periodic, in a square box with size $L = 2\pi$. For this simulation, a pseudospectral code with standard 2/3 dealiasing and resolution 512^2 grid point has been used. The time integration is performed by a third-order Adams-Bashforth scheme and dissipation is provided by a biharmonic term $D = -\nu_2\nabla^4\nabla^2\psi$ with $\nu_2 = 5 \cdot 10^{-8}$.

Lecture 8

Dynamics of Coherent Vortices

The coherent vortices that spontaneously emerge in rotating fluids do not live in isolation, as they interact both with each other and with the turbulent background that surrounds them. We now consider some of the processes that affect the life of a vortex, and explore the properties of an ensemble of vortices in 2D turbulence. A simplified, low-order model based on a point-vortex approximation will also be discussed. Then, we explore the fate of coherent vortices in baroclinic fluids on a rotating planet with a free surface, and in magnetohydrodynamics (MHD).

8.1 When vortices collide

As described in the previous lecture, the coherent vortices of 2D turbulence experience both long-range elastic interactions when they are widely separated, and strong inelastic interactions when they become close to each other. The long-term evolution of freely-decaying turbulence is largely dictated by the inelastic processes, in particular, by vortex merging.

Most of our knowledge of what happens when vortices collide comes from numerical simulation. A particularly important case is the interaction of vortices with the same sign. When such vortices come within a critical distance of each other they occasionally merge into one object, or sometimes survive as separate entities. On other occasions, a vortex becomes torn asunder by the other, and the victor entrains part of the remnants in a vortical feast. But essentially, interaction is a complicated phenomenon with intricate details and many outcomes (Dritschel 1995).

We can crudely classify interactions of this kind according to the ratio of the vortex radii, R_2/R_1, and by the initial distance that separates them, Δ. When the vortices have about the same strength, and $R_1 \approx R_2$, the interaction is largely symmetrical. Then, if their initial separation is not too large, the vortices wrap around each other to form a new entity. Simultaneously, filaments are shed from the newly created vortex that preserve its balance of angular momentum. This is "complete merger". If the initial separation is larger, however, the two vortices survive, but parts of their structure are stripped off during the interaction. These filaments can become lost in the background, or wind around the interacting vortices, adding

to their strength.

For larger disparities in the size of the vortices, *straining out* can occur. This means that the straining field created by the larger of the two vortices is large enough to significantly distort the structure of the weaker vortex whilst the larger vortex remains relatively undisturbed. If the initial separation is not that great, the smaller vortex is completely destroyed; for larger separations, a remnant sometimes remains intact.

In both cases, the surviving vortices can entrain the fluid stripped off their competitors. If the entrained fluid is quite large, we might call this "partial merger". Both this cannibalization and the complete mergers lead to the gradual attrition of smaller vortices in favour of larger ones. Thus, inexorably, the number of vortices decreases in time as their size increases; ultimately only a few remain, to be dissipated by viscosity and friction.

Usually, mergers occur relatively quickly, and the whole process lasts only a few eddy turnover times. However, even if a complete merger happens, the fluid particles belonging to the two individual vortices do not truly mix until much later times; the filamentation created by interaction remains distinct until the fluid eventually intermingles through viscous diffusion.

8.2 Evolution of vortex statistics

Due to the processes of merging and straining, the total number $N(t)$ of vortices present in a 2D turbulent field varies with time. In particular, due to mergers and straining out, $N(t)$ decreases. Note that it is not immediately obvious that vortex interactions should act in this way: if the vorticity filaments shed by the merging vortices were underwent a secondary instability that "wraps them up", then new vortices could be generated. In principle, there is no obvious reason why this seeding of new vortices might overwhelm the effects of mergers and straining and lead to statistics in which $N(t)$ increased with time. However, there are some crude scaling arguments, described below, that suggest otherwise, and which agree with what is seen in numerical simulation and with experiments.

First, let us assume that only the energy remains constant during a merging process. Since the domain size is constant, the number of vortices in the domain must be inversely proportional to the square of the average distance λ between two vortices. Then, by dimensional arguments, we take λ to be proportional to the product of time and a speed determined from the (constant) energy: $\lambda = t\sqrt{E}$. Consequently,

$$N(t) \propto \frac{1}{\lambda^2} \propto \frac{1}{Et^2}. \tag{8.1}$$

Thus, $N(t) \propto t^{-2}$.

However, direct numerical simulation of 2D turbulence suggest, in fact, that the number of vortices decreases much more slowly than this. Low-resolution simulations (Weiss & McWilliams 1993) indicate that the number of vortices decreases as a power law, $N(t) \propto t^{-\xi}$, with $\xi \approx 0.72$. This result can be rationalized by supposing that energy is not the only conserved quantity during a merging process. Suppose instead that the peak vorticity, ζ_{ext}, is also constant during merger. The energy per unit area is given by $\epsilon = \zeta_{ext}^2 a^2$, where a is the

average radius of the vortices. The total energy is then given by

$$E = N\zeta_{ext}^2 a^4. \tag{8.2}$$

Now suppose that $N(t)$ can be written in the form,

$$N(t) = l^{-2} g(t/\tau), \tag{8.3}$$

where $l = \sqrt{E}/\zeta_{ext}$ and $\tau = \zeta_{ext}^{-1}$. If the function g has power-law form, $g \propto t^{-\xi}$, then, in order to satisfy (8.2), the average vortex radius, a, and circulation, Γ, must be given by

$$a \propto t^{\xi/4} \qquad \Gamma \propto \xi_{ext} a^2 \propto t^{\xi/2}. \tag{8.4}$$

This argument does not provide the form of $N(t)$, but it does predict the time dependence of $a(t)$ and $\Gamma(t)$, given $N(t)$. Should we observe such scalings in the numerical simulation, then, presumably, the argument is self-consistent and roughly correct.

The above relationships were indeed observed from the numerical simulations at times beyond the era of vortex formation (Weiss *et al.* 1993). A repetition of the simulations at much larger Reynolds number and higher resolution has provided similar results, indicating that the scaling behavior seems to be a robust property of freely-decaying 2D turbulence (Bracco *et al.*, in preparation). It remains to identify what theoretical arguments could justify a power-law form of $N(t)$, and to understand what determines the value of the scaling exponent, ξ.

8.3 Systems of point vortices

Systems of point vortices represent an extreme form of vortex-dominated flows. Here, vorticity is concentrated in point-like singularities which move due to their mutual advection, and the fluid between the singularities is completely passive. The description of 2D turbulence in terms of point vortices can be obtained by discarding viscosity and supposing that the vorticity is concentrated in a set of singular points, ideally representing the intense coherent structures discussed above. As we indicate below, the partial differential equations describing the motion of the fluid are then replaced by ordinary differential equations determining the positions of the point vortices (see Aref (1983) for a review). Note that, in this approach, the individual vortices do not have internal degrees of freedom, and are characterized by their (constant) circulation and (evolving) position. More complex expansions, based for example on modelling each vortex as a constant elliptical patch of vorticity, have also been introduced.

Formally, point vortices are singular solutions of the two-dimensional Euler equations. In a system of N point vortices, the vorticity distribution is given by

$$\omega(\mathbf{x}) = \sum_{j=1}^{N} \Gamma_j \delta(\mathbf{x} - \mathbf{x}_j). \tag{8.5}$$

The stream function due to a point vortex centred at $\mathbf{x}_j$ with a circulation Γ_j is given by

$$\nabla^2 \psi_j = \Gamma_j \delta(\mathbf{x} - \mathbf{x}_j). \tag{8.6}$$

If $G(\mathbf{x}, \mathbf{x}_j)$ is the solution of $\nabla^2 G = \delta(\mathbf{x} - \mathbf{x}_j)$ (that is, the Green function of the Laplacian in the relevant geometry), then

$$\psi_j(\mathbf{x}) = \Gamma_j G(\mathbf{x}, \mathbf{x}_j). \tag{8.7}$$

The Eulerian velocity components at $\mathbf{x}$ due to the jth vortex are then

$$u_j(\mathbf{x}) = -\frac{\partial \psi_j}{\partial y} = -\Gamma_j \frac{\partial}{\partial y} G(\mathbf{x}, \mathbf{x}_j) \tag{8.8}$$

and

$$v_j(\mathbf{x}) = +\frac{\partial \psi_j}{\partial x} = +\Gamma_j \frac{\partial}{\partial x} G(\mathbf{x}, \mathbf{x}_j). \tag{8.9}$$

In the point-vortex approximation, each vortex moves due to the velocity field generated by the other vortices. Thus, the coordinates of the ith vortex, (x_i, y_i), evolve according to

$$\frac{dx_i}{dt} = -\sum_{j \neq i} \Gamma_j \frac{\partial G_{ij}}{\partial y_i} \tag{8.10}$$

and

$$\frac{dy_i}{dt} = +\sum_{j \neq i} \Gamma_j \frac{\partial G_{ij}}{\partial x_i}, \tag{8.11}$$

where $G_{ij} = G(\mathbf{x}_i, \mathbf{x}_j)$.

A system of point vortices is a Hamiltonian system. The Hamiltonian is given by

$$H(\mathbf{x}_i) = -\frac{1}{2} \sum_{i \neq j} \sum_{j=1}^{N} \Gamma_i \Gamma_j G(\mathbf{x}_i, \mathbf{x}_j) \tag{8.12}$$

and the evolution of (x_i, y_i) is obtained from

$$\Gamma_i \frac{dx_i}{dt} = +\frac{\partial H}{\partial y_i} \qquad \text{and} \qquad \Gamma_j \frac{dy_i}{dt} = -\frac{\partial H}{\partial x_i}. \tag{8.13}$$

Note that, in equation (8.13), the canonically conjugate variables are x_i and y_i. That is, the space coordinate y_i plays the role usually performed by linear momentum.

Each vortex represents a degree of freedom in the Hamiltonian system (two dimensions in phase space, in the terminology of Hamiltonian dynamics, not dissipative dynamical systems); with N vortices, there are N degrees of freedom and $2N$ dimensions in phase space. Note, also, that the form of the point-vortex Hamiltonian is quite peculiar, as there is no kinetic term and only the interaction energy (related to the distance between vortices) enters its expression.

A system of point vortices can have several invariants of the motion, other than the energy. Clearly, the total circulation $\sum_j \Gamma_j$ is constant, but this does not constitute a dynamical invariant (circulation is automatically conserved by the point-vortex form of the vorticity). Linear momenta for point vortices are traditionally defined as

$$P = \sum_i \Gamma_i y_i \qquad \text{and} \qquad Q = \sum_i \Gamma_i x_i. \tag{8.14}$$

Similarly, angular momentum is defined as

$$I = \sum_i \Gamma_i (x_i^2 + y_i^2). \tag{8.15}$$

Depending on the boundary conditions used, linear and angular momenta can be invariants of the system. The existence of these conserved quantities introduces important constraints on the dynamics of point vortices. If the system has N_0 independent conserved quantities, the motion of $N \leq N_0$ vortices is regular and the maximum Lyapunov exponent in the $2N$-dimensional phase space is zero. But the motion of $N > N_0$ point vortices is in general chaotic, with a positive maximum Lyapunov exponent (see Aref, 1983).

On the infinite plane, the Green's function is

$$G(\mathbf{x}_i, \mathbf{x}_j) = \frac{1}{2\pi} \ln r_{ij}^2, \tag{8.16}$$

where

$$r_{ij}^2 = (x_i - x_j)^2 + (y_i - y_j)^2. \tag{8.17}$$

Substitution of equation (8.16) into equations (8.10) and (8.11) gives

$$\frac{dx_i}{dt} = -\sum_{j \neq i} \frac{\Gamma_j}{2\pi} \frac{y_i - y_j}{r_{ij}^2} \tag{8.18}$$

and

$$\frac{dy_i}{dt} = +\sum_{j \neq i} \frac{\Gamma_j}{2\pi} \frac{x_i - x_j}{r_{ij}^2}. \tag{8.19}$$

For this system, in the case of a non-zero total circulation, there are three independent conserved quantities, namely the energy, the angular momentum, and one component of the linear momentum. Thus, if the number of point vortices is less than or equal to three, the motion is regular; but if there are more than three vortices, chaotic motion is possible and is generally observed for generic initial conditions.

Vortices having the same sign undergo a bounded motion on the infinite plane. In this case, vortices cannot get too far or too close to each other due to the simultanous conservation of energy and angular momentum. By contrast, if vortices on the infinite plane have opposite signs, unbounded motion can occur, due to the formation of dipoles that travel off to infinity.

Another important case is that of periodic boundary conditions (motion on a torus). In this case, angular momentum is not conserved. For a periodic domain the Green's function is given by (Weiss & McWilliams 1991)

$$G(\mathbf{x}_i, \mathbf{x}_j) = \sum_{m=-\infty}^{\infty} \ln \left[\frac{\cosh(x_i - x_j - 2\pi m) - \cos(y_i - y_j)}{\cosh(2\pi m)} \right] - \frac{(x_i - x_j)^2}{2\pi}. \tag{8.20}$$

The velocity of the ith vortex is then determined by substituting equation (8.20) into equations (8.10) and equation (8.11). This gives

$$\frac{dx_i}{dt} = -\sum_{j=1, j \neq i}^{N} \Gamma_j \sum_{m=-\infty}^{\infty} \frac{\sin(y_i - y_j)}{\cosh(x_i - x_j - 2\pi m) - \cos(y_i - y_j)} \tag{8.21}$$

and

$$\frac{dy_i}{dt} = \sum_{j=1, j\neq i}^{N} \Gamma_j \sum_{m=-\infty}^{\infty} \frac{\sin(x_i - x_j)}{\cosh(y_i - y_j - 2\pi m) - \cos(x_i - x_j)}. \tag{8.22}$$

Systems of N vortices on the periodic domain have been used to model the properties of 2D turbulence, primarily in studying the trajectories of individual vortices subject to long-range elastic interactions with the other vortices. In systems of a large number of point vortices, the motion of each individual vortex can be decomposed into periods of quasi-random motion, associated with the mean velocity field generated by the vortex ensemble, and rare, but long, quasi-ballistic flights generated by the temporary coupling of two opposite-sign vortices into a dipole. A dipole travels rapidly across the domain, until it is destroyed by a close encounter with another vortex (Weiss *et al.*, 1998). .

The main drawback of point-vortex systems as models of turbulence is the absence of inelastic interactions such as vortex mergers, which play a crucial role in the evolution. An attempt to introduce a parameterization of mergers was given by Carnevale *et al.* (1991). In this approach, it is assumed that the vortices evolve according to (8.10)-(8.11) whilst they are all well separated. But if two same-sign vortices come within a certain distance of each other, then they "merge" according to the following prescription: Consistent with indications from numerical simulation of 2D turbulence (as discussed in the previous section), it is assumed that during a merger both energy and peak vorticity are conserved. By contrast, circulation is not conserved during the merger because of dissipation. Therefore, during the merging of two same-sign vortices *with equal amplitude* (the case considered by Carnevale *et al.*), the peak vorticity, ζ, and vortex radii, a, satisfy

$$\zeta_3 = \zeta_1 = \zeta_2 \tag{8.23}$$

and

$$a_3^4 = a_1^4 + a_2^4, \tag{8.24}$$

where the subscript 3 refers to the vortex created by the merging of vortices 1 and 2. The critical distance below which two vortices, with radii a_1 and a_2, merge is fixed at

$$d_c = 3.3 \left(\frac{a_1 + a_2}{2} \right), \tag{8.25}$$

which is suggested from simulations.

By using this approach, Carnevale *et al.* were able to reproduce the statistical behavior of the population of extended vortices in 2D turbulence. Because the system takes the form an evolving population of point vortices interrupted by instantaneous mergers, Carnevale *et al.* coined the term "Punctuated Hamiltonian Dynamics" to describe it, much as biologists refer to one possible scenario for the evolution of species. But, leaving aside this pleasant analogy, we learn that the point-vortex metaphor, with its artifice of merging appears to reproduce some of the gross aspects of two-dimensional turbulence.

8.4 Effects of a free surface, β, and baroclinicity

We now discuss the fate of coherent vortices when the effects of the free surface, planetary rotation and baroclinicity cannot be neglected.

Let us first consider the role of the free surface and the $\beta-$effect in a barotropic fluid. We recall the equation for barotropic quasi-geostrophic (QG) turbulence:

$$\frac{\partial q}{\partial t} + [\psi, q] = D, \tag{8.26}$$

where the potential vorticity q is given by

$$q = \nabla^2 \psi - \frac{\psi}{R^2} + \beta y \tag{8.27}$$

and $D = (-1)^{s-1}\nu\nabla^{2s}\nabla^2\psi$ is the dissipation term.

The potential vorticity equation (8.26) describes the evolution of q as a result of the velocity field prescribed by ψ. But that streamfunction is related to the potential vorticity through (8.27). However, as we have seen for freely decaying two-dimensional turbulence, the dynamics is dominated by the interaction of coherent vortices. Thus the kinds of solutions that we are interested in are those for which q is approximately composed of a sum of well separated, localized vortices:

$$q \sim \sum_j q_j. \tag{8.28}$$

Each of the q_j closely corresponds to the solution for an isolated vortex. In that circumstance we can approximately write ψ as a sum over the streamfunctions associated with each of these vortices:

$$\psi \sim \sum_j \psi_j. \tag{8.29}$$

Thus, an approximate equation for the motion of the j^{th} vortex is given by

$$\frac{\partial q_j}{\partial t} + [\psi_j, q_j] \sim -\sum_{l, l\neq j} [\psi_l, q_j], \tag{8.30}$$

if we ignore dissipation, and because the vorticity of the objects is more localized than the streamfunction. This equation describes how the vortex evolves under the combined influence of the others; the right-hand side models vortex interactions. Importantly, the interaction is mediated by the streamfunctions, and so to understand the effects of the free surface and β we must explore how the corresponding terms modify ψ. But

$$\psi = \int\int G(\mathbf{x}, \mathbf{x}') q(\mathbf{x}', t) d\mathbf{x}', \tag{8.31}$$

where $G(\mathbf{x}, \mathbf{x}')$ denotes the Green function of the Laplacian. Hence, the key to understanding the new terms lies in how they modify the structure of the Green function.

If the Rossby deformation radius, R, is infinite and $\beta = 0$, equations (8.26) and (8.27) reduce to those for 2D turbulence with $q = \nabla^2\psi$. In this case the Green's function for the system is a solution to

$$\nabla^2 G = \delta(\mathbf{x} - \mathbf{x}_j) = \delta(r), \tag{8.32}$$

for which $G \propto \ln r$ on the infinite plane (see equation (8.16)). If R is finite (but β still zero), then

$$\nabla^2 G - \frac{G}{R^2} = \delta(r). \tag{8.33}$$

This Green function has the form $G \propto \ln r$ for $r < R$, and $G \propto \exp(-r/R)$ for $r \geq R$. The exponential decay of the Green's function at large r reflects a "shielding" effect by the free surface. As a result, vortex interactions become spatially more localized (see, for example, the report by Mockett elsewhere in this volume). For the same reason, the presence of a free surface slows down the inverse cascade at scales larger than R; at the larger scales, nonlinear couplings are weakened. At scales smaller than R, on the other hand, the dynamics remains basically that of 2D turbulence. Coherent vortices thus form and grow by merging until they reach a scale of order R. After this stage, the evolution becomes very slow because the different vortices interact much more weakly with each other. This is illustrated in figure 8.1, which shows the result of a numerical simulation. This picture should be compared with the corresponding figure 7.2 in lecture 7. The comparison shows that vortices in the fluid with a free surface are more numerous and smaller, as expected from the reduction in interactions and therefore mergers.

The latitudinal variation of the planetary rotation, modelled by $\beta \neq 0$, has a more significant influence (see, for example, Rhines 1975 and 1979; McWilliams 1984). In particular, the β-term introduces an upper scale $L_\beta = (U/\beta)^{1/2}$, above which the inverse energy cascade is actually inhibited. (Here, U is again a typical velocity scale which is determined by the dynamics.) The essential reason behind this arrest of the cascade is that, on sufficiently long scales, the $\beta-$effect dominates any nonlinearity, and the fluid equations become practically linear. These linear equations describe Rossby waves.

The length L_β is called the Rhines scale, and above it Rossby waves dominate the dynamics; usually, coherent vortices cannot grow larger than L_β. Even below the Rhines scale, β-plane vortices live for shorter times than their f-plane counterparts. This is because, in general, isolated monopoles on the β-plane emit Rossby waves and undergo zonal and meridional motion. Thus they decay through *radiation*, even without viscosity. Nevertheless, coherent vortices still form and persist for relatively long times. As such, they still exert a significant influence on the dynamics of the flow.

A representative simulation with $\beta \neq 0$ and $r \to \infty$ is shown in figure 8.2. This picture is to be compared with figures 7.2 and 8.1. The most obvious feature of the case with β is that there are significantly fewer vortices, but there is also large-scale structure that we associate with the Rossby waves.

When we add both β and finite R at the same time, there is in some sense a mixture of the two effects of these terms: there is both shielding and Rossby-wave radiation. Interestingly, the free surface can partially shield the destructive effects of differential planetary rotation,

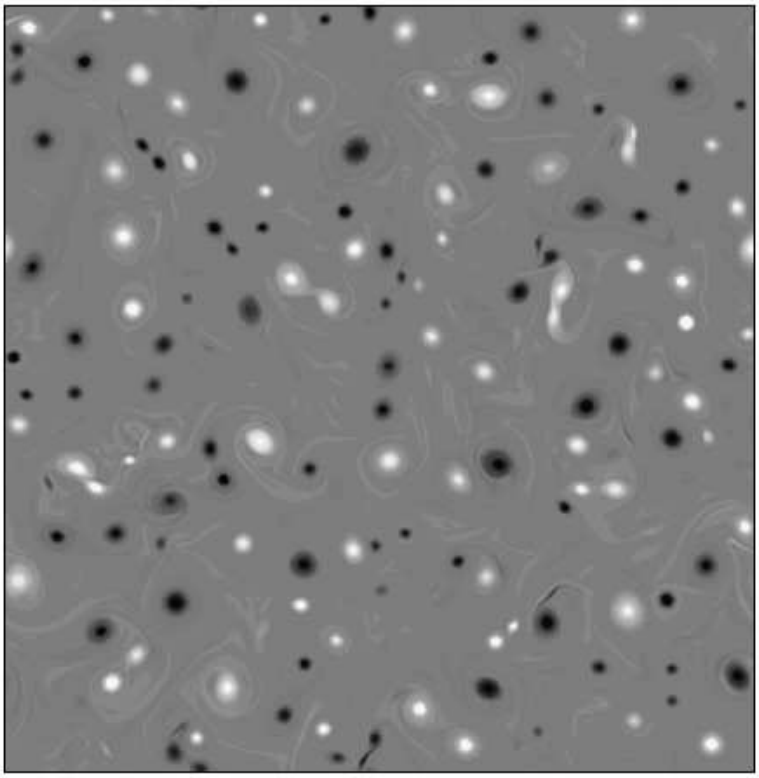

Figure 8.1: Numerical simulation of freely decaying, two-dimensional turbulence with $R = 0.2$ and $\beta = 0$. Shown is the vorticity field at $t = 10$. The numerical scheme is described in the caption to figure 7.2.

leading to vortices that can live for very long times in fluids with both β and a free surface. But otherwise, the overall dynamics remains much the same.

Finally, we briefly discuss the role of baroclinic effects. For baroclinic QG flow another form of potential vorticity must be used. The conservation of QG potential vorticity in a stratified flow takes the form

$$\frac{\partial q}{\partial t} + [\psi, q] = D \tag{8.34}$$

and

$$q = \frac{\partial^2 \psi}{\partial x^2} + \frac{\partial^2 \psi}{\partial y^2} + \frac{\partial}{\partial z}\frac{f^2}{N^2}\frac{\partial}{\partial z}\psi, \tag{8.35}$$

where N is the Brunt-Vaisala frequency given by

$$N^2 = -\frac{g}{\rho}\frac{d\rho}{dz}. \tag{8.36}$$

For constant N, the z coordinate can be rescaled as $z' = (N/f)z$ so that q can then be written as

$$q = \nabla^2_{3D}\psi \tag{8.37}$$

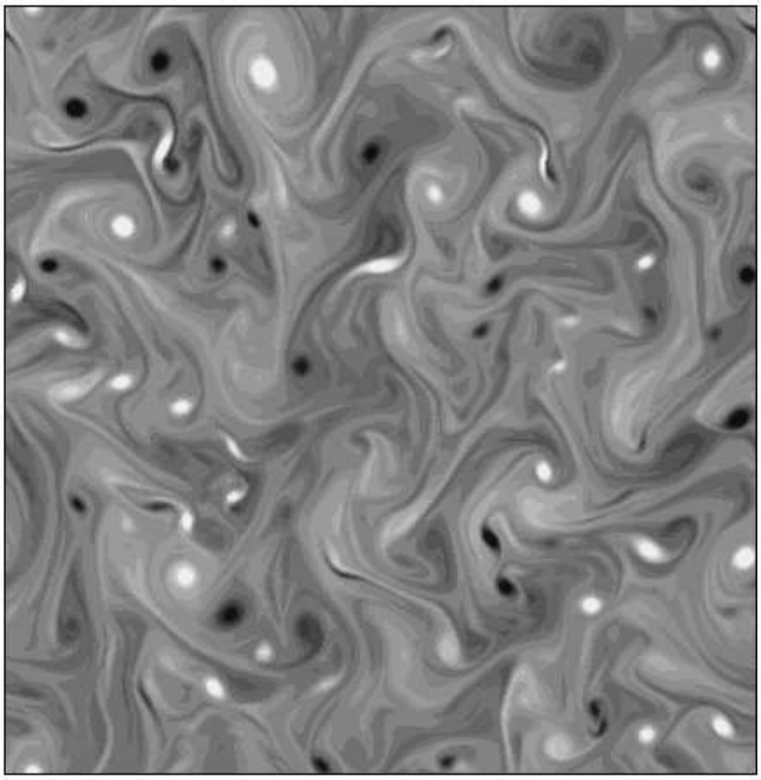

Figure 8.2: Numerical simulation of freely decaying, two-dimensional turbulence with $\beta = 10$ and $R \to \infty$. Shown is the vorticity field at $t = 10$. The numerical scheme is described in the caption to figure 7.2.

where ∇^2_{3D} is the three-dimensional Laplacian. In this system, the Green's function for the infinite plane takes the form $G \propto 1/r$. Once again this leads to interactions that are more localized than in two-dimensional turbulence, and prolongs the run down of a freely decaying system.

The dynamics of stratified QG turbulence has been numerically studied by several authors (e.g. McWilliams 1989; McWilliams & Weiss 1994; McWilliams, Weiss & Yavneh 1994). The simulations show that an initially random vorticity field organizes itself into well-defined coherent vortices, similarly to what happens in 2D turbulence. The vortices initially take the form of three-dimensional, ellipsoidal vorticity concentrations, reminiscent of ocean structures (for example, the Meddies). These vortices undergo long-range elastic interactions with each other, and occasional inelastic interactions (such as mergers and straining), much like their two-dimensional counterparts. A new feature present in this system, however, is that vortices on different vertical levels tend to align into columnar structures, when they become sufficiently close to each other. As a result, freely-decaying systems display some tendency to evolve to a final state composed of two tall columns of opposite vorticity, somehwat analogous to the final dipolar state observed for 2D turbulence. Although the stratified case has been explored less

thoroughly than the barotropic one, one can safely conclude that, here too, there is a robust tendency to form coherent vortices, which then dominate the system evolution.

8.5 Magnetic vortices

Up to now, we have considered a purely hydrodynamical situation, where electromagnetic forces do not play any role. In most astrophysical flows, however, magnetic effects cannot be discarded. In keeping with the attitude of staying as simple as possible (and sometimes even simpler than that), here we mention the issue of vortex formation in two-dimensional incompressible magnetohydrodynamics.

If the conducting fluid is incompressible, and it is subject to a strong constant magnetic field along z (the ordering field that we discussed in Lecture 7), one can make the following approximations to the full equations of MHD:

$$\partial_z \to 0, \quad w = 0, \quad B_z = \text{constant}$$

where w is the fluid velocity and B_z is the magnetic field in the z direction. Thus, the only dynamical variables left are the velocity, $\mathbf{u} = (u, v)$, and magnetic field, $\mathbf{B}_h = (B_x, B_y)$, in the (x, y) plane. Both $\mathbf{u}$ and $\mathbf{B}_h$ are divergenceless, and can be expressed as

$$u = -\frac{\partial \psi}{\partial y} \ , \ v = \frac{\partial \psi}{\partial x} \tag{8.38}$$

and

$$B_x = -\frac{\partial a}{\partial y} \ , \ B_y = \frac{\partial a}{\partial x}, \tag{8.39}$$

where ψ is the stream function and a is the magnetic potential. The vorticity is given as usual by $\omega = \nabla^2 \psi$. Analogously, the only relevant component of the current, $\mathbf{j} = \nabla \times \mathbf{B}$, is that in the z direction, and is given by $j = \nabla^2 a$.

The evolution equations for the flow take the form,

$$\partial_t \nabla^2 \psi + [\psi, \nabla^2 \psi] - [a, \nabla^2 a] = \nu \nabla^2 \nabla^2 \psi$$

and

$$\partial_t a + [\psi, a] = \eta \nabla^2 a,$$

where we have introduced a Newtonian viscosity ν and a resistivity η. These equations are intriguing. Imagine, for example, if we discarded the term $[a, \nabla^2 a]$ in the first equation (the Lorentz force). Then, one is left with standard 2D turbulence, with the addition of a passive scalar field a which is advected by the flow, with no feedback on the flow itself. This is similar to the *kinematic dynamo problem* in which one studies whether a given velocity field can amplify an embedded, passive magnetic field. However, by turning on the term $[a, \nabla^2 a]$, the skew-product asymmetry is broken and the advected field a feeds back on the advecting field. In fact, this term amplifies rapidly in turbulent fluids, and the system becomes dominated by the magnetic effects.

For zero viscosity and resistivity, 2D-MHD has three quadratic invariants, namely the total energy (E), the square of the magnetic potential (A), and the cross-helicity (H). These are

$$E = \frac{1}{2}\int (u^2 + v^2) dxdy + \frac{1}{2}\int (B_x^2 + B_y^2) dxdy,$$

$$A = \int a^2 dxdy$$

and

$$H = \int uB_x + vB_y dxdy.$$

Note that, in this system, enstrophy is not conserved. This induces severe modifications in the turbulent cascades. In particular, in 2D-MHD, energy flows from large to small scales (as in 3D turbulence), and it is the magnetic potential that undergoes an inverse cascade from small to large scales.

Numerical integrations of 2D-MHD have indicated the formation of strong vorticity sheets (Biskamp *et al.* 1990), but no kinetic vortices. However, the current field develops localized structures that one might call "magnetic vortices". In other words, the current plays a similar role to that played by vorticity in the simpler hydrodynamical case (Kinney *et al.* 1995).

The details of the dynamics of 2D-MHD are very complex, depending, for example, on the initial ratio between kinetic and magnetic energy and on the cross-correlation between the fluid velocity and the magnetic field. Nevertheless, it is clear that coherent structures do play a crucial role in this system as well. But here, we deal with coherent magnetic flux tubes rather than with vortices, and these magnetic coherent structures are reminiscent (to the eye of the believer) of the coherent magnetic flux tubes associated with sunspots.

Lecture 9

Floats, Balloons, and Planets

With a final effort, we consider what happens to particles that are transported by a fluid flow. If the tracers are passive (that is, they do not feed back on the advecting fluid), then we are in the presence of another skew-product system, where the driver is the Eulerian flow and the driven system is represented by the advected tracers.

9.1 Chaotic advection

How can we model the motion of a particle advected by a flow? Let us first suppose that the particle under study is passive, point-like and it has a vanishing inertia with respect to the advecting fluid. That is, it is a passive fluid particle. The equations of motion for such a particle are obtained by equating the Lagrangian velocity and the Eulerian fluid velocity at the particle position, i.e.

$$\frac{d\mathbf{x}}{dt} = \mathbf{V}(t) = \mathbf{u}(\mathbf{x}, t), \tag{9.1}$$

where $\mathbf{x}(t) = (x(t), y(t))$ is the particle position at time t, $\mathbf{V}(t)$ is its Lagrangian velocity, and $\mathbf{u}(\mathbf{x}, t)$ is the Eulerian velocity at point $\mathbf{x}$ and time t. For simplicity, we have assumed a two-dimensional velocity field.

For two-dimensional incompressible flows, such as those discussed in Lectures 7 and 8, the Eulerian velocity may be expressed in terms of a stream function $\psi(x, y, t)$. In this case, equation (9.1) becomes

$$\frac{dx}{dt} = -\frac{\partial \psi}{\partial y} \quad ; \quad \frac{dy}{dt} = \frac{\partial \psi}{\partial x} \quad . \tag{9.2}$$

Equation (9.2) formally defines an Hamiltonian system with one degree of freedom, described by the canonically conjugate variables x and y. Here, the stream function ψ plays the role of the Hamiltonian and the phase space of the system is the physical plane (x, y) (see e.g. Ottino, 1989). For stationary stream functions, system (9.2) is integrable, the particles follow the streamlines and particle trajectories are regular. When the stream function is time-dependent (for example, periodic in time), the system becomes non-integrable. In this case, chaotic particle trajectories are in general expected and the Lagrangian motion may become

highly irregular even if the Eulerian dynamics is simple. This type of behavior is known as *chaotic advection*, and it has been shown to be of some use in the description of particle advection in flows dominated by one or a few structures, such as an isolated vortex, a simple jet or a single wave train.

One classic example of chaotic advection in a two-dimensional flow was studied by Solomon and Gollub (1988). They considered a time-dependent stream function representing simplified convection cells

$$\psi = A \cos x \cos (y + B \sin \Omega t).$$

If the stream function ψ is constant in time ($B = 0$) particles are constrained to stay within the cell in which they start. For $B \neq 0$ it is found that particles cross cell boundaries and undergo dispersion processes similar to those observed in turbulent flows. At short times, the mean square displacement $A^2 =< [\mathbf{x}(t) - \mathbf{x}(0)|^2 >$ of a particle ensemble increases as t^2 (ballistic motion), while on long times the motion becomes Brownian-like and $A^2 \propto t$. Examples of *anomalous* diffusion, with $A^2 \propto t^\alpha$ with $\alpha \neq 1$ at large times have also been reported.

Chaotic advection has been studied in several other flows of geophysical interest, ranging from modulated travelling waves (Weiss & Knobloch 1989), to models of the Gulf Stream (Samelson 1992) and low-resolution general circulation models of the atmosphere (Pierrehumbert & Yang 1992). The main lesson that we can learn from this approach is that even simple Eulerian flows can generate unpredictable, Brownian-like particle trajectories and strong particle dispersion. This leads to potentially serious difficulties when trying to relate Eulerian and Lagrangian statistics, and to reconstruct Eulerian flows from Lagrangian measurements. Also, we see that we do not need turbulent flows and high-dimensional stochastic processes to generate particle dispersion, as a simple time-periodic wavetrain can generate it.

9.2 Dynamics of advected impurities

In the previous section we have assumed that the advected particles have vanishing inertia with respect to the advecting fluid. Complications arise when the advected particles have finite relative inertia or size, as in the case of dust grains, gas bubbles and the floats and balloons used as Lagrangian tracers in the ocean and the atmosphere. In this case, Newton's laws have to be used, and we must equate the particle acceleration to the force per unit mass acting on the particle. The simplest expression for the equations of motion of an advected particle with finite inertia (an *impurity*) then becomes

$$\frac{d^2\mathbf{x}}{dt^2} = \delta \frac{D\mathbf{u}}{Dt} - \gamma \left(\frac{d\mathbf{x}}{dt} - \mathbf{u} \right) + \mathbf{g}(1 - \delta).$$

where

$$\delta = \frac{\rho_f}{\rho_p}$$

is the ratio of fluid density ρ_f to the density of the impurity ρ_p,

$$\gamma = \frac{9}{2} \left(\frac{a}{L} \right)^{-2} Re^{-1}$$

is the coefficient of the Stokes drag term, and

$$\frac{D}{Dt} = \frac{\partial}{\partial t} + \mathbf{u} \cdot \nabla \ .$$

For two-dimensional incompressible flows,

$$\mathbf{u} = (u, v) \ ; \ u = -\frac{\partial \psi}{\partial y} \ , \ v = \frac{\partial \psi}{\partial x}.$$

The left-hand-side of equation (9.2) represents particle acceleration. The first term on the right-hand-side represents the force that the fluid would exert on a fluid particle placed at the position of the impurity, weighted by relative inertia. The second term is the Stokes drag, and it models the friction that the fluid exerts on a particle moving with a velocity that is different from the local fluid velocity. Here, a is the radius of the particle, L is a typical length scale of the flow, and Re is the Reynolds number. γ^{-1} represents the time constant for the equilibration of the velocity of the tracer with the flow velocity. Finally, the third term represents the buoyancy force acting on the impurity.

This system has been considered by Stommel (1949) as a simplified model for the fall of heavy particles in a two-dimensional vertical plane. Consider x in the horizontal direction and y pointing vertically downward. Thus, $\mathbf{g} = (0, g)$. By discarding the particle acceleration $d^2\mathbf{x}/dt^2$ and considering very heavy particles, $\delta \to 0$, the system reduces to

$$\frac{dx}{dt} = -\frac{\partial \psi}{\partial y} \ , \ \frac{dy}{dt} = \frac{\partial \psi}{\partial x} + g$$

which can be recast in a stream function form by introducing $\phi = \psi + gx$.

For example, if $\psi = \psi_0 \sin x \sin y$, it can be shown that, depending on their initial position and velocity, some of the heavy particles can be trapped forever in recirculation regions of the flow. However, as shown by Maxey (1987), this result is spurious: if one includes the particle acceleration, no permanent trapping is possible and the fate of all heavy particles is to fall, sooner or later.

For horizontal flows, buoyancy is absent and particles are not constrained to fall under gravity. In such cases, the dynamics of the particles can depend crucially on whether they are light ($\delta > 1$), or heavy ($\delta < 1$). For example, Crisanti *et al* (1992) studied fluid laden with particles of finite δ, using the model streamfunction of Solomon & Gollub: $\psi = A \cos x \cos (y + B \sin \Omega t)$. When $B = 0$ and the flow is steady, they showed that light particles converge to the elliptic fixed points at the center of the advection cells. Heavy particles, on the other hand, are pushed outside regions of closed streamlines (as their inertia is larger than that of fluid particles) and undergo chaotic motion associated with a strange attractor in the four-dimensional phase space, $(x, y, dx/dt, dy/dt)$. For time-dependent stream functions ($B \neq 0$), the picture is more complicated and light particles can also display chaotic dynamics. In general, however, it remains true that heavy particles are pushed outside coherent structures with closed streamlines.

Note that system (9.2) is dissipative, and thus phase-space volumes shrink with time. This implies that the long-term evolution of the system takes place on a set of measure zero in the

full phase space. This is a major difference with respect to the dynamics of fluid particles, described by a Hamiltonian system for which the Liouville theorem holds. Note, also, that system (9.2) is an extension of the model used for fluid particles, to which it reduces for $\delta = 1$ and $a \to 0$ (though this is a singular limit as the order of the equation changes).

Finally, we recall that even though interesting results can be obtained with a simple system such as (9.2), the equations of motion for finite-size, finite-inertia particles are extremely complicated, as they depend, for example, on the shape of the particle itself. It is only in the case of very small spherical particles, that the equations of motion take a manageable form that can be derived from Newton's second law of motion (see Maxey & Riley (1983) for a fairly complete discussion of the dynamical equations for small spherical impurities in non-rotating systems and Tanga *et al* (1996) for the rotating case). Even in this case, however, terms known as the added mass, the Basset history term, the Faxen corrections, and the lift all participate in reminding us that the world is more complicated than we would like. Insisting in the Walsh cottage tradition of not dealing too heavily with the *accidenti*, we have decided not to talk about these complications here.

9.3 Dust in the spots

The presence of an overall rotation of the system induces new effects in the dynamics of heavy impurities. In a rotating frame, the equations of motion for an advected impurity become

$$\frac{d^2\mathbf{x}}{dt^2} = \delta\frac{D\mathbf{u}}{Dt} - \gamma\left(\frac{d\mathbf{x}}{dt} - \mathbf{u}\right) + \mathbf{g}(1-\delta) - 2\boldsymbol{\Omega}\times\left(\frac{d\mathbf{x}}{dt} - \delta\mathbf{u}\right) + |\boldsymbol{\Omega}|^2 r(1-\delta)\hat{\mathbf{r}}, \tag{9.3}$$

where we have introduced the relative Coriolis and centrifugal accelerations which are present in a rotating reference frame; here $\boldsymbol{\Omega}$ is the angular velocity of the system.

As a consequence of rotation, when heavy particles are spinning inside a coherent vortex in a rotating reference frame, they are subject to two main opposing forces: the centrifugal force, which pushes the heavy particles outside the region of closed isolines, and the Coriolis force, which - for an overall cyclonic rotation of the reference frame - pushes the particles to the right of the direction of motion. Thus, the Coriolis force pushes heavy impurities out of cyclonic vortices and it pushes them toward the center of anticyclonic vortices. Thus, in rotation-dominated systems for which the Coriolis force is stronger than the centrifugal term, heavy impurities can concentrate in the cores of anticyclonic vortices (Tanga *et al.* 1996, Provenzale 1999), in complete contrast to the nonrotating case for which heavy impurities are always ejected from coherent vortices,

Can all this be of some use in explaining the formation of planets? First, we must mention how people think of planet formation. The *nebular hypothesis* by Kant and Laplace was based on the conjecture that the solar system formed from a flattened gas cloud. Until now, this has survived as a basically correct explanation, and it has been further elaborated by realizing that stars condense from an interstellar medium composed by gas and an admixture of solid particles called interstellar dust. As the central star contracts, it leaves around it material that contains a significant portion of the initial angular momentum of the system. In this

nebula, centrifugal forces balance the stellar gravity in the radial direction and a disk forms. This is a Keplerian disk, because it is dominated by the gravity of the central star. The disk is dusty, and the dust settles toward the midplane, until it forms - in a process whose details are still poorly understood - small protoplanetary objects called planetesimals. Later on, the planetesimals start feeling the gravity of each other, cluster together to form larger objects, and the true planets are finally formed.

A crucial problem in this scenario, however, is to reconcile the time scales for growth by accumulation of objects of the size of Jupiter, and the estimated lifetime of the gaseous nebula itself. In particular, there is a lack of standard mechanisms for building planetesimals between the centimeter-sized grains formed by agglomeration and sticking, and the larger objects capable of efficiently triggering gravitational instability.

At this point, vortices enter the scene, much as the Cavalry always appeared in old, politically incorrect movies. Since coherent vortices are so common in rotating fluids, we could imagine that there are vortices in the rotating nebula. This hypothesis seems natural to fluid dynamicists, but has not been appreciated by astrophysicists, as they claimed that the strong shear present on Keplerian disks can easily destroy any incipient coherent structure. And, apart from the shear, there are several other effects (compressibility, magnetic fields, and so forth) that can complicate the picture.

In an attempt of dealing with just one problem at a time, Bracco *et al* (1998) have explored whether coherent vortices can survive in incompressible Keplerian disks. That is, whether the Keplerian shear is really able to prevent the formation of vortices. The system dynamics is governed by the standard equation for barotropic turbulence:

$$\frac{\partial}{\partial t}\nabla^2\psi + [\psi, \nabla^2\psi] = \nu\nabla^2\nabla^2\psi, \tag{9.4}$$

where a Newtonian viscosity has been added. The initial conditions at time $t = 0$ are given by

$$\psi = \psi_{Kep} + \psi', \tag{9.5}$$

where $\nabla\psi_{Kep} \propto r^{-3/2}$ represents the unperturbed Keplerian disk, and ψ' is a perturbation to the Keplerian flow.

Numerical simulation of this system indicates that weak perturbations are destroyed by the shear of the Keplerian flow. If the initial perturbations are large enough, however, coherent vortices can form even in the presence of the strong shear (see figure 9.1). Interestingly enough, only anticyclonic vortices can form, since cyclonic vortices are more readily destroyed by the shear. This is at least partly because the local, Keplerian vorticity gradient is *negative* (if we consider a local Cartesian coordinate system centerd at some particular radius). But cyclonic vortices rotate against this Keplerian background and so become sheared out. Anticyclones, however, are reinforced by the background, and so they may survive if they are of sufficient initial strength.

In general, the presence of vortices is also determined by the interplay of two limiting space scales. The smaller one, L_ν, is the scale associated with dissipative effects; below it, vortices cannot form as the nonlinear terms are overwhelmed by dissipation. The larger scale, L_{out}, is determined by the shear; above L_{out}, vortices are destroyed by the shear. Thus, vortices

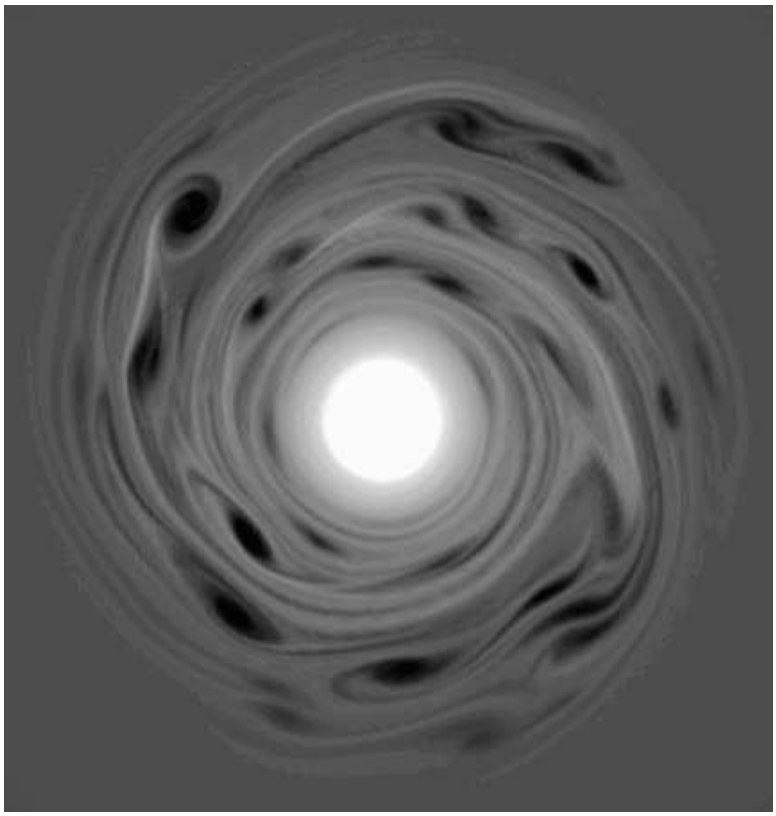

Figure 9.1: Vorticity field evolving from a perturbed Keplerian disk in the incompressible, barotropic approximation. A pseudo-spectral code with Newtonian viscosity $\nu = 5 \times 10^{-5}$ and resolution 512^2 grid points has been used. The initial mean kinetic energy of the Keplerian disk is $E_{Kep} = 0.5$ and the mean perturbation energy is $E' = 4 \times 10^{-3} E_{Kep}$. The time shown is $t = 8$. (Adapted from Bracco *et al*)

can exist only in the range between these two scales, and this requires that $L_\nu \ll L_{out}$. In conclusion, it is possible to obtain coherent anticyclonic vortices on Keplerian disks only if there are large enough initial perturbations on the Keplerian flow and the viscosity is small enough. Given this, coherent vortices happily form, and lead to what have been called *spotted disks*, by analogy with sunspots.

Given that vortices can form on (barotropic) Keplerian disks, the remainder of the metaphor for planet formation in vortices follows naturally. The dust grains in the solar nebula are very heavy, being characterized by $\delta \approx 10^{-8}$. For these impurities, the concentration mechanism discussed above is at work, and, if the rotation of the nebula is sufficiently rapid, the Coriolis force can overcome the centrifugal force of the vortices; as a consequence, the dust grains are pushed into the cores of the anticyclonic vortices (Barge & Sommeria 1995, Tanga *at al* 1996, Bracco *et al* 1998). Potentially, this leads to a relatively rapid accumulation of matter into vortex cores, and the birth of planetesimals.

Explicit numerical simulation of dust grain dynamics verifies this image; see figure 9.2. Moreover, the computations confirm that the process effectively concentrates the heavy particles and therefore expedites the formation of planetesimals. Hence, we can say that the spots on the disk are dusty.

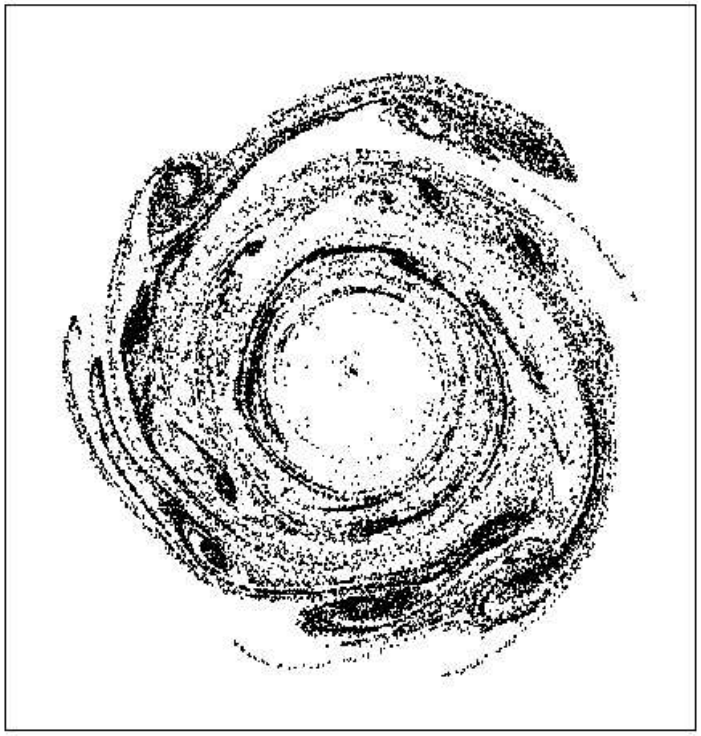

Figure 9.2: Distribution of dust grains in the perturbed Keplerian disk shown above. The particles were initially released uniformly in the disk. (Adapted from Bracco *et al.*)

The fact that vortices may have played a role in the formation of the solar system is, of course, appealing to the palate of the nonlinear dynamicist. However, the world is as usual more complicated than we depict it, and in this discussion we have for example discarded important effects such as compressibility of the gas in the disk and magnetic fields. But, just as a note, we report that preliminary simulations based on the (compressible) thin-layer aproximation indicate that vortices should be able to form in weakly compressible disks as well (Bracco *et al.* 1999).

Conclusion

We started these lecture notes by considering the motion of a dust grain in a stratified atmosphere. And we concluded them, by discussing the dynamics of dust grains in the primordial

solar nebula. In the process of passing from dust to dust, we have enjoyed an exploration of some intriguing mysteries. Nothing more should be desired, nor expected. And it is not allowed in such a short summer program.

Bibliography

[1] H. Aref, *Integrable, chaotic, and turbulent vortex motion in two-dimensional flows*, Ann. Rev. Fluid Mech., 15 (1983), pp. 345–389.

[2] E. Aurell, G. Boffetta, A. Crisanti, G. Paladin, and A. Vulpiani, Phys. Rev. Lett., 77 (1996), p. 1262.

[3] N. J. Balmforth, M. Martens, A. Provenzale, E. A. Spiegel, C. Tresser, and C.-W. Wu, *Red spectra from white and blue noise*, Proc. Roy. Soc. London B, to appear, (1998).

[4] P. Barge and J. Sommeria, *Did planet formation begin inside persistent gaseous vortices?*, Astron. Astrophys., 295 (1995), pp. L1–L4.

[5] R. Benzi, G. Parisi, A. Sutera, and A. Vulpiani, Tellus, 34 (1982), p. 10.

[6] R. Benzi, A. Sutera, and A. Vulpiani, J. Phys. A, 14 (1981), p. L453.

[7] D. Biskamp, H. Welter, and M. Walter, Phys. Fluids B, 2 (1990), p. 3024.

[8] J. Bjerknes, Tellus, 18 (1966), p. 820.

[9] G. Boffetta, A. Crisanti, F. Paparella, A. Provenzale, and A. Vulpiani, *Slow and fast dynamics in coupled systems: A time series analysis view*, Physica D, 116 (1998), pp. 301–312.

[10] A. Bracco, P. H. Chavanis, A. Provenzale, and E. A. Spiegel, *Particle aggregation in a turbulent keplerian flow*, Phys. Fluids A, submitted, (1998).

[11] A. Bracco, A. Provenzale, E. A. Spiegel, and P. Yecko, *Spotted disks*, in Theory of black hole accretion disks, M. Abramowicz, G. Björnsson, and J. Pringle, eds., Cambridge University Press, 1999.

[12] A. R. Bulsara and L. Gammaitoni, *Tuning into noise*, Physics Today, (1996), pp. 39–45.

[13] G. F. Carnevale, J. C. McWilliams, Y. Pomeau, J. B. Weiss, and W. R. Young, *Evolution of vortex statistics in two-dimensional turbulence*, Phys. Rev. Lett., 66 (1991), pp. 2735–2737.

[14] P. Cessi, *A simple box model of stochastically forced thermohaline flow*, J. Phys. Oceanog., 24 (1994), pp. 1911–1920.

[15] J. G. Charney and J. G. DeVore, *Multiple flow equilibria in the atmosphere and blocking*, J. Atmos. Sci., 36 (1979), pp. 1205–1216.

[16] A. Crisanti, M. Falcioni, A. Provenzale, P. Tanga, and A. Vulpiani, *Dynamics of passively advected impurities in simple two-dimensional flow models*, Phys. Fluids A, 4 (1992), pp. 1805–1820.

[17] M. Ding and W. Yang, *Stability of synchronous chaos and on-off intermittency in coupled map lattices*, Phys. Rev. E, 56 (1997), pp. 4009–4016.

[18] P. G. Drazin, *Nonlinear Systems*, University Press, Cambridge, 1992.

[19] D. G. Dritschel, *A general theory for two-dimensional vortex interactions*, J. Fluid Mech., 293 (1995), pp. 269–303.

[20] G. S. Duane, *Synchronized chaos in extended systems and meteorological teleconnections*, Phys. Rev. E, 56 (1997), pp. 6475–6493.

[21] J.-P. Eckmann and D. Ruelle, Physica D, 56 (1992), p. 185.

[22] W. Ferrel, *The motions of fluids and solids relative to the earth's surface*, Math. Monthly, 1 (1859), pp. 140–147,210–216,300–307,366–372,397–406.

[23] A. M. Fraser and H. L. Swinney, Phys. Rev. A, 33 (1986), p. 1134.

[24] H. Ghil and S. Childress, *Topics in Geophysical Fluid Dynamics*, Springer, New York, 1987.

[25] P. Grassberger and I. Procaccia, Physica D, 9 (1983), p. 189.

[26] G. Hadley, *Concerning the cause of the general trade winds*, Phil. Trans., 39 (1735), pp. 58–63.

[27] K. Kaneko, *Chaotic but regular posi-nega switch among coded attractors by cluster-size variation*, Phys. Rev. Lett., 63 (1989), pp. 219–223.

[28] ——, ed., *Theory and applications of coupled map lattices*, Nonlinear science: Theory and applications, John Wiley & Sons, West Sussex, England, 1993.

[29] H. Kantz and T. Shreiber, *Nonlineat Time Series Analysis*, Cambridge University Press, Cambridge, 1997.

[30] R. Kinney, J. C. McWilliams, and T. Tajima, *Coherent structures and turbulent cascades in two-dimensional incompressible magnetohydrodynamic turbulence*, Phys. Plasmas, 2 (1995), pp. 3623–3639.

[31] R. H. Kraichnan and D. Montgomery, *Two-dimensional turbulence*, Rep. Prog. Phys., 43 (1980), pp. 547–619.

[32] E. N. Lorenz, *Deterministic nonperiodic flow*, J. Atmos. Sci., 20 (1963), pp. 130–141.

[33] ——, *The local structure of a chaotic attractor in four dimensions*, Physica D, 13 (1984), p. 90.

[34] ——, *Can chaos and intransitivity lead to interannual variability?*, Tellus, 42A (1990), pp. 378–389.

[35] ——, *Dimension of weather and climate attractors*, Nature, 353 (1991), pp. 241–244.

[36] ——, *Predictability: A problem partly solved*, in Proc. Seminar on Predictability, vol. 1, ECMWF, Reading, Berkshire, UK, 1996.

[37] M. R. Maxey, *The motion of small spherical particles in a cellular flow field*, Phys. Fluids, 30 (1987), pp. 1915–1928.

[38] M. R. Maxey and J. J. Riley, *Equation of motion for a small rigid sphere in a nonunform flow*, Phys. Fluids, 26 (1983), pp. 883–889.

[39] B. McNamara and K. Wiesenfeld, Phys. Rev. A, 39 (1989), p. 4854.

[40] J. C. McWilliams, *The emergence of isolated coherent vortices in turbulent flow*, J. Fluid Mech., 146 (1984), pp. 21–43.

[41] J. C. McWilliams, *Statistical properties of decaying geostrophic turbulence*, J. Fluid Mech., 198 (1989), pp. 199–230.

[42] J. C. McWilliams, *The vortices of two-dimensional turbulence*, J. Fluid Mech., 219 (1990), pp. 361–385.

[43] J. C. McWilliams and J. B. Weiss, *Anisotropic geophysical vortices*, Chaos, 4 (1994), pp. 305–311.

[44] J. C. McWilliams, J. B. Weiss, and I. Yavneh, *Anisotropy and coherent vortex structures in planetary turbulence*, Science, 264 (1994), pp. 410–413.

[45] D. W. Moore and E. A. Spiegel, *A thermally excited nonlinear oscillator*, Astrophys. J., 143 (1966), pp. 871–887.

[46] C. Nicolis, Tellus, 34 (1982), p. 1.

[47] A. R. Osborne, A. D. Kirwan, A. Provenzale, and L. Bergamasco, Physica D, 23 (1986), p. 75.

[48] A. R. Osborne and A. Provenzale, Physica D, 35 (1989), p. 357.

[49] E. Ott, *Chaos in dynamical systems*, Cambridge University Press, Cambridge, Great Britain, 1993.

[50] E. Ott, T. Sauer, and J. A. Yorke, *Coping with Chaos*, Wiley, New York, 1994.

[51] J. M. Ottino, *The kinematics of mixing: stretching, chaos and transport*, Cambridge University press, Cambridge, 1989.

[52] N. H. Packard, J. P. Crutchfield, J. D. Farmer, and R. S. Shaw, *Geometry from a time series*, Phys. Rev. Lett., 45 (1981), pp. 712–715.

[53] L. M. Pecora and T. L. Carroll, *Synchronization in chaotic systems*, Phys. Rev. Lett., 64 (1990), pp. 821–824.

[54] L. M. Pecora, T. L. Carroll, G. A. Johnson, D. J. Mar, and J. F. Heagy, *Fundamentals of synchronization in chaotic systems, concepts, and applications*, Chaos, 7 (1997), pp. 520–543.

[55] J. Pedlosky, *Geophysical Fluid Dynamics*, Springer, New York, 1987.

[56] R. T. Pierrehumbert and H. Yang, *Global chaotic mixing on isentropic surfaces*, J. Atmos. Sci., 50 (1992), pp. 2462–2480.

[57] N. Platt, E. A. Spiegel, and C. Tresser, *The intermittent solar cycle*, Geophys. Astrophys. Fluid Dyn., 73 (1993), pp. 147–161.

[58] N. Platt, E. A. Spiegel, and C. Tresser, *On-off intermittency: A mechanism for bursting*, Phys. Rev. Lett., 70 (1993), pp. 279–282.

[59] Y. Pomeau and P. Manneville, *Intermittent transition to turbulence in dissipative dynamical systems*, Comm. Math. Phys., 74 (1980), p. 189.

[60] A. Provenzale, *Transport by coherent barotropic vortices*, Ann. Rev. Fluid Mech., 31 (1999), pp. 55–93.

[61] ——, *Transport by coherent barotropic vortices*, Ann. Rev. Fluid Mech., 31 (1999), pp. 55–93.

[62] A. Provenzale, L. A. Smith, R. Vio, and G. Murante, *Distinguishing between low-dimensional dynamics and randomness in measured time series*, Physica D, 58 (1992), pp. 31–49.

[63] A. Provenzale, B. Villone, A. Babiano, and R. Vio, *Intermittency, phase randomization and generalized fractal dimensions*, Intern. J. Bifurc. Chaos, 3 (1993), pp. 729–736.

[64] A. Provenzale, R. Vio, and S. Cristiani, Astrophys. J., 428 (1994), p. 591.

[65] S. Rahmstorf, *On the fresh-water forcing and trasnport of the atlantic thermohaline circulation*, Climate Dynamics, 12 (1996), pp. 799–811.

[66] P. B. Rhines, *Waves and turbulence on a beta-plane*, J. Fluid Mech., 69 (1975), pp. 417–443.

[67] ——, *Geostrophic turbulence*, Ann. Rev. Fluid Mech., 11 (1979), pp. 401–441.

[68] M. G. Rosenblum, A. S. Pikovsky, and J. Kurths, *Phase synchronization of chaotic oscillators*, Phys. Rev. Lett., 76 (1996), pp. 1804–1807.

[69] R. M. Samelson, *Fluid exchange across a meandering jet*, J. Phys. Oceanog., 22 (1992), p. 431.

[70] L. A. Smith, Phys. Lett. A, 133 (1988), p. 283.

[71] T. H. Solomon and J. P. Gollub, *Chaotic particle transport in time-dependent rayleigh-bénard convection*, Phys. Rev. A, 38 (1988), pp. 6280–6286.

[72] C. Sparrow, *The Lorenz equations: bifurcations, chaos and strange attractors*, Springer, Berlin, 1982.

[73] H. Stommel, *Trajectories of small bodies sinking slowly through convection cells*, J. Mar. Res., 8 (1949), pp. 24–29.

[74] ——, *Thermohaline convection with two stable regimes of flow*, Tellus, 13 (1961), pp. 224–230.

[75] F. Takens, Lecture Notes in Matematics, 898 (1981).

[76] P. Tanga, A. Babiano, A. Provenzale, and B. Dubrulle, *Forming planetesimals in vortices*, ICARUS, 121 (1996), pp. 158–170.

[77] J. Theiler, S. Eubank, A. Longtin, B. Galdrikian, and J. B. Farmer, Physica D, 58 (1992), p. 77.

[78] J. Thomson, *On the grand currents of atmospheric circulation*, Phil. Trans. Roy. Soc. A, 183 (1857), pp. 653–684.

[79] J. von Hardenberg and A. Provenzale, *Dynamics of forced and coupled systems*, in Proceedings of the International School of Physics "Enrico Fermi", G. C. Castagnoli and A. Provenzale, eds., no. 133, IOS Press, Amsterdam, 1997, pp. 161–176.

[80] J. G. von Hardenberg, F. Paparella, N. Platt, A. Provenzale, E. A. Spiegel, and C. Tresser, *Missing motor of on-off intermittency*, Phys. Rev. E, 55 (1997), pp. 58–64.

[81] J. B. Weiss and E. Knobloch, *Mass transport and mixing by modulated travelling waves*, Phys. Rev. A, 40 (1989), p. 2579.

[82] J. B. Weiss and J. C. McWilliams, *Nonergodicity of point vortices*, Phys. Fluids A, 3 (1991), pp. 835–844.

[83] ——, *Temporal scaling behaviour of decaying two-dimensional turbulence*, Phys. Fluids A, 5 (1993), pp. 608–621.

[84] J. B. Weiss, A. Provenzale, and J. C. McWilliams, *Lagrangian dynamics in high dimensional point vortex systems*, Phys. Fluids, (1998).

[85] J. A. Whitehead, *Thermohaline ocean processes and models*, Ann. Rev. Fluid Mech., 27 (1995), pp. 89–113.